République Algérienne Démocratique et Populaire

Ministère de l'Enseignement Supérieur et de la Recherche Scientifique

Université Mohamed El Bachir El Ibrahimi de Bordj Bou Arreridj

Département d'Électronique

Thèse de Doctorat

Présentée en vue de l'obtention du diplôme de **DOCTORAT**

En : Télécommunications

Spécialité : Systèmes de Télécommunications

Par : BENGHERABI Ayoub

Thème

Performances des techniques d'accès multiple par saut dans le temps dans des milieux défavorables

Soutenue publiquement, le **19 janvier 2026**, devant le jury composé de:

M.	MESSAOUDENE Idris	MCA	à l'Univ-BBA	Président
M.	FLISSI Mustapha	Professeur	à l'Univ-BBA	Encadreur
M.	ROUABAH Khaled	Professeur	à l'Univ-Msila	Co-encadreur
M.	CHALABI Izzeddine	Professeur	à l'Univ-Msila	Examinateur
M.	MEZAACHE Salah Eddine	MCA	à l'Univ-BBA	Examinateur

People's Democratic Republic of Algeria
Ministry of Higher Education and Scientific Research
University Mohamed El Bachir El Ibrahimi of Bordj Bou Arreridj
Electronic department

Doctoral Thesis

Presented for the obtaining of the degree of **DOCTOR**

In: Telecommunications

Specialty: Telecommunication Systems

By: BENGHERABI Ayoub

Theme

Performance of Time-Hopping Multiple Access Techniques in Challenging Environments

Publicly defended, on **19 January 2026**, before the jury composed of:

Mr.	MESSAOUDENE Idris	MCA	at Univ-BBA	President
Mr.	FLISSI Mustapha	Professor	at Univ-BBA	Supervisor
Mr.	ROUABAH Khaled	Professor	at Univ-Msila	Co-supervisor
Mr.	CHALABI Izzeddine	Professor	at Univ-Msila	Examiner
Mr.	MEZAACHE Salah Eddine	MCA	at Univ-BBA	Examiner

I dedicate this thesis first and foremost to the pillars of my life: to my beloved mother, Dahmani Khadidja (Zahira), for your endless love, prayers, and sacrifices that paved my way.
To my dear father, Amar, for your unwavering support and for always pushing me to be my best. You taught me the true value of perseverance, and your constant belief in me was a powerful source of strength.
To my brothers, Tarek and Younes, and my sister, Hanane, for your constant encouragement and for being my lifelong friends.
My heartfelt gratitude extends to my entire family and all my friends who stood by me and encouraged me throughout this journey. This achievement is as much yours as it is mine.

Furthermore, I dedicate this work to the steadfast people of Gaza. To your resilience in the face of injustice, to the spirit of your resistance that inspires the world, and to the memory of every soul taken too soon. May this small effort be a testament to the enduring fight for freedom.
And let us always remember the promise made by Allah to the patient:
وبشر الصابرين ⋆ الذين إذا أصابتهم مصيبة قالوا إنا لله وإنا إليه راجعون ⋆ أولئک عليهم صلوات من ربهم ورحمة وأولئک هم المهتدون

Acknowledgment

ربنا لك الحمد أنت قيم السماوات والأرض ومن فيهن، ولك الحمد أنت رب السماوات والأرض ومن فيهن، ولك الحمد أنت نور السماوات والأرض ومن فيهن، أنت الحق وقولك الحق ووعدك الحق ولقاؤك الحق. الحمد لله، الذي بفضله وتوفيقه يسّر لي إتمام هذا العمل، فله الحمد أولاً وآخراً

وعملاً بقول رسول الله صلى الله عليه وسلم: من لا يشكر الناس لا يشكر الله

I am sincerely grateful to my thesis supervisor, Professor FLISSI Mustapha, whose guidance and unwavering support have been instrumental throughout this research journey. His insightful advice and rigorous scientific approach not only enhanced the quality of this work but were also essential to my development as a researcher. I feel privileged to have worked under his supervision.

I also extend my gratitude to my co-supervisor, Professor ROUABAH Khaled, whose scientific rigor, profound knowledge, and encouragement were the cornerstones of this thesis. His patience and mentorship have been a continuous source of personal and academic inspiration. I am sincerely grateful for the invaluable guidance and insights that I have gained from his expertise.

Furthermore, I would like to thank the members of the jury who took on the responsibility of evaluating this thesis. I sincerely thank Professor CHALABI Izzeddine and Dr. MEZAACHE Salah Eddine for their meticulous review and the insightful discussions that have greatly enriched this work. It is a great honor that Dr. MESSAOUDENE Idris graciously accepted to preside over this jury, and I extend my deepest respect and heartfelt gratitude to him.

I am deeply grateful to Dr. BENGHERABI Messaoud, Dr. TITOUNI Salem, Pr ATIA Salim, Dr. HIMEUR Yassine, and Dr. DAWOUD Diana for their invaluable mentorship and guidance. I also thank the Scientific Committee and my colleagues at the ETA Laboratory for their support. My sincere appreciation goes to the administrative staff of the Faculty of Science and Technology and the Electronics Department, with special thanks to the secretary, Loubna, and her colleagues for their constant assistance.

Abstract

Pseudolite systems are increasingly used to augment Global Navigation Satellite Systems (GNSS) in challenging environments, thereby improving the reliability of positioning, navigation, and timing services. Time-Hopping Multiple Access (THMA) effectively mitigates the near–far problem in pseudolite signal transmission, yet, similarly to GNSS, the system remains highly susceptible to performance degradation caused by multipath (MP) interference and noise. This thesis examines the robustness of THMA under MP-rich conditions, with a focus on how MP primarily affects this signal through distortions in the initial phase, which can be separated into integral and fractional components. In the integral part, the correlation function between the received signal and the local replica produces line-of-sight and MP peaks, which can merge to allow partial mitigation of MP effects. In contrast, mitigation in the fractional part is considerably more challenging and requires advanced baseband-level strategies, similar to those employed for standard GNSS signals. Existing approaches, such as the narrow correlator, double-delta, extended double-delta, and locally generated code–based techniques, are limited in their adaptability to dynamic environments where MP and noise characteristics vary. To address this limitation, this thesis proposes a novel Multipath-Aware Adaptive Delay Locked Loop (MAA-DLL) architecture that integrates real-time MP delay estimation with an adaptive reconfiguration of the DLL. This reconfiguration dynamically selects the optimal Early-Late correlator pairs and applies optimized weightings via a lookup table. MAA-DLL was evaluated across various modern GNSS modulations, including BOC (2,1), BOC (4,1), higher-order BOC (10,5), and BOC (14.2), as well as the composite MBOC(6,1,1/11), under two scenarios. In MP-only conditions, it achieved the lowest running average error across a diverse range of MP delays, confirming reliable performance over the full range. In the joint MP-and-noise scenario, root mean square error was evaluated across all tested signals under both fixed (-30 dB) and variable (-35 to -20 dB) signal-to-noise ratio levels. The MAA-DLL consistently outperformed conventional methods, demonstrating its effectiveness in improving the accuracy and robustness of GNSS and pseudolite systems under challenging conditions.

Keywords: Pseudolite , GNSS, multipath interference, noise, THMA, MAA-DLL.

Résumé

Les systèmes pseudolite sont de plus en plus utilisés pour compléter les systèmes mondiaux de navigation par satellite (SMNS) dans des environnements difficiles, améliorant ainsi la fiabilité des services de positionnement, navigation et synchronisation. L'accès multiple par sauts dans le temps (AMST) atténue efficacement le problème de proche-lointain dans la transmission des signaux pseudolite, mais, comme pour les SMNS, le système reste très sensible à la dégradation des performances causée par les interférences de trajets multiples (TM) et le bruit. Cette thèse examine la robustesse de l'AMST dans des conditions riches en TM, en se concentrant sur la manière dont le TM affecte principalement le signal par des distorsions de la phase initiale, pouvant être séparées en composantes intégrale et fractionnaire. Dans la partie intégrale, La fonction de corrélation entre le signal reçu et la réplique locale génère un pic associé à la composante en ligne de visée et un autre lié aux TM. Ces pics peuvent se superposer, entraînant une atténuation partielle des effets des TM. En revanche, l'atténuation dans la partie fractionnaire est beaucoup plus complexe et nécessite des stratégies avancées au niveau de la bande de base, similaires à celles utilisées pour les signaux SMNS standards. Les approches existantes, telles que le corrélateur étroit, le double-delta, le double-delta étendu et la technique basée sur un code localement généré, présentent des limites d'adaptabilité dans des environnements dynamiques où les caractéristiques du TM et du bruit varient. Pour surmonter cette limitation, cette thèse propose une nouvelle architecture de Boucle de Poursuite Adaptative Sensible aux TM (BPAS-TM), qui intègre l'estimation en temps réel du retard TM avec une reconfiguration adaptative de la boucle de poursuite de code. Cette reconfiguration sélectionne dynamiquement les paires de corrélateurs avance-retard optimales et applique des pondérations optimisées via une table de correspondance. L'architecture BPAS-TM a été évaluée sur diverses modulations SMNS modernes, y compris BOC(2,1), BOC(4,1), les BOC d'ordre supérieur BOC(10,5) et BOC(14,2), ainsi que le signal composite MBOC(6,1,1/11), selon deux scénarios. Dans des conditions avec uniquement du TM, elle a atteint la plus faible erreur moyenne glissante sur une large plage de retards TM, confirmant une performance fiable sur toute la plage. Dans le scénario combinant TM et bruit, l'erreur quadratique moyenne a été évaluée pour tous les signaux testés, sous des niveaux de rapport signal sur bruit fixes (-30 dB) et variables (de -20 à -35 dB). La BPAS-TM a systématiquement surpassé les méthodes conventionnelles, démontrant son efficacité pour améliorer la précision et la robustesse des systèmes SMNS et des systèmes pseudolite dans des conditions difficiles.

Mots-clés : Pseudolite, SMNS, interférence à trajets multiples, Bruit, AMST, BPAS-TM.

ملخص

تُستخدم أنظمة الإرسال الأرضي الشبيه بالأقمار الصناعية بشكل متزايد لتعزيز أنظمة الأقمار الصناعية العالمية للملاحة في البيئات الصعبة، مما يحسن موثوقية خدمات تحديد المواقع والملاحة والتوقيت. فعلى الرغم من أن الوصول المتعدد بالقفز الزمني يخفف بشكل فعّال من مشكلة القريب–البعيد في إرسال إشاراتها، إلا أن النظام يظل شديد التأثر بتدهور الأداء الناتج عن تداخل المسارات المتعددة والضوضاء. تركز هذه الأطروحة على دراسة متانة الوصول المتعدد بالقفز الزمني في البيئات الغنية بالـمسارات المتعددة، مع التركيز على كيفية تأثير الـمسارات المتعددة على إشارات الوصول المتعدد بالقفز الزمني من خلال تشويه الطور الأولي، الذي يمكن فصله إلى مكونات صحيحة وجزئية. في الجزء الصحيح، تُنتج دالة الارتباط بين الإشارة المستقبلة والنسخة المحلية قمما من كل من الإشارة المباشرة وإشارات المسارات المتعددة، والتي يمكن دمجها للسماح بتخفيف جزئي لتأثير المسارات المتعددة. أما في الجزء الكسري، فإن التخفيف أكثر تعقيدا ويتطلب استراتيجيات متقدمة على مستوى النطاق الأساسي، مماثلة لتلك المستخدمة مع إشارات الأقمار الصناعية العادية. الطرق التقليدية محدودة في قدرتها على التكيف مع البيئات الديناميكية حيث تتغير خصائص المسارات المتعددة والضوضاء. لمعالجة هذا القيد، تقترح هذه الأطروحة بنية جديدة تُسمى حلقة التتبع المكيفية زمنياً المدركة لتعدد المسارات، والتي تدمج تقديرا لحظيا لتأخيرات المسارات المتعددة مع إعادة تشكيل تكيفية عبر اختيار ديناميكي للمترابطات وتطبيق ترجيح محسّن باستخدام جدول بحث. تم تقييم حلقة التتبع المكيفية زمنياً المدركة لتعدد المسارات على مجموعة واسعة من التضمينات الحديثة لـأنظمة الأقمار الصناعية العالمية للملاحة، بما في ذلك BOC(2,1)، BOC(4,1)، التضمينات الأعلى رتبة BOC(10,5) و BOC(14,2)، بالإضافة إلى الإشارة المركبة MBOC(6,1,1/11)، ضمن سيناريوهين. في حالة المسارات المتعددة فقط، حققت أقل قيمة لمتوسط الخطأ المتحرك عبر جميع التأخيرات، مما يؤكد أداءً موثوقا على كامل النطاق. أما في السيناريو الذي يجمع بين المسارات المتعددة والضوضاء، فقد أظهرت نتائج متانة فائقة تحت كل من نسبة الاشارة الى الضوضاء الثابتة عند 30 dB - والمتغيرة من 35 dB - إلى 20 dB -. عبر جميع الإشارات المختبرة، تفوّق حلقة التتبع المكيفية زمنياً المدركة لتعدد المسارات باستمرار على الطرق التقليدية، مما يبرهن فعاليته في تعزيز الدقة والمرونة لأنظمة أنظمة الأقمار الصناعية العالمية للملاحة و انظمة الإرسال الأرضي الشبيه بالأقمار الصناعية في البيئات الصعبة.

الكلمات المفتاحية: أنظمة الإرسال الأرضي، أنظمة الأقمار الصناعية العالمية للملاحة، المسارات المتعددة، ضوضاء، الوصول المتعدد بالقفز الزمنية، حلقة التتبع المكيفية زمنياً المدركة لتعدد المسارات.

Research Publications

- Ayoub Bengherabi, Mustapha Flissi "Time-Hopping Pulse Detection in Multipath Environments: Analysis and Mitigation". Proc. The 1st International Conf.: Electronics Engineering, Technology of Telecommunications Advanced Applications, Bordj Bou Arreridj, Algeria, 2023.

- Ayoub Bengherabi, Mustapha Flissi and Khaled Rouabah, "Performance Evaluation of Unambiguous Tracking Techniques for BOC-Modulated GNSS Signals Under Challenging Conditions". Proc. First International Conf.: Green Engineering, Bordj Bou Arreridj, Algeria, 2025.

- Ayoub Bengherabi, Mustapha Flissi, Khaled Rouabah, Salim Attia, Diana W. Dawoud, Yassine Himeur, Shadi Atalla, and Wathiq Mansoor. "Efficient Multipath Mitigation in Gnss Using Dynamic Selection and Weighting of Early-Late Correlators". IEEE Access, 13: 110736–110751, 2025, doi : 10.1109/ACCESS.2025.3581856.

Contents

List of Figures

List of Tables

Nomenclature

Acronyms / Abbreviations

A-PL	Airborne Pseudolite
ACF	Autocorrelation Function
ADC	Analogue-to-Digital Converter
AWGN	Additive White Gaussian Noise
BCS	Binary Coded Symbols
BOC	Binary Offset Carrier
BPSK	Binary Phase-Shift Keying
CA	Coarse/Acquisition
CBOC	Composite BOC
CDMA	Code Division Multiple Access
CF	Correlation Function
CS	Commercial Service
DD	Double Delta
DF	Discriminator Function
DLL-DF	DLL discriminator function
DLL	Delay-Locked Loop
DoD	Department of Defense
DOP	Dilution of Precision

DP	Dot Product
DSSS	Direct Sequence Spread Spectrum
EDD	Extended Double-Delta
FDMA	Frequency Division Multiple Access
G-PL	Ground-Based Pseudolite
GEO	Geostationary Earth Orbit
GLONASS	Global Orbiting Navigation Satellite System
GLONASSST	GLONASS System Time
GNSS	Global Navigation Satellite Systems
GPS	Global Positioning System
GPST	GPS System Time
GST	Galileo System Time
HALE	High Altitude Long Endurance
HAPS	High Altitude Platform Systems
HRC	High-Resolution Correlator
IAT	International Atomic Time
IFFT	Inverse FFT
IF	Intermediate Frequency
LOS	Line-of-Sight
LPF	Low-Pass Filter
MAA-DLL	Multipath-Aware Adaptive Delay Locked Loop
MBOC	Multiplexed BOC
MC/MF	Multi-constellation/Multi-frequency
MEO	Medium Earth Orbit

MLE	Maximum Likelihood Estimation
MP	Multipath
NC	Narrow Correlator
NCO	Numerically Controlled Oscillator
NSD	Non-coherent Squaring Detection
OS	Open Service
PAC	Pulse Aperture Correlator
PLL	Phase-Locked Loops
PNT	Positioning, Navigation, and Timing
PPS	Precise Positioning Service
PRN	Pseudo-Random Noise
PSD	Power Spectral Density
PVT	Position, Velocity and Time
RAE	Running Average Error
RMSE	Root Mean Squared Error
RNSS	Radionavigation Satellite Service
RTCM	Radio Technical Commission for Maritime Services
SAR	Search and Rescue
SC	Strobe Correlator
SIT	Slot Index Table
SLG	Specified Locally Generated
SNR	Signal-to-Noise Ratio
SOL	Safety of Life
SPFs	Stratospheric Platforms

SPS	Standard Positioning Service
TDMA	Time Division Multiple Access
THMA	Time-Hopping Multiple Access
THSIs	TH Slot Indices
TMBOC	Time-Multiplexed BOC
TTC	Telemetry and Control
UERE	Equivalent Range Error
PL	Pseudolite

General Introduction

Context and Motivation

GNSS, encompassing the Global Positioning System (GPS), the Global Orbiting Navigation Satellite System (GLONASS), Galileo, and BeiDou, form the backbone of Positioning, Navigation, and Timing (PNT) services. These services support a wide range of critical applications, from autonomous transportation to disaster management and emergency response [1–5]. To expand the PNT capability to domains with minimal or no GNSS signal availability, pseudolite (PL) systems are being developed. PLs are ground-based or airborne transmitters intended to increase signal GNSS-like signal availability indoors, in urban canyons, and in aided aircraft landing operations [6–9].

GNSS signals are strongly affected by atmospheric delays, particularly ionospheric and tropospheric effects, whereas PL systems are largely unaffected by such propagation errors but are more vulnerable to the near–far problem [8, 10–12]. In this case, signals from nearby transmitters can exceed satellite signals by more than 20 dB, creating an imbalance that may saturate the receiver's dynamic range and disrupt coexistence between systems. A mitigation strategy is provided by THMA, which assigns pseudo-random transmission slots to reduce interference and facilitate frequency sharing [6, 8, 9, 13]. Beyond these system-specific impairments, both GNSS and PL are affected by common error sources, including clock offsets, Doppler frequency shifts, and MP [14–16]. Among these, MP is the most persistent and detrimental, as reflected and diffracted signals distort correlation functions (CFs), introduce pseudorange biases, and significantly degrade positioning accuracy [17, 18].

In the THMA PL signal, residual MP effects appear within the initial phase, which can be separated into integral and fractional components. The integral component is associated with the number of timeslots, while the fractional component corresponds to the PRN code phase of the Direct Sequence Spread Spectrum (DSSS) portion of the signal and represents sub-timeslot delays. In the integral part, the CF between the received signal and the local replica generates two peaks, corresponding to the Line-of-Sight (LOS) and

MP components; merging these peaks allows partial mitigation of MP effects. However, residual distortions in the fractional domain remain complex and require advanced MP mitigation techniques similar to those applied to standard GNSS signals [6, 19].

To further enhance resistance to MP, modern GNSS signals employ advanced modulation schemes that extend beyond conventional Binary Phase-Shift Keying (BPSK). Such modulations are BOC, MBOC and CBOC, TMBOC, and BCS [15, 20–25]. These modulations enhance spectral coexistence and inter-channel spacing, resulting in improved accuracy of position determination. The additional complexities, however, also contribute to new signal ambiguities and a higher demand on processing resources at the receiver. These developments have amplified the need for effective baseband MP mitigation strategies to achieve reliable performance [19].

Existing baseband MP mitigation methods, including the Narrow Correlator (NC), Double-Delta (DD), Extended Double-Delta (EDD), and Specified Locally Generated (SLG), provide only partial solutions, as their fixed weighting schemes and correlator structures cannot adapt to the time-varying nature of MP across different delays and modulation types. As a result, MP distortions in the Discriminator Function (DF) of Delay-Locked Loops (DLL) persist, introducing code-tracking biases manifested through zero-crossing shifts and linear range reduction, which ultimately degrade tracking accuracy. To address these limitations, this thesis proposes the Multipath-Aware Adaptive Delay Locked Loop (MAA-DLL). This adaptive architecture integrates real-time MP delay estimation with dynamic correlator adaptation, with its principles and superior performance detailed in Chapter 4. This design provides a significant advancement in mitigating MP interference, thereby improving tracking accuracy and reliability in GNSS and PL signals under diverse and dynamic conditions.

Thesis Objectives

This thesis aims to achieve several objectives, outlined as follows:

- Analyze the specific effects of MP interference on GNSS and THMA-based PL signals, with particular emphasis on its impact on DLL-DFs and the limitations of conventional baseband MP mitigation techniques.

- Design and implement an innovative MAA-DLL architecture incorporating real-time MP delay estimation, dynamic selection of optimal E-L correlators, and adaptive weighting to overcome the limitations of existing approaches.

- Carefully evaluate the performance of the proposed MAA-DLL across all simula-

tion scenarios, comparing its tracking accuracy and interference suppression with conventional methods under varying signals and environmental conditions.

- Demonstrate the robustness of the MAA-DLL across BOC-modulated GNSS signals under combined MP and noise interference.

Thesis Contribution

The main contributions of this thesis are as follows:

- **Comprehensive Review of PL and GNSS Systems :** This thesis provides an exhaustive and comprehensive baseline for PL and GNSS positioning systems. It thoroughly reviews the architectures, the nature of the signals, and the multiplicity of sources of extrinsic and intrinsic errors that interfere with their performance.
- **Detailed Assessment of GNSS Modulations and THMA :** A thorough evaluation of advanced GNSS modulation schemes (BPSK, BOC, MBOC, BSC, CBCS), with a detailed study of the THMA framework in PL systems, including TH-pulsed signal composition, code-based THSI generation, and statistical distributions of the slot index table (SIT).
- **Analysis of MP Effects and Mitigation in THMA-Based PL Signals :** This work examines the impact of MP on THMA-Based PL signals and reviews baseband-level mitigation techniques for GNSS and PL signals, highlighting their principles, strengths, and limitations.
- **Thorough Examination of MP Impact on DLL-DFs :** This study offers an accurate investigation of the MP effects on DLL-DFs with fixed configurations, quantifying their impact as code-tracking biases through zero-crossing shifts and reduced linear range, thus motivating the proposed adaptive mitigation strategy.
- **Proposal and Validation of a Dynamic MAA-DLL Architecture :** This thesis introduces a novel MAA-DLL design that enhances robustness against MP interference by dynamically selecting optimal E-L correlators and applying adaptive weighting. Its performance is rigorously validated through extensive simulations across two distinct scenarios:
  - **MP Mitigation Performance :** The method's ability to mitigate MP was tested against a wide range of signals, including BOC(2,1), BOC(4,1), the higher-order BOC(10,5) and BOC(14,2), and the complex MBOC(6, 1, 1/11).

The MAA-DLL consistently achieved lower Running Average Error (RAE) values across the full range of MP delays compared to conventional methods.

– **Robustness Against Combined Interference :**In the second scenario, the resilience of the MAA-DLL architecture was validated under combined MP and noise conditions, achieving lower Root Mean Squared Error (RMSE) at a fixed SNR of -30 dB and over a variable SNR range from -35 dB to -20 dB.

Document Organization

The thesis consists of a general introduction and four chapters, summarized as follows:

Chapter 1 establishes the foundations of GNSS, presenting the principles of satellite navigation such as atomic clocks and pseudorange measurements, and offering an overview of the main GNSS constellations (GPS, GLONASS, Galileo, BeiDou) with their architectures, signals, services, and interoperability. The chapter also introduces PL systems, their classifications, applications, and the inherent near/far problem, concluding with an examination of various positioning error sources.

We then turn to **Chapter 2**, which addresses key aspects of signal design. It begins with the fundamentals of GNSS signals, including DSSS, PSD, and ACF, before examining advanced modulation schemes such as BPSK, BOC, MBOC (with CBOC and TMBOC variants), and BSC with CBCS implementation, highlighting their main characteristics and offering a comparative analysis. The chapter then introduces THMA as a solution to the near-far problem in PL systems, detailing the THMA-pulsed signal structure, SIT generation approaches, and their statistical properties.

In **Chapter 3**, we provide a detailed analysis of GNSS/PL signal processing, covering acquisition methods (serial and parallel search) along with THMA pulse position detection. It also examines tracking techniques based on PLL with various phase discriminators and DLL in both coherent and non-coherent forms, addresses the effects of MP, and concludes with an overview of baseband MP mitigation strategies including NC, DD, EDD, and SLG.

Chapter 4 presents the impact of MP on conventional DLL-DF with fixed configurations, highlighting their limitations, and consequently proposes the novel MAA-DLL architecture, which integrates real-time MP delay estimation with dynamic selection and adaptive weighting of E-L correlators. It concludes with a thorough presentation and discussion of experimental results, demonstrating the MAA-DLL's superior performance in mitigating MP interference and enhancing tracking accuracy under various conditions.

This thesis will be concluded with a general conclusion and future perspectives.

Chapter 1

GNSS and Pseudolite Positioning Systems

1.1 Introduction

PNT data is the invisible backbone of countless modern technologies. While GNSS provide remarkable worldwide PNT services, their faint signals often falter in challenging environments, such as dense urban canyons, indoor spaces, or deep valleys. In these GNSS-denied scenarios, PLs emerge as a crucial supplementary technology designed to enhance positioning accuracy, availability, and integrity where satellites alone fall short.

This chapter builds a comprehensive foundation for understanding both GNSS and PL positioning. It begins by explaining the fundamental principles of satellite navigation, from its three-segment architecture to position determination using pseudorange measurements. The discussion then surveys the major global constellations, examining their features and the critical role of interoperability. From there, the focus pivots to PL systems, their use as a powerful local augmentation, and their operational challenges, notably the near-far problem. Finally, the chapter identifies common error sources, such as atmospheric delays and multipath interference, providing the essential groundwork for the advanced mitigation techniques developed in the subsequent chapters.

1.2 Satellite Navigation

Satellite navigation utilizes the GNSS to provide users anywhere on Earth with their precise Position, Velocity, and Time (PVT). A GNSS is formally defined as any satellite system offering autonomous geospatial positioning with worldwide coverage [2].

The United States' GPS, the Russian Federation's GLONASS, the European Union's

Galileo, and China's BeiDou are currently the primary global GNSS systems. These systems were initially developed for military use, but they are now widely used in civilian settings for PVT purposes. The precise atomic clocks on board satellites, which ensure accurate time measurement, are crucial to precise satellite navigation. The strict synchronization of every satellite with a universal time reference, like Coordinated Universal Time (UTC), is necessary for accurate position computation. A receiver must concurrently track signals from a minimum of four satellites to determine the user's position and time. To guarantee worldwide coverage, this essential requirement calls for massive satellite constellations, or "fleets" [2, 3](Figure1.1).

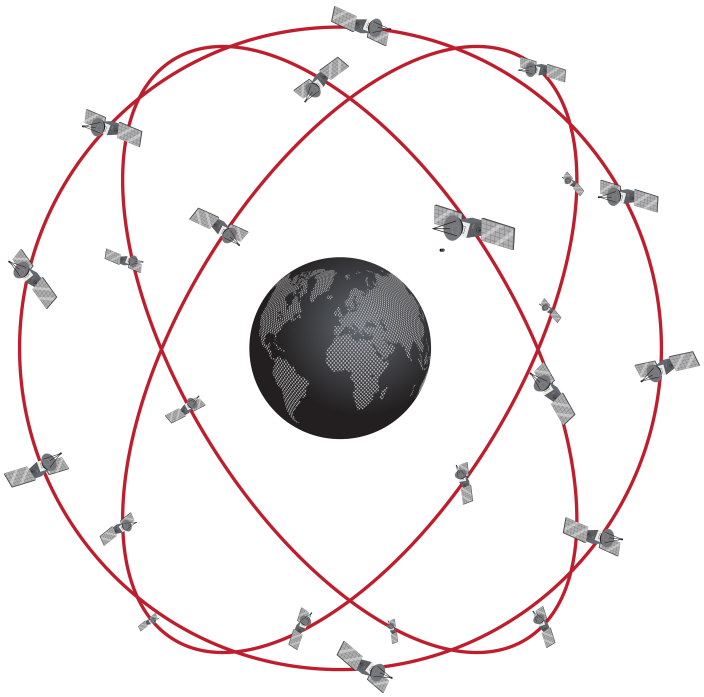

figure 1.1: GNSS constelation [26].

As conceptually shown in Figure 1.2, each GNSS is mainly organized around three interconnected segments: the spatial segment, the control segment, and the user segment. All of the main GNSS technologies share essentially identical architectural concepts among their basic segments.

The GNSS satellite constellation in Earth's orbit makes up the spatial segment. To achieve the required worldwide coverage, each GNSS system launches a distinct constellation of satellites that are carefully placed in orbit. Signals with unique identifiers, exact timing information, orbital data (ephemeris), and status indicators are continuously broadcast by individual GNSS satellites [27, 28]. A system of terrestrial stations makes up the control segment. Its primary duties include monitoring and managing the satellites to

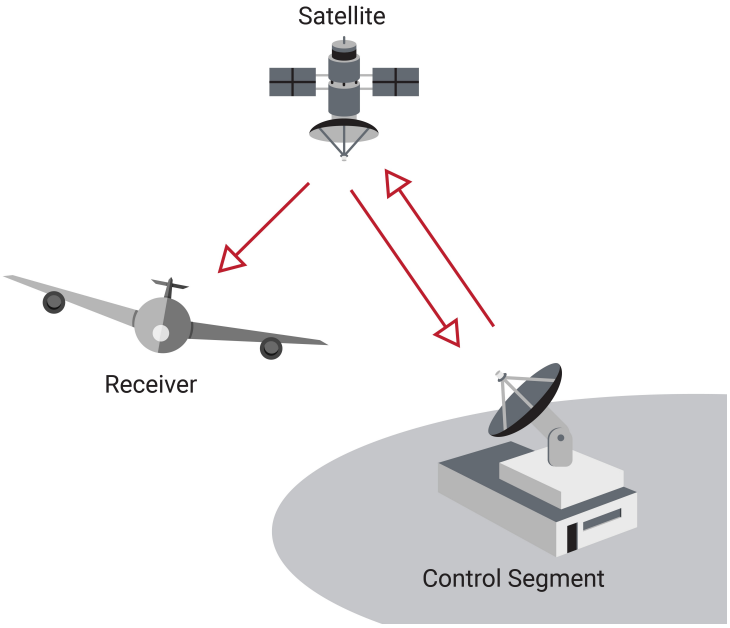

figure 1.2: GNSS segments [26].

maintain their exact orbits. To ensure signal accuracy, this segment also performs vital satellite health monitoring and regularly uploads updated navigation messages, including clock and ephemeris corrections [27, 28]. Lastly, the user segment includes a range of military and civilian receivers. These receivers are made to receive and process the signals that the satellites send to give the end user access to vital PNT functions [27, 28].

1.2.1 Positioning Principles

Satellites continually broadcast signals containing the exact time and their current orbiting position, information sourced from atomic clocks onboard. Most of these clocks rely on rubidium or caesium, and they are so accurate that they drift by no more than a single second throughout 30,000 to 1,000,000 years. To maintain this level of precision, several ground control stations regularly check, calibrate, and synchronize each clock [4].

The transmissions travel as electromagnetic waves move at roughly 300,000 km per second, the accepted speed of light in a vacuum [5, 29]. Because a receiver must also keep time accurate, it first reads the signal's arrival and compares that moment with the time stamped in the onboard log. By noting the time difference, the receiver estimates how long the message spent in transit and multiplies that interval by the speed of light, resulting in a preliminary distance between itself and the circling satellite. Using trilateration, the receiver determines its three-dimensional location by measuring the distance to a minimum of four satellites (Figure 1.3).

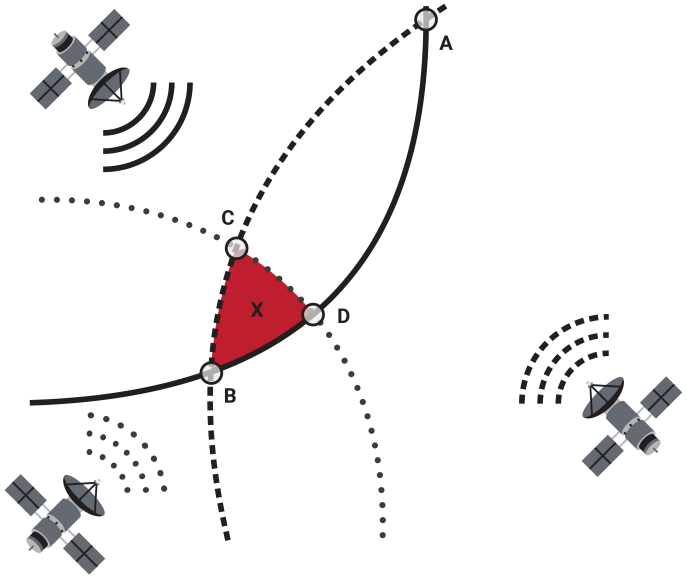

figure 1.3: GNSS trilateration [26].

1.2.2 Pseudorange Measurement

The measurement of the signal's propagation time, Δt, is the fundamental method for determining the geometric distance ρ between a satellite and a receiver. This period refers to the amount of time required for a code generated by a satellite to travel from the satellite's antenna to the receiver's antenna. The geometric range between the user and the satellite can be computed by multiplying the measured propagation time, Δt, by the speed of light in a vacuum, c (roughly 3×10^8 m/s). The precise calculation of Δt is essential to this distance calculation. A positioning error of 300 meters can result from even a small error in Δt, like $1\mu s$.

The clocks inside receivers and those aboard satellites, however, are not precisely in sync with one another or with a standard system time. Thus, the measured range, represented by ρ, is called a *pseudorange*. Because the distance is calculated by multiplying the propagation speed of the signal, c, by the observed time difference between the unsynchronized satellite and receiver clocks, it is referred to as a "pseudo."

The calculation of pseudorange requires consideration of the following temporal components, conceptually illustrated in Figure 1.4 :

- The time equivalent to the true geometric distance.
- The offset between the system time and the receiver's clock.
- The offset between the system time and the satellite's clock.

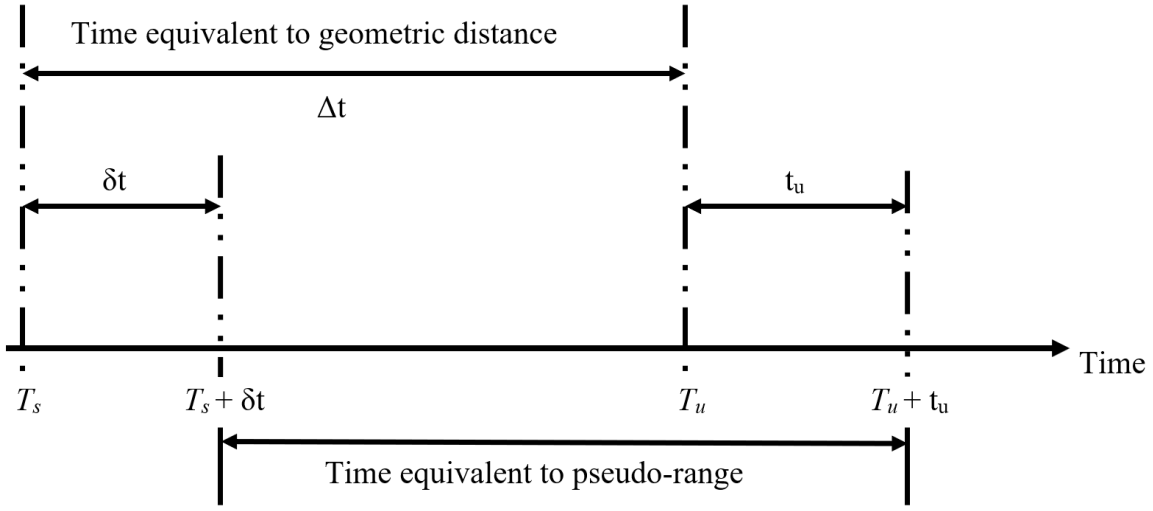

figure 1.4: Temporal relationships for distance measurement.

Where:

- T_s: System time at which the signal left the satellite.
- T_u: System time at which the signal reached the receiver.
- δt: Satellite clock offset from system time (positive for advance, negative for delay).
- t_u: Receiver clock offset from system time.
- $T_s + \delta t$: Satellite clock reading when the signal was transmitted.
- $T_u + t_u$: Receiver clock reading when the signal was received.

Based on these definitions, the true geometric distance r can be expressed as:

$$r = c(T_u - T_s) = c \cdot \Delta t \tag{1.1}$$

And the pseudorange ρ is given by:

$$\rho = c[(T_u + t_u) - (T_s + \delta t)] = r + c(t_u - \delta t) \tag{1.2}$$

Several ground control points on Earth are used to periodically adjust and synchronize the satellite clock offset, δt, with the system time. Consequently, it is possible to simplify the pseudo-range equation to:

$$\rho = r + c \cdot t_u \tag{1.3}$$

Where t_u represents the receiver clock offset relative to the perfectly synchronized satellite-broadcast time [5].

To determine the user's three-dimensional position (ξ_j, η_j, ζ_j) and the receiver clock offset t_u, pseudorange measurements are simultaneously acquired from at least four satellites. These measurements form a system of non-linear equations that can be solved to yield the receiver's state [5]:

$$\rho_1 = \sqrt{(\xi_1 - \xi_u)^2 + (\eta_1 - \eta_u)^2 + (\zeta_1 - \zeta_u)^2} + c \cdot t_u \tag{1.4}$$

$$\rho_2 = \sqrt{(\xi_2 - \xi_u)^2 + (\eta_2 - \eta_u)^2 + (\zeta_2 - \zeta_u)^2} + c \cdot t_u \tag{1.5}$$

$$\rho_3 = \sqrt{(\xi_3 - \xi_u)^2 + (\eta_3 - \eta_u)^2 + (\zeta_3 - \zeta_u)^2} + c \cdot t_u \tag{1.6}$$

$$\rho_4 = \sqrt{(\xi_4 - \xi_u)^2 + (\eta_4 - \eta_u)^2 + (\zeta_4 - \zeta_u)^2} + c \cdot t_u \tag{1.7}$$

Here, (ξ_j, η_j, ζ_j) denotes the three-dimensional position of the j-th satellite.

1.2.3 GPS

GPS, first built by the U.S. Department of Defense (DoD) in the 1970s, was the world's first fully working satellite navigation network. Originally designed to help troops navigate even in adverse weather conditions, the system has evolved significantly over the last fifteen years, finding applications in a wide range of settings, including cars, planes, delivery fleets, ambulances, and even smartphones. As a result, GPS has become a standard part of modern life, quietly steering people and machines across towns, countries, and oceans [16].

GPS is a worldwide tool that provides precise three-dimensional position and time data to anyone with the correct receiver. Because it operates passively, numerous users can access the service simultaneously without interfering with one another. Today, the GPS fleet typically includes about 31 working satellites, numbering more than its original 24, spread across six separate orbital planes. Each satellite flies about 20,200 kilometres above the planet, tilted 55 degrees to the equator, and completes one loop in roughly 11 hours and 58 minutes [15, 16].

1.2.3.1 GPS Signals and Services

GPS satellites send out signals that are stamped with the time recorded by their ultra-stable atomic clocks, all of which are synchronized with the same master GPS time. These radio waves ride on carefully chosen carrier waves that fall within the 1559-1610 MHz band set aside internationally for radionavigation satellite service (RNSS). At present, the system mainly broadcasts three distinct carrier frequencies [15, 16, 30]:

- $f_{L1} = 1575.42$ MHz
- $f_{L2} = 1227.60$ MHz
- $f_{L5} = 1176.45$ MHz

Using code-division multiple access (CDMA) technology, every satellite sends out a distinct spreading code over the same frequency bands. The codes are deliberately selected for their low cross-correlation, allowing receivers to pick out a single satellite's signal even when others are present. Traditionally, the GPS offered two primary services, each tied to the specific spreading code and frequency it used [31, 32]:

Standard Positioning Service (SPS) This service is openly and constantly accessible to the public for non-military uses. It operates on the L1 frequency using the Coarse/Acquisition (CA) code. Under normal conditions, the horizontal positioning accuracy of the Standard Positioning Service is about 10 meters.

Precise Positioning Service (PPS) This highly accurate service is reserved for authorized governmental agencies, particularly military entities. It utilizes the encrypted Precise P(Y) code on both L1 and L2 frequencies, offering superior positioning accuracy compared to SPS.

1.2.3.2 GPS Modernization and New Signals

New satellites are being developed as part of the ongoing GPS modernization program to send more signals, which should enhance accuracy and reliability. Several new signals for military and civilian use are introduced by this modernization on the L1, L2, and new L5 frequency bands [4, 33–35]:

- **L2 Civil (L2C) and Military (M) Code:** Satellites from the Block IIR-M series broadcast the L2C signal, giving users a stronger way to correct ionospheric errors than the older L1 CA code. This newer signal also transmits at a higher power, does

so without interfering with the CA code, and incorporates security features such as limited access, authentication, and data privacy, making it a natural replacement for the older PY code in military systems.

- **L5 Signal:** Broadcast by Block IIF satellites, the L5 signal (1176.45 MHz) is designated for safety-of-life civil applications .
- **L1 Civil (L1C) Signal:** Currently in the design phase for Block III satellites, the L1C signal is based on the BOC waveform, or its optimized form, MBOC. This waveform was adopted following a 2004 agreement on GNSS cooperation between the United States and the European Union.

1.2.4 Other Global Satellite Positioning Systems

Beyond GPS, other satellite positioning systems are now fully operational, being upgraded, or are rapidly transitioning from design to launch. Together, these networks enhance the global navigation backbone, making location services sharper, stable, and more resilient to jamming or blocking. This section details GLONASS from Russia, Galileo operated by Europe, and China's BeiDou constellation [36].

1.2.4.1 GLONASS

GLONASS, Russia's satellite navigation system, follows a different path from GPS and has undergone significant evolution since its launch. Its entire system first went live in 1996 with 24 satellites in orbit, comprising 21 active and three backup satellites. These crafts are split among three orbital planes, flying at about 19,100 kilometers with an inclination of 64.8°. Each takes roughly 11 hours and 15 minutes to complete one circuit, so the ground track repeats every eight days. In the past, GLONASS used the PZ-90 reference frame, meaning users wanting to mix GLONASS and GPS data had to convert to WGS84 first [37].

Similar to GPS, GLONASS has provided both civil and military services. A key distinguishing feature of early GLONASS was its use of Frequency Division Multiple Access (FDMA), meaning each satellite transmitted its navigation message on a unique frequency [37]. Ground control stations across Russia were responsible for transmitting corrections to the satellites.

After the dissolution of the Soviet Union, budget cuts severely affected GLONASS, and by 2000, the constellation had been reduced to only six working satellites. Since then, a steady modernization push has breathed new life into the system. A series of

GLONASS-M satellites, labeled the Modified version, have been orbited, and these units utilize the PZ-90.02 reference frame, which roughly matches WGS-84, making it easier for users to combine GLONASS data with GPS and, eventually, Galileo. Work is now focused on the upcoming GLONASS-K birds, which will add CDMA signaling and further sharpen interoperability with other GNSS [36–38].

1.2.4.2 Galileo

Europe's independent global satellite navigation system is Galileo. Developed to eliminate reliance on the US military-controlled GPS, the system began offering initial services around 2014. Galileo is designed with a constellation of 30 satellites, positioned in three circular Medium Earth Orbit (MEO) planes at an altitude of 23,222 km, with an inclination of 56 degrees. Each satellite has a revolution period of 14 hours and 21 minutes, resulting in a 10-day repeat cycle of its ground track. Galileo satellites carry two types of exact atomic clocks: rubidium and hydrogen maser [36].
A unique characteristic of Galileo is its inherent design as a civilian-controlled system and its emphasis on transmitting integrity information within its navigation messages. Galileo provides five distinct services, some free and others paid [39–41]:

- **Open Service (OS):** The basic, free service, analogous to current civilian GPS use, providing standard positioning.
- **Commercial Service (CS):** This service is a subscription-based offering that improves positioning accuracy, reliability, and availability.
- **Safety of Life (SoL) Service:** Developed for safety-critical operations, it delivers high-integrity assurances using signal authentication, formal certification, and contractual service levels.
- **Public Regulated Service (PRS):** Access is limited to authorized government users engaged in missions that demand superior performance and benefit from jamming-resistant signals.
- **Search and Rescue (SAR) Service:** Intended for locating emergency beacons, the capability works seamlessly with the current COSPAS-SARSAT network.

Galileo satellites broadcast six unique signals-E1, E5a, E5b, and E6-across three leading frequency bands: E5 (1164 MHz to 1215 MHz), E6 (1200 MHz to 1300 MHz), and E2-L1-E1 (1556 MHz to 1592 MHz) [42]. Some of these signals are also paired with quadrature-phase replicas that carry no user data. For every navigation service offered by

Galileo, a specific mix of these signals is employed, as outlined in Table 1.1. An important design goal was interoperability; therefore, the overlapping channels allow Galileo to work seamlessly with existing GPS and GLONASS services.

table 1.1: Distribution of Different Signals for Each Service.

Service	Signals
OS	E1, E1Fp, E5A, E5B, E5Ap, E5Bp
CS	E1, E1Fp, E6B, E6Bp, E5A, E5B, E5Ap, E5Bp
SoL	E1, E1Fp, E5A, E5B, E5Ap, E5Bp
PRS	E6A, E1P

The control segment of the Galileo system is supported by a worldwide array of ground facilities, which include:

- two dedicated control centers;
- five Tracking, Telemetry and Control (TTC) stations;
- ten data upload stations that send information to the satellites;
- forty signal reception sensor stations that monitor the broadcast;
- one specialized integrity center that verifies system accuracy.

All these stations are geographically distributed worldwide. Galileo was conceived to provide a more secure and precise civilian positioning system, particularly oriented towards transportation applications, and is designed to operate in conjunction with augmentation systems. The future combined use of GPS and Galileo's 30 additional satellites is expected to yield significantly improved accuracy, availability, and continuity of service, enabling more robust GNSS-based applications [36].

1.2.4.3 BeiDou

China's home-grown satellite navigation network, known as the BeiDou Navigation Satellite System, was once branded COMPASS in early public releases. BeiDou is engineered to deliver worldwide positioning and timing by deploying a mix of satellites circling in MEO and those stationed in Geostationary Earth Orbit (GEO). The project initially set 2013 as the target year for a regional service, yet full global functionality was realized around 2020. Satellites in the MEO leg fly at roughly 21,000 km, trace an orbit tilted at 55°, and complete a pass over Earth in about 12 hours. To meet diverse user needs, BDS offers a free civilian service, promising 10-meter positioning, and a more precise, encrypted option reserved for military customers [43, 44].

1.3 GNSS Compatibility and Interoperability

In many practical situations, relying on just one GNSS fails to deliver the best possible position, navigation, and timing data, even when compared to stand-alone GPS-GNSS. Urban canyons, densely built railroad corridors, and mountain valleys all block or reflect signals, creating MP and temporary lock-outs. The arrival of Galileo, the steady rollout of BeiDou, and ongoing upgrades to GPS and GLONASS heighten interest in how well these systems work side by side, and scholars increasingly focus on compatibility and interoperability as key design goals [45].

1.3.1 GNSS Compatibility

Compatibility ensures that each constellation can be switched on in the same region without harming another's signals. It requires careful engineering of frequencies, bandwidths, signal structures, and power levels so that one set of satellites does not drown out or distort what the next set is trying to transmit. Because the leading operators have paid close attention from the start, the major GNSS constellations are, in theory, compatible by design [45, 46].

1.3.2 GNSS Systems Interoperability

Interoperability refers to a situation where different GNSS constellations work together in a manner that the combined performance exceeds what any single system could achieve alone. For users, this advantage becomes apparent when a receiver locks onto signals from multiple satellites simultaneously, which speeds up location fixes, sharpens accuracy, and extends coverage even in challenging areas. Over recent years, the service communities have hammered out a set of technical and policy pacts that line up signal layouts, timing codes, and data formats. As a result, people with modern dual- and triple-frequency units are now enjoying the smooth, worldwide positioning service that combines GPS, Galileo, GLONASS, and BeiDou [45–47].

1.3.3 GNSS Signal Interoperability

Signal interoperability exists when different GNSS signals look alike enough that a Multi-Constellation, Multi-Frequency (MC/MF) receiver can tweak a few processing settings and still produce a PVT solution. This commonality cuts down both the design effort and the bill of materials for MC/MF receivers [48].

Looking at current and planned signals, each GNSS offers at least three separate frequency channels. One of the most widely used frequencies across GPS, GLONASS, Galileo, and BeiDou is 1575.42 MHz. Soon, 1176.45 MHz is expected to be seen on all four systems, while 1207.14 MHz is already available on three. Modernization proposals for GLONASS also call for open CDMA beacons on 1575.42, 1176.45, and 1207.14 MHz, which are meant to match GPS-L5, GPS-L1C, and the Galileo-/BeiDou E1, E5a, and E5b signals [38, 45–47]. Figure 1.5 shows those allocations and overlaps visually.

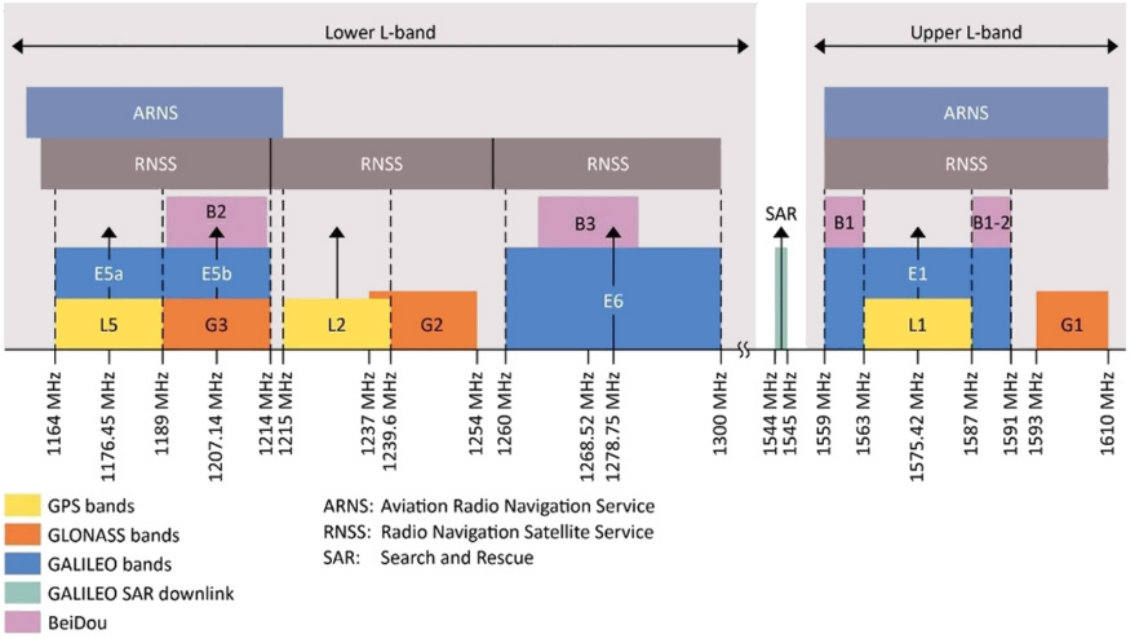

figure 1.5: Frequency bands [49].

The five frequencies currently in use or planned across GPS, Galileo, GLONASS, and BeiDou (1176.45 MHz, 1207.14 MHz, 1227.60 MHz, 1278.75 MHz, and 1575.42 MHz) are all based on a fundamental frequency of $f_0 = 10.23$ MHz, with multiplication factors of 115, 118, 120, 125, and 154, respectively. Additionally, GNSS signals employing BOC, BPSK, or QPSK modulations contribute to interoperability. Since QPSK can be treated as BPSK, GPS, GLONASS, Galileo, and BeiDou can be considered signal-interoperable within specific frequency bands (for example, L1, E1, and B1). However, significant differences in navigation message structures can complicate multi-GNSS signal processing, potentially increasing the required program memory for MC/MF receivers [46, 50].

Finally, while most global clocks are synchronized to UTC, individual GNSS atomic clocks operate on their internal time systems. Galileo System Time (GST) is based on

International Atomic Time (IAT), and BeiDou Time is its reference. In contrast, GPS System Time (GPST) and GLONASS System Time (GLONASSST) are based on the U.S. and Russian versions of UTC, respectively. GNSS service providers have agreed to broadcast the necessary time offsets, which receivers can then apply to their measurements to ensure accurate positioning. Some receivers can also isolate this time offset as an additional unknown to be solved within the navigation solution. Consequently, all GNSS are considered interoperable in terms of time synchronization [46, 50].

1.4 Pseudolites System

PL systems are ground-or airborne transmitters that broadcast signals mimicking GNSS code patterns, enabling well-equipped receivers to compute PVT in real-time. Because they generate strong, controlled signals, PL can penetrate dense urban architectures, indoor spaces, and steep canyons where conventional satellite visibility is poor or absent, thus serving as an essential supplementary or fallback guidance source. Their benefits include high transmit power, configurable geometric spread, and the potential for multi-meter positioning accuracy under favorable conditions. When four or more stations are networked, they can yield a standalone positioning solution, guaranteeing uninterrupted location tracking in GNSS-denied zones and supporting the accelerating demand for dependable, continuous location-based services [6–8].

1.4.1 Pseudolites System Classifications

PL systems have been researched and field-tested in a variety of environments where GNSS signals are weak, intermittent, or blocked. Such settings often include large indoor complexes, long tunnels in deep open-cut mines, busy container terminals along the coast, and crowded city blocks where many tall buildings obstruct satellite lines of sight. From an engineering perspective, existing studies usually distinguish between two broad categories of PL architecture, depending on whether the signal source is stationed on the ground or carried overhead: Ground-Based PL (G-PL) and Airborne PL (A-PL) [51].

1.4.1.1 G-PL System

G-PL technology dates back to the late 1970s, a period that predates the full deployment of GPS. The earliest working prototype utilized a network of stationary ground stations that broadcast signals resembling the GPS L1 waveform, enabling early receivers to combine these transmissions with satellite data for position fixes (Figure 1.6). By the mid-1980s,

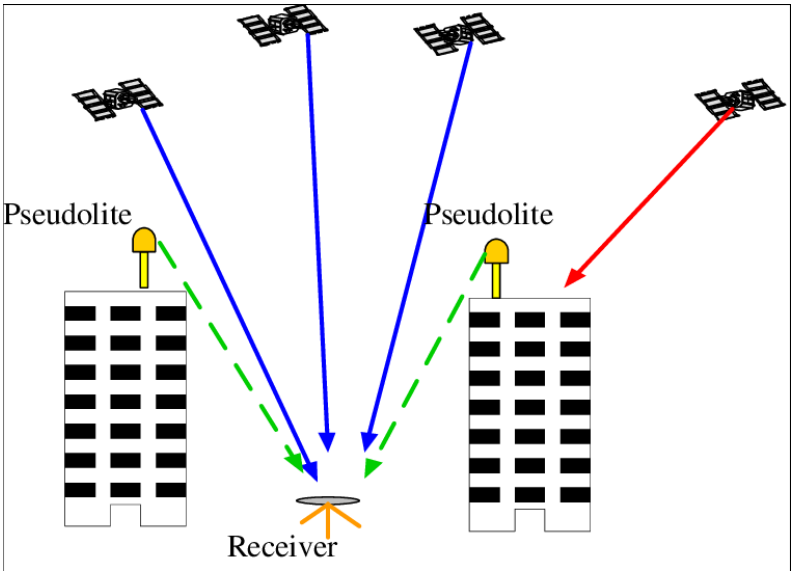

figure 1.6: G-PL positioning system [52].

the Radio Technical Commission for Maritime Services (RTCM) published a set of signal standards that prevented the new broadcasts from interfering with adjacent-GPS channels. Central to this specification, Message Type 8 carries the PL almanac and relays critical parameters such as satellite geometry and signal health. Collectively, these refinements have established G-PL as a complementary technique that boosts the availability, reliability, integrity, and accuracy of GNSS applications. Interest surged during the 1990s when engineers adopted G-PL for high-precision navigation and positioning [6–8, 51].

Stanford University has suggested placing G-PL along an aircraft's final descent path to clarify carrier phase ambiguities and make precision landings more reliable. The same G-PLs could enhance GPS-driven deformation-monitoring networks by providing additional range data that accelerates ambiguity resolution and improves overall positioning accuracy. Unlike orbiting GPS satellites, however, each fixed G-PL must be carefully calibrated to the particular conditions and constraints of its chosen site [6–8, 51].

1.4.1.2 A-PL System

To address a few limitations that still arise with G-PL, researchers have suggested using A-PL systems. Essentially, beacons are mounted on planes, airships, or other flying hardware. The first serious push for A-PL work can be traced back to 1996, when teams attempted a reverse positioning mode that treated the ground receivers as having fixed, well-surveyed locations. By the early 2000s, those efforts merged with High Altitude Platform Systems (HAPS) and Stratospheric Platforms (SPFs) were put forward as a way to raise GPS accuracy, coverage, and reliability over broad stretches, even an entire nation.

One prominent example came from the Europe's HeliNet project, which pictured High Altitude Long Endurance (HALE) solar-powered drones, sometimes called stromatolites, at around 17 kilometers, broadcasting differential corrections along with GNSS-like ranging pulses. The real effectiveness of such an architecture hinges on knowing the drone's position precisely, for which options like code-phase differential GPS or kinematic carrier-phase techniques have been proposed [53].

The concept evolved to include mobile A-PL at high altitudes due to their flexible deployment features and extensive LOS coverage. Their use as mobile PLs ignited the need for real-time positioning, giving rise to concepts like trilateration with bidirectional range measurements. However, achieving accurate real-time A-PL positioning remains a significant challenge. Common "inverted-GPS" methods using ground monitoring stations can introduce additional performance degradation. The A-PL's dynamics, together with the rate of ephemeris transmission, integration period during user position fix calculations, and timing accuracy, affect the resultant positioning calculations derived from triangulated geometry depicting ground station coordinates. These factors also influence the precision of user position determination. Airborne relay-based systems have been created to manage some of the difficulties arising from A-PLs; however, they inevitably increase the difficulty of user position estimation and could diminish system robustness in failure cases involving ground reference stations [51].

1.4.2 Near-Far Issue

The Near/Far problem is a core issue with PL positioning systems because the ground-based transmitters sit much closer to users than the orbiting satellites used in traditional GNSS. Because received power drops with the square of the distance, moving only a few meters toward or away from a PL can change the signal strength by many decibels. For example, a receiver sitting 100 meters from a PL will see a signal almost 20 dB stronger than one that is 1 kilometer away. That huge swing in power, unlike the almost steady signals sent by space-borne GNSS satellites, makes it hard to build receivers that work well across a wide coverage area [6–9, 51, 53].

Consider a scenario such as an A-PL used to assist aircraft. As an airplane descends, its range to the G-PL varies dramatically, shifting from more than 32 km (20 nautical miles) to within a few meters near the runway threshold. Such a swing translates to an estimated 70 dB change at the aircraft receiver. At the exact moment the receiver is trying to lock onto faint satellite signals hovering around -130 dBm, the nearby PL can blast in at nearly -60 dBm [9].

That vast difference in signal power creates serious interference for GNSS receivers.

If the strong PL sends out a steady code, its peak power can easily exceed the cross-correlation limit of approximately 21.6 dB, and at closest approach, it can sit some 50 dB higher. Under those conditions, the receiver stops tracking real satellites and instead latches onto false cross-correlation peaks generated by the PL. In real-world operations, the overbearing PL can drown out weaker GNSS signals and even suppress other, farther PL transmissions as the aircraft gets closer. This well-documented phenomenon is known as the near/far problem, illustrated in Figure 1.7 [9].

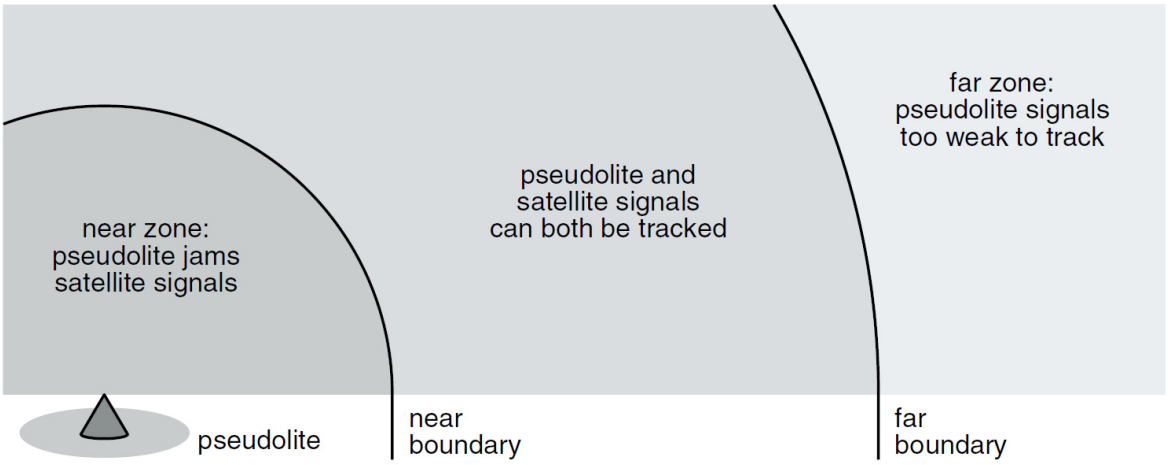

figure 1.7: Near/Far issue zones. [9].

Successful navigation relies on keeping the receiver in a well-defined operational zone bordered by two key limits. The outer, or far boundary, is set where the PL signal weakens enough that the satellite tracking becomes unreliable; the inner, or near boundary, marks the point at which an overly strong PL signal starts to overload the receiver and degrade accuracy. The exact position of the far boundary primarily depends on the PL's transmission power, which must be sufficiently strong to maintain the minimum detectable signal level at the receiver, typically around -130 dBm. In practice, however, the gap between the near and far limits depends less on fixed power values and more on the specific tracking margin built into the receiver's design. Tackling this interference situation, known as the near/far effect, therefore requires a range of targeted countermeasures that have been explored in the literature [6–9, 51, 53].

Researchers have advanced several strategies to mitigate the near/far problem in positioning systems. These strategies range from designing new spreading codes and fine-tuning power-level antenna hardware to deploying sophisticated interference-cancellation circuits [6, 8]. THMA pulse sequences have surfaced as the leading option in PL positioning systems, appearing in a growing number of studies on robust signal generation and channel management [6, 8, 13]. This popularity stems from the scheme's low power and

bandwidth overhead, as well as the limited mechanical changes required to retrofit current receivers. In practice, a THMA PL signal emerges by sweeping a steady, GNSS-like carrier with a pseudo-random train of time-hopped pulses [6,8]. The exact timings of those gaps follow a master time-code blueprint, often stored in a SIT, which lists multiple offset permutations [6,8,13]. A more detailed discussion of timing accuracy, slot strategies, and experimental performance can be found in the next chapter.

1.5 Positioning Error Sources

In GNSS, the quality of a user's computed location depends on three interrelated factors: the accuracy of satellite orbits, the precision of pseudo-range measurements, and the spatial configuration of visible satellites [14]. Collectively, these error sources can be summarized by the term User Equivalent Range Error (UERE), which, in turn, is scaled upward or downward by the satellite positional geometry as captured by the Dilution of Precision (DOP) metric.

It is essential to understand the principal sources of error that collectively affect the measurements obtained between the receiver and visible satellites [15,27]. Generally, User UERE can be decomposed into several distinct error types. These include ephemeris errors, which represent inaccuracies in the broadcast satellite orbit information; clock biases, arising from discrepancies in the timing of satellite and receiver clocks; and atmospheric delays caused by the signal's passage through the ionosphere and troposphere. Other significant contributors include MP effects resulting from interference caused by reflected signals, as well as inherent receiver noise and thermal noise generated within the receiver itself.

The pseudo-range measurement, denoted as $r_k^{(R)}$, is impacted by all these positioning error sources and can be expressed for the k-th satellite as:

$$r_k^{(R)} = \rho_k + c(T_s - T_u) + E_{sat,k} + E_{inos} + E_{tropo} + E_{MP} + E_{Br} \tag{1.8}$$

Where:

- ρ_k: Geometric distance between the receiver and the k-th satellite.
- c: Speed of light.
- T_s: Time of reception.
- T_u: Time of emission.
- $E_{sat,k}$: Error in the position of the k-th satellite (combining ephemeris and satellite clock errors).
- E_{inos}: Ionosphere error corresponding to the k-th satellite.

- E_{tropo}: Troposphere error corresponding to the k-th satellite.
- MP effects (E_{MP}): Error caused by MP.
- Receiver noise (E_{Br}): Error caused by receiver noise.

The final positioning accuracy of a GPS receiver is ultimately achieved by multiplying the UERE by an appropriate DOP value [14, 54]. A brief description of these errors and their properties will be provided in the subsequent sections of this chapter. This work will particularly focus on the effects of MP and receiver noise.

1.5.1 Ephemeris Error

Ephemeris errors occur when the navigation message sent by a GNSS fails to match the satellite's true orbital path. Usually, the radial component that runs directly along the LOS to the receiver is the smallest part of the discrepancy. Much larger errors tend to appear in the tangential and transverse directions, which lie perpendicular to the radial line, and those can be roughly ten times bigger. Happily, these bigger components still matter less for overall positioning quality than the radial error does. To reduce the problem, the GNSS control segment carefully gauges each satellite location and then uploads fresh ephemeris data to the spacecraft on a regular schedule [15, 27, 46, 50].

1.5.2 Ionosphere

The ionosphere forms an elevated layer in Earth's atmosphere, extending from approximately 60 km to about 1000 km above the Earth's surface. There, incoming solar wind and high-energy radiation knock electrons loose from gas molecules, creating a patchwork of free charges. These charges alter the speed at which GNSS signals propagate through the region. Because of this, the arrival of a signal at a receiver's antenna is slowed, and engineers label this ionospheric delay, which skews the actual travel time [10, 55]. Left uncorrected, the delay can push position fixes off by several tens of meters, with the size of the error swinging on the satellite elevation angle and current ionospheric state, especially during peak solar periods [10, 27, 55]. Such a significant bias weakens many applications, particularly those that use only a single frequency. To lessen the problem, a range of correction models has been devised. One of the most accessible, the Klobuchar model [11], relies on parameters sent in the GNSS navigation message to roughly predict and offset part of the delay.

Furthermore, the ionosphere is a dispersive medium, meaning that its influence on a radio signal varies with frequency. This characteristic is essential for modern receivers; when pseudo-range measurements are gathered at two distinct carrier frequencies, the

frequency-dependent ionospheric error essentially cancels out. By combining these dual-frequency observations, the ionospheric delay on frequency I^k_{f1} for satellite k can be approximated through the equation given in [11]:

$$I^k_{f1} = \frac{f_2^2}{(f_1^2 - f_2^2)}(\rho^k_{f2} - \rho^k_{f1}) \tag{1.9}$$

Where:

- k: Indicates the satellite number.
- f_1, f_2: Represent the two different carrier frequencies.
- ρ^k_{f1}, ρ^k_{f2}: Are the pseudorange measurements obtained for satellite k on frequencies f_1 and f_2, respectively.

1.5.3 Troposphere

The troposphere is the atmospheric layer closest to the Earth, reaching roughly 10 kilometers above the surface. Made up mostly of dry air mixed with water vapor, the troposphere slows down GNSS signals much as the ionosphere does. This slowdown adds extra time to the calculated travel path, creating a bias in how long receivers think the signals have been in the air. Both the pseudorange and the carrier-phase measurements suffer from this delay equally. The size of the tropospheric error varies with local weather, depending on temperature, pressure, and the amount of moisture in the air. Unlike the ionosphere, the tropospheric error does not change much with different radio frequencies. Though still important, the delay caused by the troposphere is usually smaller than the problems brought by the ionosphere [10, 12, 55]. To minimize tropospheric errors, GNSS receivers typically employ multiple atmospheric models. These models calculate the tropospheric delay based on input data, including real-time readings of pressure, temperature, and water vapor. Other approaches, however, depend on location-specific averages of these variables that have been recorded over more extended periods [56].

1.5.4 Doppler Effect

In GNSS, the Doppler effect arises from the relative motion between a transmitting satellite and the user's receiver. When a satellite travels toward the receiver while broadcasting a signal, the frequency detected by the receiver is pushed higher than the frequency that left the satellite; if the satellite moves away, the observed frequency drops. The size and direction of the shift depend on the original signal's frequency and the component of the relative speed along the LOS between emitter and receiver [57].

The resulting Doppler frequency shift (Δf) is mathematically given by [57]:

$$\Delta f = f_r - f_e = -\frac{v_r}{\lambda} \tag{1.10}$$

Where:

- f_r: Is the received frequency.
- f_e: Is the emitted frequency.
- λ: Is the wavelength of the signal.
- v_r: Is the relative speed between the emitter and the receiver (positive when receding, negative when approaching).

For a typical ground-based receiver, the Doppler frequency shift can vary by nearly ±10 kHz. In contrast, spaceborne receivers designed for demanding missions may experience shifts well beyond that, approaching ±50 kHz [57].

1.5.5 Multipath

MP propagation is a major error source in GNSS receivers, particularly in dense urban areas and similar environments where LOS signals are often obstructed. In such conditions, the navigation signal reaches the antenna via multiple paths reflected or diffracted by nearby surfaces such as glass façades, pavements, or low-roofed structures [17,18]. The received waveform thus becomes a composite of the direct LOS component and several delayed, attenuated reflections, each distinguished by its timing, power, and phase offset relative to the uncorrupted path, as illustrated in Figure 1.8.

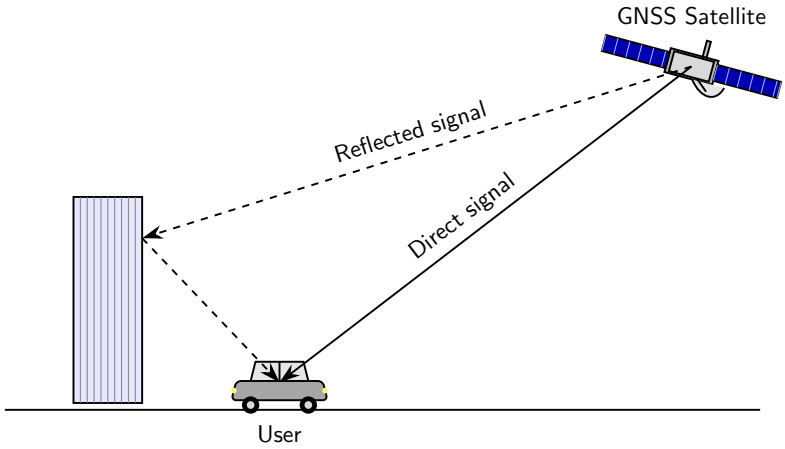

figure 1.8: LOS and MP reception in an urban GNSS scenario.

Reflected signals clutter a receiver's tracking performance, primarily corrupting the accuracy of both code loops and carrier-phase loops. Interference from these MP echoes

skews the estimated delay and phase of the LOS signal, creating sizable errors in pseudo-range readings-evidence of the problem is particularly clear in crowded urban canyons [17]. The properties of the MP environment, delays, phases, and the sheer number of visible paths fluctuate continually because of relative motion between transmitter and receiver as well as moment-to-moment changes in nearby buildings or vehicles [17, 18]. When a receiver locks onto a bounced echo rather than the clean direct wave, the position fix may drift severely or fail, leaving the user without usable location data.

Ongoing studies continue to investigate how MP fading affects global navigation signals, thereby biasing position fixes. Work in this area falls into two broad, though complementary, streams:

- **Antenna Processing Methods:** Adaptive arrays and smart antennas shape the radiated beam so that echoes from walls and nearby objects are quietly nulled rather than amplified, improving front-facing reception [58, 59].
- **Signal Processing Methods:** Here, either a hardware or firmware module estimates the echoes delay, phase, and power in near real-time and then subtracts them, or new code-phase and carrier-phase trackers work through the noise instead of being overpowered by it [19].

The detailed effect of MP on GNSS receiver performance, particularly on the ACF and the S-curve of the DLL, will be explored in depth in the following chapters.

1.5.6 Signal-to-Noise Ratio

Weak GNSS signals can undermine the precision of positioning solutions. A key indicator of how good a received signal is the Signal-to-Noise Ratio (SNR), which measures how the sound signal stands up against the ambient noise.

Mathematically, SNR equals the power of the signal, P_s, divided by the power of the noise, P_n, and engineers often report it in decibels (dB) using the formula [15, 27]:

$$\mathrm{SNR}_{dB} = \left[\frac{P_s}{P_n}\right]_{dB} = 10\log_{10}\left[\frac{P_s}{P_n}\right] \tag{1.11}$$

When the SNR is high, the signal overwhelms the noise, allowing users to obtain steadier and more accurate position fixes.

1.6 Conclusion

This chapter provided a comprehensive overview of GNSS, establishing the core principles of satellite navigation by outlining the standard three-segment architecture and explaining

position determination through geometric trilateration with pseudorange measurements. A detailed survey of the four primary global constellations (GPS, GLONASS, Galileo, and BeiDou) highlighted their unique characteristics and modernization efforts, emphasizing the growing importance of system compatibility and signal interoperability for enhanced performance.

The review of positioning technologies was extended to include PL systems, presented as a vital supplement to GNSS in environments where satellite signals are weak or unavailable. This section explored both Ground-Based and Airborne configurations while conducting a critical analysis of the persistent near-far problem. A systematic analysis of the primary sources of positioning error provided essential context for understanding real-world performance limitations, covering satellite-dependent errors, atmospheric propagation delays, and signal-level impairments like receiver noise and MP interference.

By thoroughly dissecting these fundamental concepts and error sources, this chapter establishes the necessary theoretical groundwork for the advanced topics in subsequent chapters, which will focus on developing robust signal processing techniques to mitigate these errors and improve positioning performance.

Chapter 2

GNSS and Time-Hopping Pseudolite Signals Design

2.1 Introduction

This chapter builds on the principles introduced in Chapter 1 to explore the detailed design of signals for GNSS and PL systems. The architecture of a signal is crucial to achieving superior navigation performance, enabling global interoperability and resolving localized issues, such as the near-far problem. To this end, the chapter examines the sophisticated modulation techniques of modern GNSS and introduces THMA as a specialized solution of the near-far issue for PL systems.

To achieve this objective, the chapter will begin by explaining the elementary components of DSSS, PSD, ACF, and GNSS signals, as well as data spreading. The chapter will also cover the critical types of GNSS modulation (BPSK, BOC, MBOC, BSC) and provide detailed ACF and PSD analyses. Next, a cross-comparative analysis of various GNSS signals will be presented to provide the foundational understanding required for the complex signal processing techniques used in advanced navigation systems. Lastly, the THMA in PL will be explained in terms of its pulsing scheme and SIT generation methods.

2.2 GNSS Signal Components and Characteristics

2.2.1 Direct Sequence Spread Spectrum

All existing GNSS rely on the DSSS technique as their fundamental signal structure. The reasons for using DSSS in satellite navigation are twofold. First, DSSS helps con-

vert narrowband information signals into wideband, noise-like signals, which enhance the systems' robustness against purposeful or inadvertent interference during signal transmission. Second, DSSS facilitates CDMA, allowing several satellites to broadcast simultaneously within a single frequency range, differentiated only by their unique spreading codes [5, 29, 60].

DSSS works by multiplying an information data signal (usually given as binary symbols $(-1, 1)$ with a PRN sequence. This sequence code is still marked with binary digits of $\{-1, 1\}$. Moreover, the chip rate is much faster than the data symbol rate. As a result, the spread spectrum signal now has a far greater frequency span. The chip rate of the PRN code mainly constrains its bandwidth (figure 2.1).

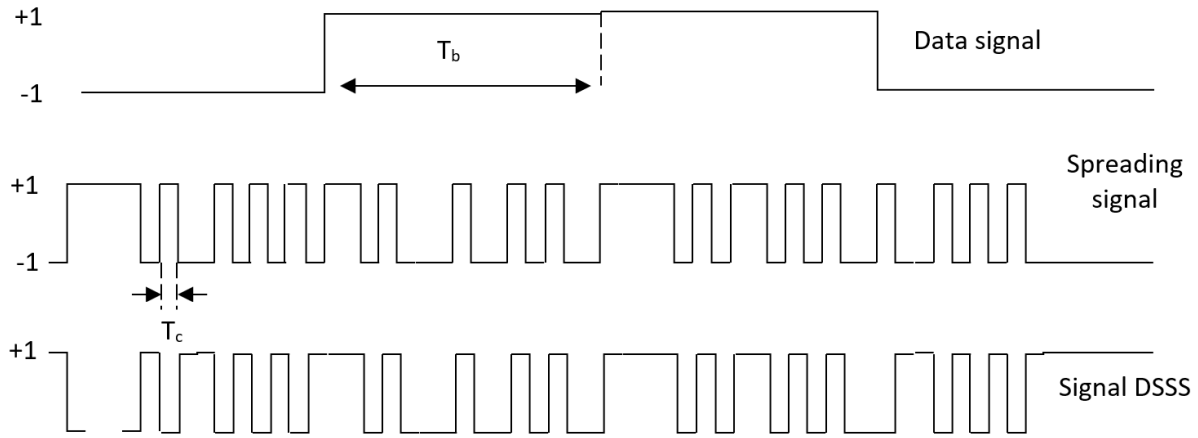

figure 2.1: Baseband DSSS signal.

Mathematically, the PRN code signal, $c(t)$, and the data signal, $b(t)$, can be represented as baseband digital signals as follows [61, 62]:

$$c(t) = \sum_{i=-\infty}^{i=+\infty} c_i u_{T_c}(t - iT_c) \tag{2.1}$$

$$b(t) = \sum_{j=-\infty}^{j=+\infty} b_j u_{T_b}(t - jT_b) \tag{2.2}$$

Here, $\{c_i\}$ and $\{b_j\}$ represent the PRN code symbols and data symbols, respectively, each taking values from the set $\{-1, 1\}$. $u_{T_c}(t)$ and $u_{T_b}(t)$ denote rectangular pulses of unit amplitude with durations T_c (chip duration) and T_b (bit duration), respectively.

Out of the various types of PRN sequences, Gold codes are one of the most preferred

in GNSS due to their unique properties in correlation metrics [63, 64]. A Gold code is produced from the exclusive OR (XOR) operation of two maximal length sequences (m-sequences) of the same length and rate. A complete family of Gold codes can be derived by taking one of the primary sequences and combining it with all possible cyclic shifts of the other. Perhaps two of the most important features of these codes, which are vital for their effectiveness in CDMA systems, are their superior correlation properties:

- The normalized ACF of a Gold code sequence exhibits four distinct possible values. For a Gold code of length $L = 2^n - 1$, where n is the shift register size, these values are:
$$R_c(\tau) \in \left\{1, \frac{-1}{L}, \frac{-\beta(n)}{L}, \frac{\beta(n)-2}{L}\right\} \tag{2.3}$$
- For any two distinct Gold codes from the same family, the normalized cross-correlation function takes on three possible values:
$$R_{c_i,c_j}(\tau) \in \left\{\frac{-1}{L}, \frac{-\beta(n)}{L}, \frac{\beta(n)-2}{L}\right\} \tag{2.4}$$

In the functions shown above, $\beta(n)$ takes the value of $1 + 2^{(n+2)/2}$ for even values of n and $\beta(n) = 1 + 2^{(n+1)/2}$ for odd values. These correlation values are optimal in that they reduce the satellite signal interference. L is the length of the gold code.

2.2.2 Power Spectral Density and Autocorrelation Function

The Power Spectral Density (PSD) and the Autocorrelation Function (ACF) are essential for evaluating the performance of a GNSS signal. These two functions are related as a Fourier Transform pair, as stated in the Wiener-Khintchine theorem [65, 66]. The PSD, $S_{sig}(f)$, of a DSSS signal $sig(t)$ can be obtained from its ACF $R_{sig}(\tau)$, as follows:

$$S_{sig}(f) = \int_{-\infty}^{+\infty} R_{sig}(\tau) e^{-j2\pi f\tau} \mathrm{d}\tau \tag{2.5}$$

Conversely, the ACF is obtained from the PSD:

$$R_{sig}(\tau) = \int_{-\infty}^{+\infty} S_{sig}(f) e^{j2\pi f\tau} \mathrm{d}f \tag{2.6}$$

Where $R_s(\tau)$ is the ACF of $sig(t)$.

Similarly, the spreading code signal's PSD is given by [65]:

$$S_c(f) = \frac{|U(f)|^2}{T_c} \sum_{k=-\infty}^{k=+\infty} R_c(k) e^{-j2\pi f k T_c} \tag{2.7}$$

Here, U(f) is the Fourier transform of the waveform u(t), and $R_c(k)$ is the ACF of $\{c_k\}$, defined as $\mu[c_n c_m]$, which represents the static mean of x. Assuming ideal PRN code properties (ACF approximated by Dirac impulses $\delta(k)$ [65]), the PSD simplifies as follows:

$$S_c(f) = \frac{|U(f)|^2}{T_c} \tag{2.8}$$

For practical purposes, the PSD and ACF of GNSS signals are often expressed in terms of normalized values relative to the power of the signal after the signal has been processed by an ideal rectangular band-pass filter with bandwidth B. The normalized PSD, $\bar{S}_{sig}(f)$ is given as follows:

$$\bar{S}sig(f) = \frac{S_{sig}(f)}{\int_{-B/2}^{B/2} S_{sig}(f)\mathrm{d}f} \tag{2.9}$$

The corresponding normalized ACF, $\bar{R}sig(\tau)$, is:

$$\bar{R}_{sig}(\tau) = \int_{-B/2}^{+B/2} \bar{S}_{sig}(f) e^{j2\pi f\tau}\mathrm{d}f \tag{2.10}$$

2.2.3 CA Code

The CA code is a PRN code explicitly used by the GPS for its SPS offered to civilians on the L1 frequency. This code is a Gold code of length $L_c = 1023$ chips, which corresponds to $n = 10$ in the shift register generation, with a period of 1 millisecond and a chip rate of 1.023 MHz [67, 68].

The CA code sequence has some specific correlation properties due to its 1023 available chips ($n = 10$):

$$\bar{R}_C(\tau) \in \left\{1, \frac{-1}{L_c}, \frac{-65}{L_c}, \frac{63}{L_c}\right\} \tag{2.11}$$

$$\bar{R}_{C_i,C_j}(\tau) \in \left\{\frac{-1}{1023}, \frac{-65}{1023}, \frac{63}{1023}\right\} \quad (i \neq j) \tag{2.12}$$

The normalized ACF of the CA code (figure 2.2) exhibits a pronounced peak at the center and negligible secondary peaks, especially under the assumption of independent chip processing. Due to these properties, it is possible to approximate the ACF of the code with a Dirac impulse function, thereby greatly simplifying receiver processing.

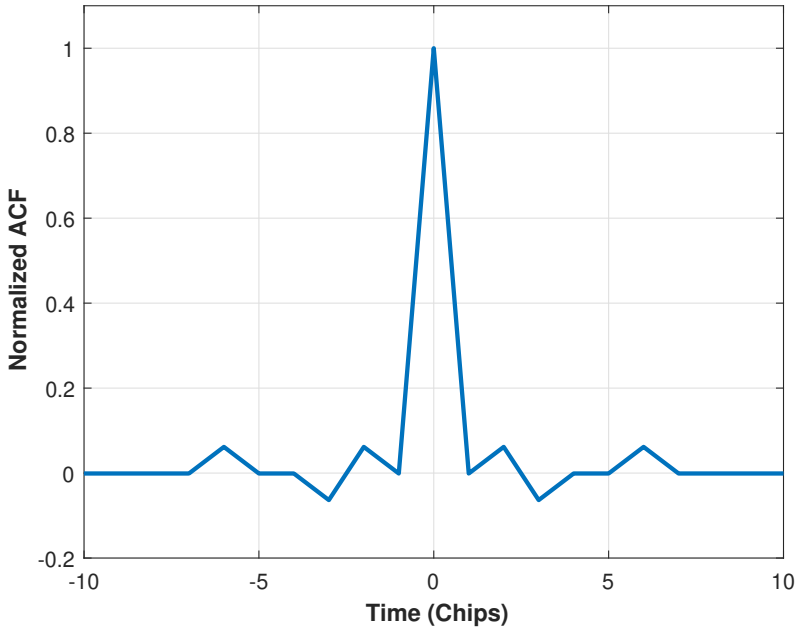

figure 2.2: Normalized ACF of the CA code.

2.3 GNSS Modulation Schemes

2.3.1 BPSK Modulation

BPSK is a fundamental digital modulation technique widely used in satellite navigation. It is characterized by the reception of binary data as two symbol levels, usually $\{-1, 1\}$ [2, 15, 27, 69]. This scheme affects a 180° phase shift in the resultant signal due to binary input bit change resulting in the echo signal as shown in Figure 2.3. The BPSK signal has a constant envelope and with phase continuity [2, 15, 27, 69].

In GNSS systems, the BPSK phases modulate the DSSS signal. For chip rates as $c_r \times f_0$ with $f_0 = 1.023$ MHz as the reference frequency, the BPSK signal is represented as $s_{BPSK(cr)}(t)$. It can be expressed as the product of the data signal $d(t)$, the PRN spreading code $c(t)$, and a sinusoidal carrier signal [69].

$$s_{BPSK(c_r)}(t) = b(t) \cdot c(t) \cdot \cos(2\pi f_p t + \theta) \tag{2.13}$$

In this case, f_p denotes the carrier frequency, while θ indicates the initial phase. This modulation technique is well known and, as mentioned in Chapter 1, has been used in GPS for the transmission of legacy CA and P(Y) codes.

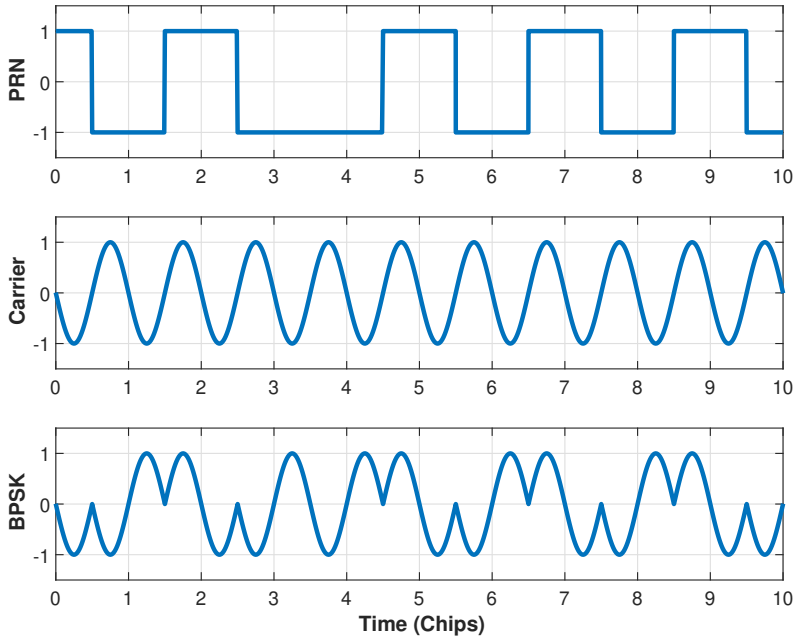

figure 2.3: BPSK Modulation.

2.3.1.1 ACF of the BPSK Signal

Neglecting the data signal and assuming ideal PRN code properties, the normalized ACF for the baseband BPSK(c_r) signal is presented in Figure 2.4 and described in [15].

$$R_{BPSK(c_r)}(\tau) = \begin{cases} 1 - \frac{|\tau|}{T_c} & \text{if } |\tau| < T_c \\ 0 & \text{elsewhere} \end{cases} \tag{2.14}$$

We note that the triangular peak of the isosceles triangle BPSK ACF is dominated by a single peak. This peak is the result of perfect alignment between the received code and the locally generated code at the GNSS receiver.

2.3.1.2 PSD of the BPSK Signal

The PSD of the baseband BPSK signal, denoted as $S(f_c)$, is given by:

$$S(f) = f_c \left(\frac{\sin(\pi f / f_c)}{\pi f} \right)^2 \tag{2.15}$$

Where f_c is the chip rate. As shown in Figure 2.5, the normalized PSD for the BPSK signal illustrates that most of the spectral energy is concentrated in the prominent main lobe. It is easy to see that the PSDs of BPSK-modulated signals capture most of their spectral energy within a singular, distinctive primary lobe that stands apart from several other adjacent lobes. The width of the primary lobe is approximately two times the chip

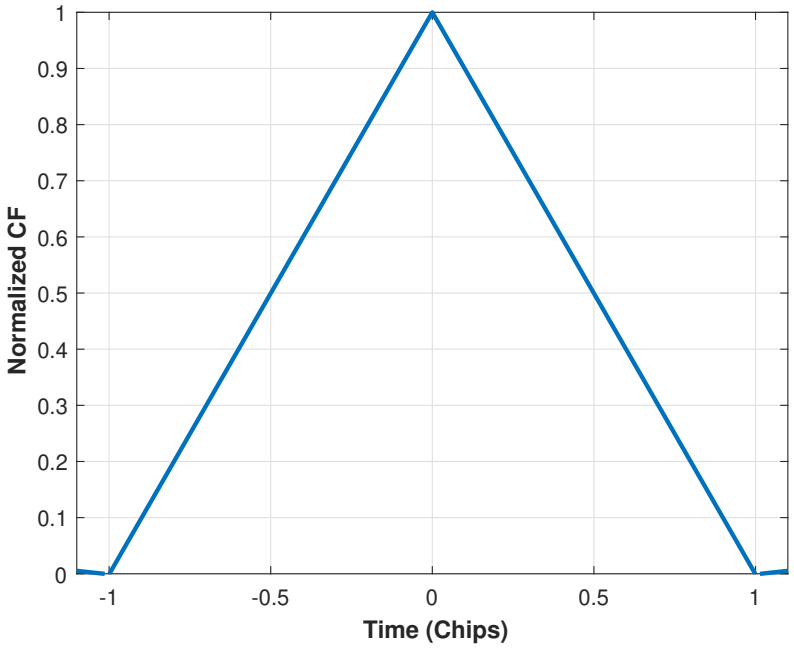

figure 2.4: BPSK ACF.

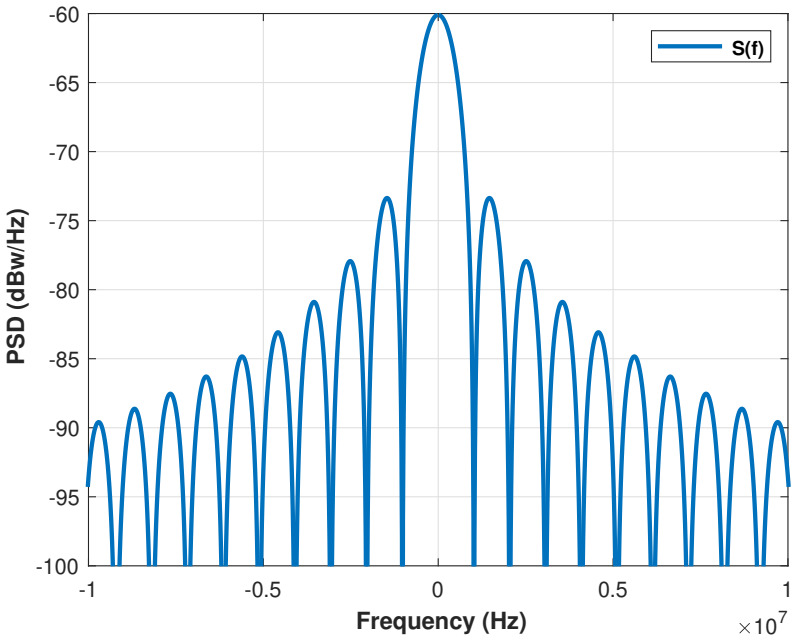

figure 2.5: BPSK PSD.

rate of the spreading code.

2.3.2 BOC Modulation

A critical technique in GNSS is the BOC-modulated signal, which involves multiplying the PRN code by a subcarrier signal. The latter is obtained from the sign of a sinusoidal

or cosinusoidal waveform. BOC signals are often referred to as BOC(m, n) where $f_{sc} = m \cdot f_0$ and $f_x = n \cdot f_0$ (subcarrier frequency and chipping rate, respectively). The BOC modulation order is given as $M = (2m/n)$ [20–22]. The envelope of the modulated signal BOC(m, n, φ) contains φ, which represents the phase of the BOC modulation and encodes the PRN code $c(t)$ onto a subcarrier waveform, resulting in the standard offset carrier structure. It can be expressed as:

$$\text{BOC}(m, n, \varphi) = c(t/T_x)\,\text{sign}[\cos(\pi t/T_{sc} + \varphi)] \tag{2.16}$$

In this expression, sign$[\cdot]$ is the signum (or sign) function, T_x designates the chip duration ($f_x = 1/T_x$), and T_{sc} denotes the subcarrier's half period, notating $f_{sc} = 1/2T_{sc}$. The parameter φ assigns the subcarrier's phase: BOC$_s(m, n)$ = BOC$(m, n, \varphi = \pi/2)$ for sine-phase and BOC$_c(m, n)$ = BOC$(m, n, \varphi = 0)$ for cosine-phase [20–22].

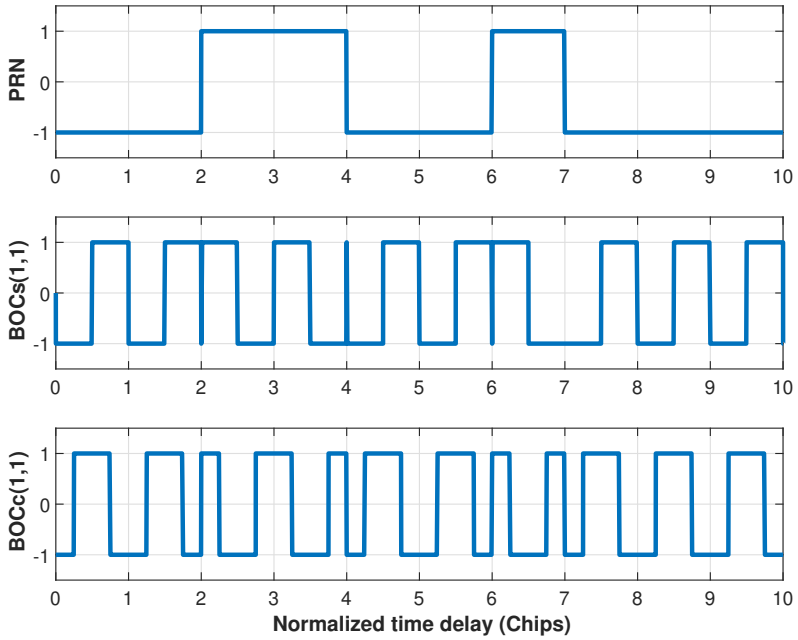

figure 2.6: Spreading code waveform with BOCs(1,1) and BOCc(1,1) subcarrier modulation using PRN code.

As discussed earlier, BOC$s(1, 1)$ and BOC$c(1, 1)$ are two signals obtained by modulating a spreading code with sine and cosine subcarriers. A typical time-domain envelope of these signals is shown in Figure 2.6. The approach taken here is to study the spectral characteristics of BOC modulation first, then proceed to the properties of correlation and the issues of ambiguity, as these factors have a substantial impact on GNSS detection performance [20–22].

2.3.2.1 ACF of BOC signal

The ACF for the BOC-modulated signal is normalized and referred to as the autocorrelation of the signals with count index n. It can be expressed mathematically as in Equation 2.17 [21, 70]. Where, $j \in \{1, \ldots, M+1\}$ and $j \equiv \lceil \frac{\tau}{T_{sc}} \rceil$; here $\lceil \cdot \rceil$ represents the ceiling operator and the parameter τ denotes the variable delay of the locally generated code.

$$R_{BOC}(\tau) = \begin{cases} (-1)^{j-1} \left[\frac{j+(M-j)(2j-1)}{M} + \frac{-1-2(M-j)}{M} \frac{\tau}{T_{sc}} \right], & 0 \leq \tau \leq T_X \\ (-1)^{j} \left[\frac{(M+j-1)(1-2j)+(1-j)}{M} + \frac{2(M+j-1)+1}{M} \frac{\tau}{T_{sc}} \right], & -T_X \leq \tau \leq 0 \\ 0, & \text{otherwise} \end{cases} \tag{2.17}$$

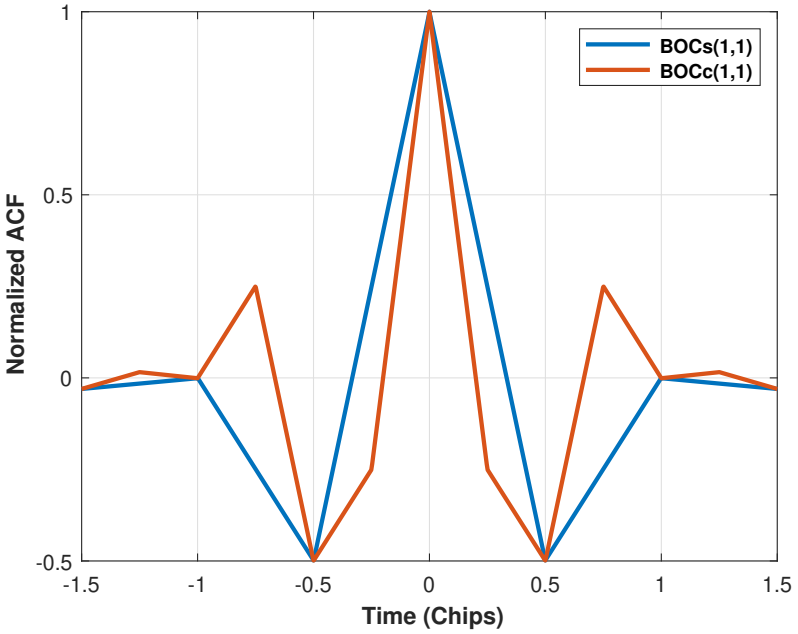

figure 2.7: Normalized ACF of BOCs(1,1) and BOCc(1,1).

As shown in Figure 2.7, which presents the normalized ACFs of BOC signals with parameters $m = 1$, $n = 1$ for BOC, and a chip rate equal to the fundamental rate for BPSK, the BOC modulated signal has a noticeably greater primary peak compared to that of the BPSK modulated signal. A critical observation from our ACF is that the BOC-modulated signals have additional side peaks around the central peak, which increase in number with the enhancement of the modulation order M. Although these side peaks enhance resolution to some extent, they also introduce ambiguities in code tracking. Such ambiguities must be accounted for in GNSS receiver design to prevent erroneous locking and ensure that the receiver can handle weak signals while maintaining stable and reliable tracking [19].

2.3.2.2 PSD of BOC signal

The power spectrum densities (PSDs) of the sine-phase and cosine-phase BOC(m,n) signals, which are denoted as $S_s(f)$ and $S_c(f)$ respectively, can be expressed by [19]:

$$S_\eta(f) \;=\; f_X\left[\frac{A_\eta\,\sin\!\big(u\big)\,\sin^{B_\eta}\!\big(\alpha_\eta\,v\big)}{\pi\,f\,cos(v)}\right]^2 \qquad \forall\, M \tag{2.18}$$

In this unified expression, $\eta = \{s, c\}$ distinguishes between sine-phased (s) and cosine-phased (c) subcarriers. The parameters $\{A_\eta, B_\eta, \alpha_\eta\}$ are defined as $\{1, 1, 1\}$ for $\eta = s$ and $\{2, 2, 0.5\}$ for $\eta = c$. Furthermore, $u = \pi f / f_X$ and $v = \pi f / 2\, f_{sc}$.

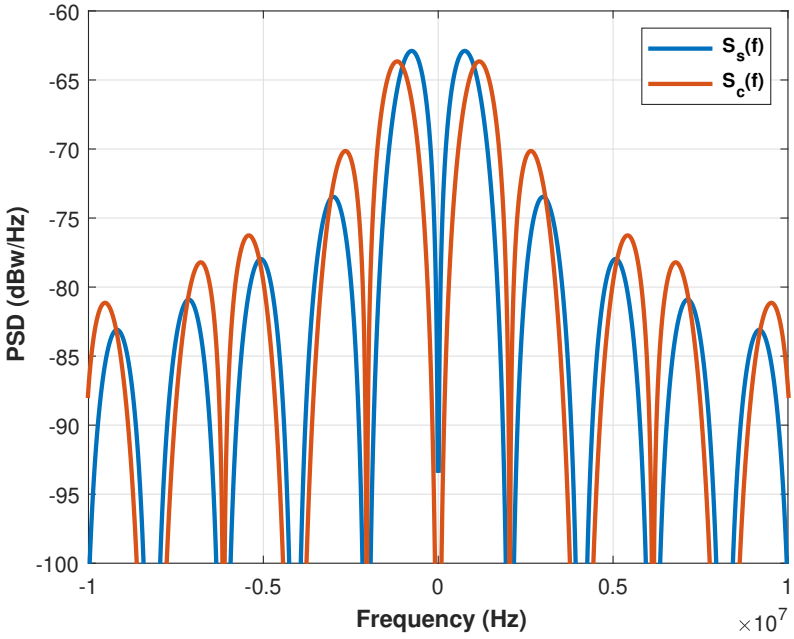

figure 2.8: Normalized PSDs of BOCs/c(1,1) signals.

Figure 2.8 shows the PSDs of BOC$s(1,1)$ and BOC$c(1,1)$. BOC-modulated signals exhibit split power symmetry about the center frequency with energy distributed both above and below the carrier. These signals exhibit a pronounced spectral notch at the carrier frequency, and the resultant band-splitting significantly enhances spectral buoyancy, allowing for coexistence with other signals and reducing the chance of co-channel interference.

2.3.3 MBOC Modulation

The MBOC modulation is marked explicitly as MBOC(6,1,1/11). Here (6,1) shows BOC(6,1) modulated signal inclusion, while 1/11 expresses the ratio of power shared between the BOC(1,1) and BOC(6,1) [22–24]. The BOC(6,1) subcarrier is explicitly used

to enhance the upper-frequency portions more than what a plain BOC(1,1) modulation would do. This produces a very narrow ACF, which improves performance in the presence of noise and MP interference. Concerning MBOC, two major implementation approaches have been developed: CBOC, which was implemented as a waveform for the Galileo OS, and TMBOC, which was applied to the GPS L1C civil signal [22–24].

2.3.3.1 CBOC Iimplementation

CBOC modulation is the European realization of MBOC. This method utilizes a four-level subcarrier, as illustrated in Figure 2.9, with a split power allocation of 50% for data and 50% for pilot. In this case, the CBOC symbols are constructed from the summation of two components: $\sqrt{\frac{10}{11}}X_{BOC(1,1)}(t)$ and $\sqrt{\frac{1}{11}}X_{BOC(6,1)}(t)$ [23].

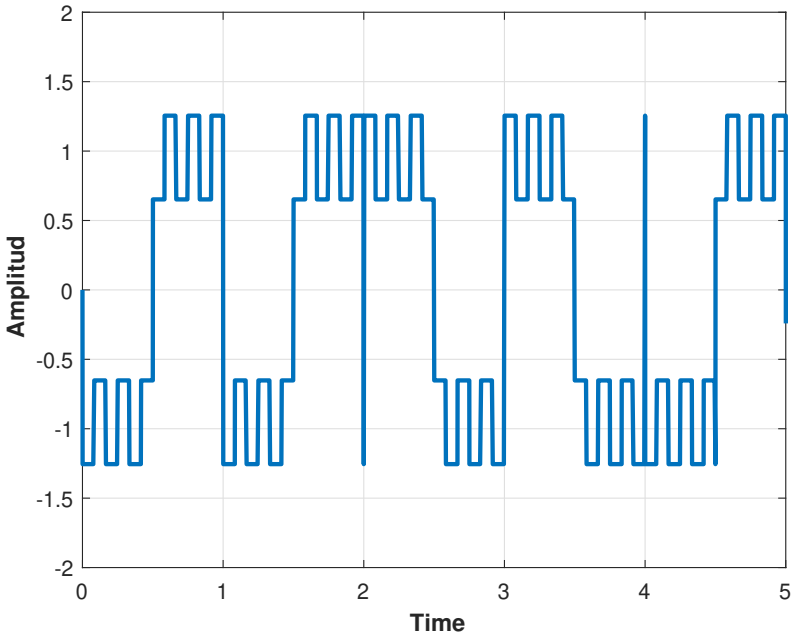

figure 2.9: CBOC subcarrier waveform.

The subcarriers $X_{BOC(1,1)}(t)$ and $X_{BOC(6,1)}(t)$ are given by [23, 24]:

$$X_{BOC(1,1)}(t) = \begin{cases} \text{sign}\left[\sin\left(\frac{2\pi t}{T_c}\right)\right], & 0 \le t \le T_c \\ 0 & \text{elsewhere} \end{cases} \tag{2.19}$$

$$X_{BOC(6,1)}(t) = \begin{cases} \text{sign}\left[\sin\left(\frac{12\pi t}{T_c}\right)\right], & 0 \le t \le T_c \\ 0 & \text{elsewhere} \end{cases} \tag{2.20}$$

The temporal CBOC signal, $X(t)$, is given by [22, 24]:

$$X_{CBOC}(t) = \sqrt{\frac{10}{11}} X_{BOC(1,1)}(t) + \sqrt{\frac{1}{11}} X_{BOC(6,1)}(t) \tag{2.21}$$

The CBOC implementation is specifically denoted as CBOC(6, 1, 1/11). Its total PSD, $S_{CBOC}(f)$, is given by [22, 71]:

$$S_{CBOC}(f) = \frac{1}{2} S_{pilot}(f) + \frac{1}{2} S_{data}(f) = \frac{10}{11} S_{BOC(1,1)}(f) + \frac{1}{11} S_{BOC(6,1)}(f) \tag{2.22}$$

Here, $S_{BOC(1,1)}(f)$ and $S_{BOC(6,1)}(f)$ represent the PSDs of the BOC(1,1) and BOC(6,1), respectively.

2.3.3.2 TMBOC Implementation

TMBOC is the American instantiation of MBOC for the modernized GPS L1C signal. It adopts the partial temporal multiplexing of BOC(1,1) and BOC(6,1) subcarriers according to some predetermined scheme [72]. The TMBOC signal $X_{TMBOC(6,1,p)}(t)$ is expressed by:

$$X_{TMBOC(6,1,p)}(t) = \begin{cases} X_{BOC(1,1)}(t) & \text{if } t \in X_1 \\ X_{BOC(6,1)}(t) & \text{if } t \in X_2 \end{cases} \tag{2.23}$$

In Equation 2.23, X_1 and X_2 are the respective time intervals where BOC(1,1) and BOC(6,1) subcarriers are active.

As described in [73], the TMBOC signal is a binary signal with an accompanying wide-band data channel consisting solely of BOC(1,1) symbols. Additionally, the pilot channel accounts for 75% of the total power, while the data channel comprises the remaining 25%. For the TMBOC architecture, the power allocation is 29/33 for BOC(1,1) and 4/33 for BOC(6,1). Figure 2.10 shows the subcarrier for the TMBOC(6,1,4/33) implementation, where BOC(6,1) chips are added at positions 1, 5, 7, and 30 of every 33 symbol period.

The equations below provide the PSDs of the pilot and data components :

$$S_{pilot}(f) = \frac{29}{33} S_{BOC(1,1)}(f) + \frac{4}{33} S_{BOC(6,1)}(f) \tag{2.24}$$

$$S_{data}(f) = S_{BOC(1,1)}(f) \tag{2.25}$$

$$S_{MBOC(6,1,1/11)}(f) = \frac{3}{4} S_{pilot}(f) + \frac{1}{4} S_{data}(f) \tag{2.26}$$

$$S_{MBOC(6,1,1/11)}(f) = \frac{10}{11} S_{BOC(1,1)}(f) + \frac{1}{11} S_{BOC(6,1)}(f) \tag{2.27}$$

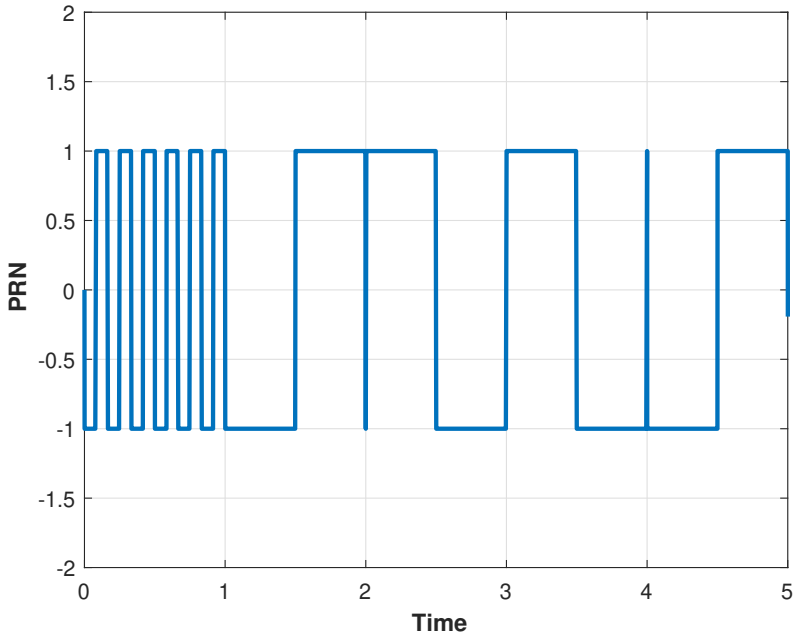

figure 2.10: TMBOC subcarrier waveform.

For a TMBOC implementation assuming a 50%/50% power split between the pilot and data channels, spreading symbols of the BOC(1,1) signal are used on the data channel, and 2/11 of the spreading symbols of the BOC(6,1) signal are used on the pilot channel [24]. In this scenario, the PSDs of the component data and pilot signals are given by:

$$S_{Pilot}(f) = \frac{2}{11}S_{BOC(1,1)}(f) + \frac{9}{11}S_{BOC(6,1)}(f) \tag{2.28}$$

$$S_{data}(f) = S_{BOC(1,1)}(f) \tag{2.29}$$

$$S_{MBOC(6,1,1/11)}(f) = \frac{1}{2}S_{pilot}(f) + \frac{1}{2}S_{data}(f) \tag{2.30}$$

$$S_{MBOC(6,1,1/11)}(f) = \frac{10}{11}S_{BOC(1,1)}(f) + \frac{1}{11}S_{BOC(6,1)}(f) \tag{2.31}$$

In another scenario with the same 50%/50% power split, the pilot channel receives 10/11 of the BOC(1,1) spreading symbols. At the same time, the remainder is allocated to the data channel. Describes the PSDs of the component data and pilot signals for this configuration [23, 24]:

$$S_{pilot}(f) = \frac{10}{11}S_{BOC(1,1)}(f) + \frac{1}{11}S_{BOC(6,1)}(f) \tag{2.32}$$

$$S_{data}(f) = \frac{10}{11}S_{BOC(1,1)}(f) + \frac{1}{11}S_{BOC(6,1)}(f) \tag{2.33}$$

$$S_{MBOC(6,1,1/11)}(f) = \frac{1}{2}S_{pilot}(f) + \frac{1}{2}S_{data}(f) \tag{2.34}$$

$$S_{MBOC(6,1,1/11)}(f) = \frac{10}{11} S_{BOC(1,1)}(f) + \frac{1}{11} S_{BOC(6,1)}(f) \tag{2.35}$$

Table 2.1 summarizes the possible implementations of MBOC (TMBOC and CBOC) for the MBOC(6,1,1/11) modulation [74].

table 2.1: Possible Implementations of MBOC(6,1,1/11) Modulation

Data	Pilot	Pilot Percentage
BOC(1,1)	TMBOC (6, 1 /2)	50%
BOC(1,1)	TMBOC (6, 1 /4)	75%
TMBOC(6, 1 /11)	TMBOC (6, 1 /11)	75%
TMBOC(6, 1 /11)	TMBOC (6, 1 /11)	50%
BOC(1,1)	CBOC(6, 1 /2)	50%
BOC(1,1)	CBOC(6, 1 /4)	75%
CBOC(6, 1 /11)	CBOC(6, 1 /11)	50%
CBOC(6, 1 /11)	CBOC(6, 1 /11)	75%

2.3.3.3 ACF of CBOC and TMBOC signals

For the assessment of the tracking properties of an MBOC-modulated signal, it is critical to compute its ACF. The ACF for the CBOC signal is given by [72]:

$$R_{CBOC}(\tau) = (1 - Q)R_i(\tau) + QR_j(\tau) \tag{2.36}$$

Where:

- $Q = \frac{1}{11}$
- $R_i(\tau)$ and $R_j(\tau)$ represent the ACFs of the BOC(1,1) and BOC(6,1) signals, respectively.

The ACF of the TMBOC signal is defined as follows [75]:

$$R_{TMBOC}(\tau) = (1 - P)R_x(\tau) + PR_y(\tau) \tag{45}$$

Where $P = \frac{4}{33}$.

Normalized ACFs for BOC(1,1), CBOC(6,1,1/11), and TMBOC(6,1,4/33) are shown in Figure 2.11. It can be seen from this figure that the peak ACFs for CBOC(6,1,1/11) and TMBOC(6,1,4/33) modulated signals are narrower than that of the BOC(1,1) signal. This narrowness indicates that MBOC signals are more robust in the presence of noise and MP interference [24, 76]. Also, the zero-crossing points of these ACFs are almost identical and occur around ±0.5 chip intervals.

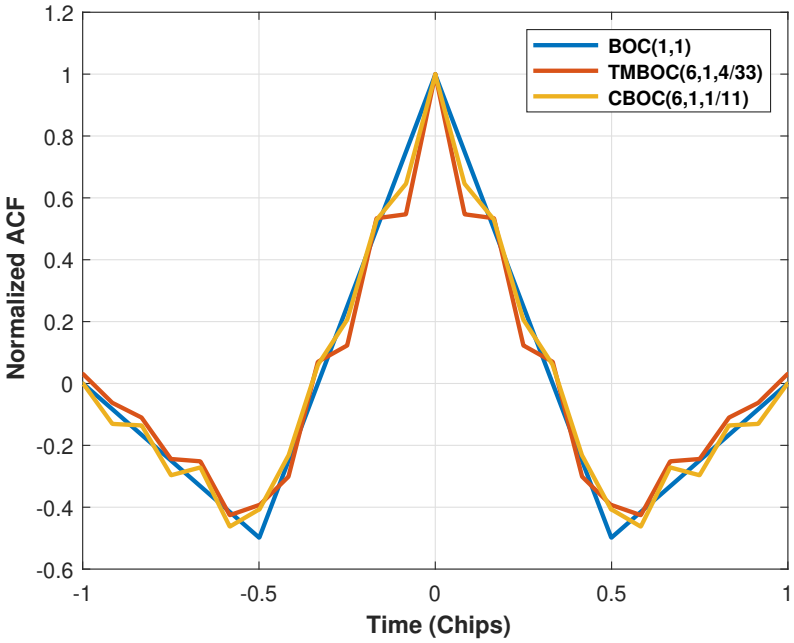

figure 2.11: ACFs of BOC(1,1), CBOC(6,1,1/11) and TMBOC(6,1,4/33) signals.

2.3.3.4 PSD of MBOC Signal

As mentioned earlier, the primary concept of MBOC modulation is to enhance code-tracking performance by reallocating a portion of the signal power to higher frequencies. The power spectral density (PSD) for the MBOC(6,1,1/11) signal is made up of the PSDs of both BOC(1,1) and BOC(6,1) signals. The expression for the PSD of MBOC modulated signals is defined in [24, 76]:

$$S_{MBOC}(f) = \frac{10}{11} S_{BOC(1,1)}(f) + \frac{1}{11} S_{BOC(6,1)}(f) \tag{2.37}$$

Where:

- $S_{BOC(1,1)}(f)$ is the PSD of the BOC(1,1) modulated signal.
- $S_{BOC(6,1)}(f)$ is the PSD of the BOC(6,1) modulated signal.

As shown in Figure 2.12, the MBOC(6,1,1/11) signal's PSD is compared with the BOC(1,1) signal's PSD. From this figure, it can be seen that there is a significant increase in power within the ±6 MHz range when compared to the PSD of the BOC(1,1) modulated signal. This feature is due to the influence of the BOC(6,1) portion contained in the MBOC-modulated signal.

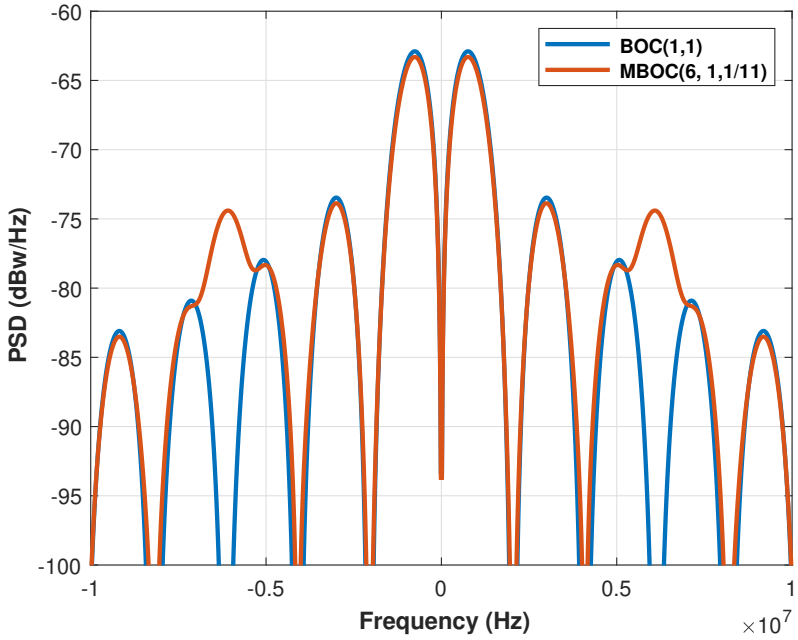

figure 2.12: Normalized PSDs of MBOC(6,1,1/11), BOC(1,1), and BOC(6,1) codes.

2.3.4 BSC Modulation

Typically, BSC modulation refers to the modulation of the PRN code with different binary-coded symbols on a chip-by-chip basis [25]. The BSC signals are divided into subsets where each subset is a segment of length T_c/n, binary-valued over n sub-chips. The spreading symbol of a BSC signal is divided into n sub-chips, which are binary-valued and have a length of T_c/n each. In the context of GNSS, the notation BSC(s, f_c) is used where s is the BSC sequence in a chip [25]. This modulation can be viewed as an extension of BPSK and BOC modulations [25, 77]. For example, BPSK modulation is equivalent to BSC$([1], f_c)$, and BOC$(1,1)$ is equal to BSC$([+1, -1], f_c)$ where the integer '1' denotes chip frequency equals the fundamental frequency $f_0 = 1.023$ MHz. The baseband representation of a BSC signal is given in [25]:

$$X_{BSC}(t) = \sum_{i=-\infty}^{+\infty} \sum_{m=0}^{n-1} c_i s_m U_{T_c/n}(t - mT_c/n - kT_c) \tag{1}$$

Where:

- c_i: Represents the PRN code sequence.
- s_m: Denotes the sequence with values $\{-1, +1\}$.
- $U_{T_c/n}$: Is a rectangular pulse of amplitude 1 and duration T_c/n.

Furthermore, the PSD of BSC($[s], f_c$) signals is given by [78]:

$$S_{BSC([s],1)}(f) = S(f)\left\{n + 2\sum_{i=1}^{n-1}\sum_{j=i+1}^{n-1} s_i s_j \cos\left[(j-i)\frac{2\pi f}{n f_c}\right]\right\} \tag{2.38}$$

2.3.4.1 CBSC Modulation

To improve performance while maintaining interoperability with BOC (1,1) modulation, a specific BSC-based modulation approach, dubbed Composite Binary Coded Symbols (CBCS), has been proposed [25]. This proposal stems from the superposition of a BSC($[1,-1,-1,-1,-1,1,1,1,1],1$) signal and a BOC$(1,1)$ signal, utilizing an adapted Interplex diagram [79]. The CBCS was developed by the Radionavigation Working Group of the European Commission to provide a universal modulation scheme for transmitting Galileo and second-generation GPS codes on the L1 frequency. This approach also enables high interoperability with BOC(1,1) modulation. In general terms, CBCS modulation can be represented as CBCS($[s], f_c, \%$) where f_c is the chip frequency and '%' denotes power given as a percentage. At the same time, '$[s]$' references the BSC sequence vector. The parameters q and p are coefficients indicating power distribution, whereby $q^2 + p^2 = 1$. To stay close to a BOC(1,1) base signal, the amplitude q of the second BSC component is less than the amplitude p of the BOC(1,1) component. The equation for CBCS($[s], f_c, \%$) follows from [25]:

$$X_{CBCS([s],f_c,\%)}(t) = qX_{BOC(1,1)}(t) + pX_{BSC([s],1)}(t) \tag{6}$$

The version of CBCS modulation commonly utilized is denoted as CBCS([1, -1, -1, -1, -1, 1, 1, 1, 1], 20%) or simply CBCS(20%). Here, {1, -1, -1, -1, -1, 1, 1, 1, 1} is the vector $[s]$ corresponding to the BSC sequence. The '1' before '20%' signifies the case where $f_c/f_s = 1$. According to this representation, MBOC(6,1,1/11) modulation is a specific instance of CBCS modulation, equivalent to CBCS($[1,-1,-1,-1,-1,1,1,1,1],1,1/11$) [25, 79].

2.3.4.2 ACF and PSD of CBCS Signal

Figures 2.13 and 2.14 show the ACF and PSD of the CBCS signal. We can conclude that the ACF of CBCS is indeed narrow, accompanied by small secondary peaks. As for the CBCS PSD, it contains two principal lobes with greater power distribution at the higher frequencies.

One of the most important benefits of the CBCS signal is its remarkable adaptability; it can be transformed into other (better) CBCS versions with changes in the BCS

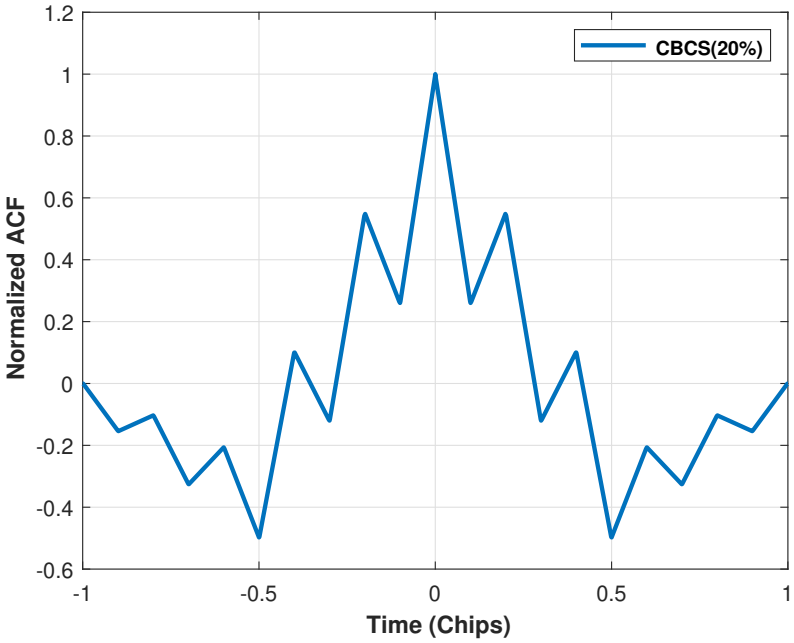

figure 2.13: Normalized ACF of CBCS (20%).

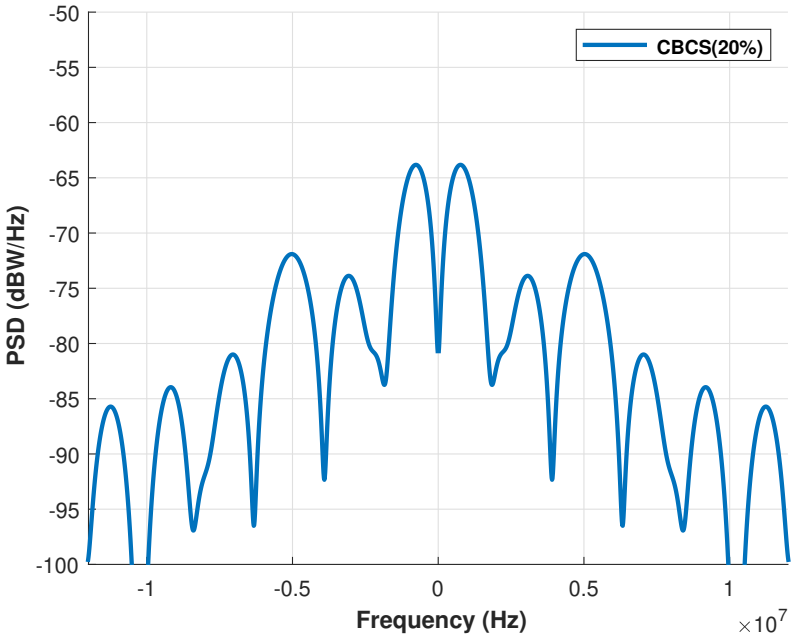

figure 2.14: Normalized PSD of CBCS (20%).

component's contribution or even with different chip rates [25].

2.3.5 GNSS Signals Comparison

Comparing GNSS signals is crucial for selecting the most suitable signal for various GNSS applications. For example, Figure 2.15 illustrates the following comparisons of the nor-

malized ACFs: BPSK, BOC(1,1), TMBOC(6,1,4/33), CBOC(6,1,1/11), and CBCS (20%) signals.

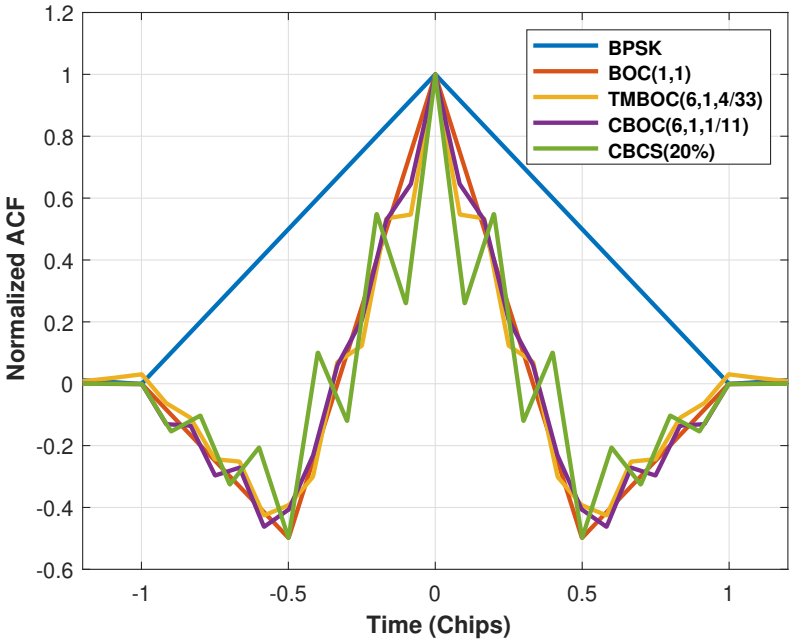

figure 2.15: Normalized ACF of BPSK, BOC(1,1), TMBOC (6,1,4/33) CBOC(6,1,1/11), and CBCS (20%).

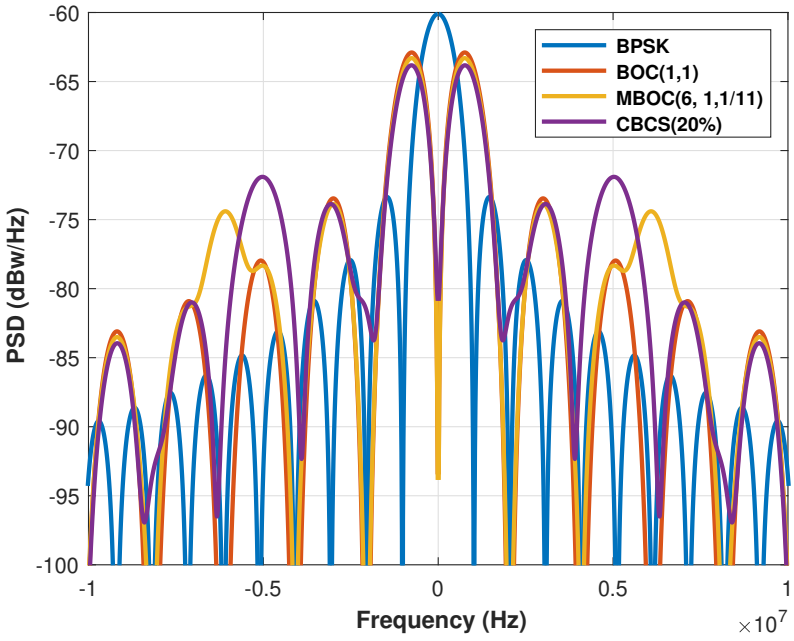

figure 2.16: Normalized PSD of BPSK, BOC(1,1), MBOC(6, 1,1/11) and CBCS (20%).

It is clear from the figure that a broad central peak with no side peaks characterizes the ACF of the BPSK signal. Conversely, the ACFs of the other signals feature a central peak,

which is the strongest, accompanied by several lower-level side peaks. It is remarkable that the CBOC(6,1,1/11), TMBOC(6,1,4/33), and CBCS (20%) signal ACFs exhibit a narrower central peak and lower level secondary peaks when compared to the BOC(1,1) signal's ACF. These advantages result from the greater power shifted toward the higher frequencies.

The PSDs of the BPSK, BOC(1,1), MBOC(6, 1, 1/11) and CBCS (20%) modulated signals are shown in Figure 1.16. From this figure, we can infer that MBOC and CBCS signals demonstrate greater power in their side lobes. This feature is the reason for their greater resistance to noise and MP.

1.4 Time-Hopping Multiple Access in Pseudolites

THMA is utilized in PL systems to enable different users to share a frequency band while mitigating the near/far problem. This problem, observed in PL systems due to the difference and distance-dependent reception characteristics, identifies the dropping signal as being weaker and more challenging to use, as it is subjected to much stronger signals. Each PL is assigned a unique pseudo-random time hop pattern separation, allowing signals from different PLs to be sent in brief, discrete time segments concurrently. Receivers can separate the different PL signals due to the time slots, thereby improving the accuracy and robustness of positioning in challenging environments [6, 8, 13].

1.4.1 THMA Pulsed Pseudolite Signal Structure

The generation of the THMA pulsed PL signal is shown in Figure 1.17, in which the gating pulse $p(t)$ can be formulated as [6]:

$$p(t) = \sum_{k=-\infty}^{+\infty} \left(t - kN_f T_{\mathrm{p}} - a_k^{(V)} T_{\mathrm{p}} \right) \tag{1.39}$$

Here, k marks the current THMA frame index within a complete pattern of K frames. N_f is the number of slots in a single THMA frame and is the inverse of the duty cycle d of the PL signal, where $N_f = 1/d$. T_p denotes the period of one THMA pulse, with $T_p = d \cdot T_c$, and $a_k^{(V)}$ is the pseudo-random THMA slot index. This component is vital as it creates disorder in the sequence of the transmitted pulses [6, 8]. For each frame, $a_k^{(V)}$ is a random integer from the set $\{0, 1, \ldots, N_f - 1\}$. The superscript (V) denotes that this index is from the V-th group of THMA slot indices, which may imply that several PL signals are capable of utilizing different sets of these indices to minimize interference. The pseudo-random choice described ensures that pulses are not sent at regular intervals, thus

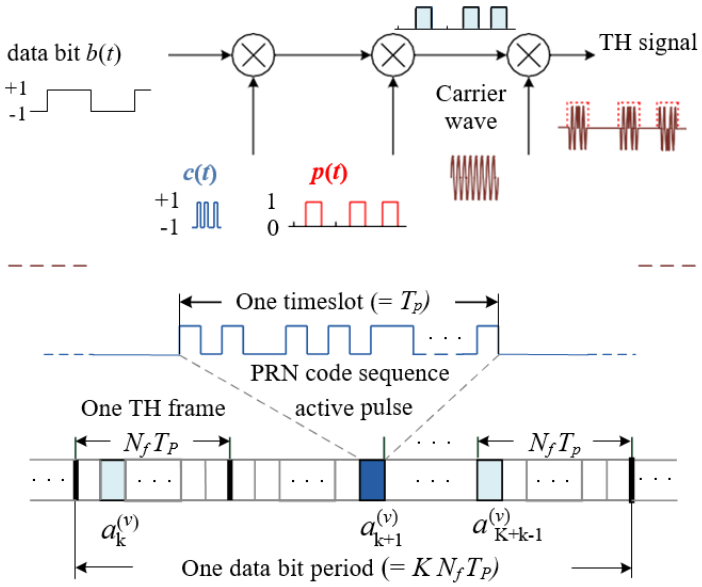

figure 2.17: TH pulsed PL signal generation.

contributing to the spread spectrum properties of the signal and making it more resilient to interference and MP effects [6, 8].

2.4.2 Slot Index Table

The SIT serves as a key component for synthesizing THMA pulsed PL signals. It helps maintain the spectral properties of the GNSS-like signal, ensuring compatibility as well as some degree of signal integrity. Moreover, each PL is issued a separate SIT, which allows receivers to distinguish between different PLs and provides additional support for using existing PRN codes from the base GNSS-like signal [6, 8].

table 2.2: THMA Table

Group ID	TH slot index in different frame				
	0	**1**	**2**	**...**	**K-1**
1	$a_0^{(1)}$	$a_1^{(1)}$	$a_2^{(1)}$	...	$a_{K-1}^{(1)}$
2	$a_0^{(2)}$	$a_1^{(2)}$	$a_2^{(2)}$	...	$a_{K-1}^{(2)}$
⋮	⋮	⋮	⋮	⋱	⋮
V-1	$a_0^{(V-1)}$	$a_1^{(V-1)}$	$a_2^{(V-1)}$	...	$a_{K-1}^{(V-1)}$
V	$a_0^{(V)}$	$a_1^{(V)}$	$a_2^{(V)}$	...	$a_{K-1}^{(V)}$
V+1	$a_0^{(V+1)}$	$a_1^{(V+1)}$	$a_2^{(V+1)}$	...	$a_{K-1}^{(V+1)}$
⋮	⋮	⋮	⋮	⋱	⋮
N	$a_0^{(N)}$	$a_1^{(N)}$	$a_2^{(N)}$	...	$a_{K-1}^{(N)}$

As shown in Table 2.2, the SIT contains several permutation sequences of TH Slot Indices (THSIs). These THSIs serve the purpose of marking the exact time slots where the THMA pulses occur. The pulses serve as gates to the continuous, locally generated GNSS-like signal, which results in the required THMA-pulsed PL signal.

2.5 Slot Index Table Generation

PLs use SITs for THMA signal generation. Older techniques either distribute a single predesigned SIT among several PLs [80] or give distinct SITs to separate LocataLites [81]. A new block-based SIT generation approach [8] that was recently issued is known to construct SITs through the generation of THSI base matrices using congruence codes.

2.5.1 Locata scheme for SIT Generation

The interference alleviation and duplication capabilities of Locata systems are PLs-specific and designed to work in conjunction with Time Division Multiple Access (TDMA) scheduling techniques. Within LocataLites, each millisecond can be divided into 10 time slots, each comprising 900 microseconds, creating a TDMA frame. By collating 200 of these TDMA frames, 200 millisecond intervals are created, which make up "super frames." Curcurent LocataLites within a given time slot are partitioned into geographical sub-networks with a maximum of 10 LocataLites, under the critical constraint that time slots within that sub-network do not overlap [81].

Each LocataLite broadcasts only during its assigned time slot and is mute at all other intervals. To prevent interference to a greater extent, these slot assignments are randomized from one frame to the next. The system defines a maximum of 5 sub-Networks that can be achieved in one time slot, in turn allowing the concurrent operation of up to 50 LocataLites within the same time slot. The design of these schemes aims specifically to reduce overlap and interference between sub-networks, which sometimes requires physical separation due to performance isolation constraints. Table 2.3 provides a partial depiction of a LocataLite subnet 1 ($N_f = 10$) [81].

2.5.2 Generating SIT using Congruence Codes

To generate SITs, this method derives THSI base matrices from specially constructed congruence codes. These base matrices undergo combination, and distinctive rows are chosen to form unique SITs tailored to individual PLs. The foundational idea with this method is a sequential approach to constructing SITs:

table 2.3: SITs generation using Locata scheme Subnet 1

TDMA Frame	**Time slot within frame**									
	1	**2**	**3**	**4**	**5**	**6**	**7**	**8**	**9**	**10**
1	1	9	2	5	10	8	6	4	3	7
2	5	8	4	2	9	7	1	6	10	3
3	10	2	6	1	3	4	5	7	9	8
4	3	2	8	7	4	9	10	1	5	6
5	5	1	2	3	8	10	4	7	6	9
6	3	5	4	8	1	7	2	10	9	6
7	7	10	5	9	4	1	3	6	8	2
8	10	7	8	6	2	3	9	5	1	4
9	6	4	10	3	1	2	7	8	9	5
10	2	1	4	8	5	10	6	3	7	9
⋮	⋮	⋮	⋮	⋮	⋮	⋮	⋮	⋮	⋮	⋮
198	2	1	5	9	7	4	3	10	6	8
199	5	7	2	10	8	6	4	3	1	9
200	3	7	8	1	9	10	4	6	2	5

- **Generation of THSI Base Matrices**: The first step is to generate different THSI base matrices. These matrices are constructed based on specially designed congruence codes. The equation defines the congruence codes:

$$\chi_{\iota,\kappa}^{(\gamma)} \equiv \left(\frac{(\iota+1)(\kappa+1)}{\gamma} - 1 \right) \pmod{\lambda} \tag{2.40}$$

  where:

  - λ is a prime number with $N_f = \lambda - 1$.
  - ι, κ, γ are all integers.
  - $0 \leq \iota, \kappa \leq \lambda - 2$.
  - $1 \leq \gamma \leq \lambda - 1$.

  Through a modular multiplicative inverse operation, it is derived that $\chi_{\iota,\kappa}^{(\gamma)} \in \{0, 1, \ldots, \lambda - 2\}$. Crucially, for fixed parameters γ and ι, varying κ from 0 to $\lambda - 2$ results in a permutation of all elements in the set $\{0, 1, \ldots, \lambda - 2\}$ and has no common elements. This property is essential for generating the THSIs of the PL signal.

- **Combination of THSI Base Matrices**: After generating several distinct THSI base matrices, they are combined. For instance, if N different base matrices are needed, they can be combined into a new matrix, $X_{R_n}^{(\gamma_1,\gamma_2,\ldots,\gamma_N)} = [X_{R_n}^{(\gamma_1)} X_{R_n}^{(\gamma_2)} \cdots X_{R_n}^{(\gamma_N)}]$, where $X_{R_n}^{(\gamma)}$ is a matrix formed by R_n selected rows of $X^{(\gamma)}$.

- **Rows Selection**: From the combined matrix, specific rows are chosen to form a new matrix which will, in turn, serve as the SIT for a particular PL.

- **Generation of Different SITs**: As we have already seen, this approach is advantageous because it is systematic and therefore, easy to modify. It is possible to create different SITs for different PLs by changing the combination of the base matrices (for instance, by changing the values of γ_1 to γ_N). This ensures that all PLs can have distinct SITs, which is crucial for differentiating between different PLs at the receiver.

The method's robust performance relies on carefully constructed congruence codes. A key property is the minimized "hit number" (collisions) of THSIs. Within the same base matrix ($X^{(\gamma)}$), the hit number between two distinct rows ($\chi^{(\gamma)}_{\iota,\kappa}$ and $\chi^{(\gamma)}_{\iota',\kappa'}$), even with a cyclic shift, is at most one. For THSIs from different base matrices ($X^{(\gamma)}$ and $X^{(\gamma')}$), the hit number is at most N_f. These low hit rates directly contribute to favorable correlation properties for the final SITs [8].

2.5.3 Statistical Distribution of THSI

As already mentioned in 2.5.2, the THSI for each row of the base matrix uniquely occupies places from 0 to $N_f - 1$. It can be challenging to characterize the whole distribution of THSI at once; therefore, one approach is to perform simulations of THSI intervals for different SITs and analyze the results. Distributional histograms for SITs based on the congruence codes-based method and the Locata scheme are shown in figures 2.18 and 2.19, respectively.

From these figures, we can derive some critical conclusions. As with the Locata scheme, the average THSI interval for the congruence code-based method is similar in value; however, the congruence code-based method has a greater standard error. This greater variability could be helpful for the detection and tracking of the transmitted PL signals [82]. Moreover, the congruence codes-based method has fewer repetitions of THSI intervals (10) when compared to Locata's, which aids in lessening the occurrence of false spectral lines during PL signal tracking [83]. On the other hand, the Locata scheme has the advantage of zero repetitions for THSI intervals equal to one, which may cause detection ambiguities between adjacent binary-mapped THSIs [8].

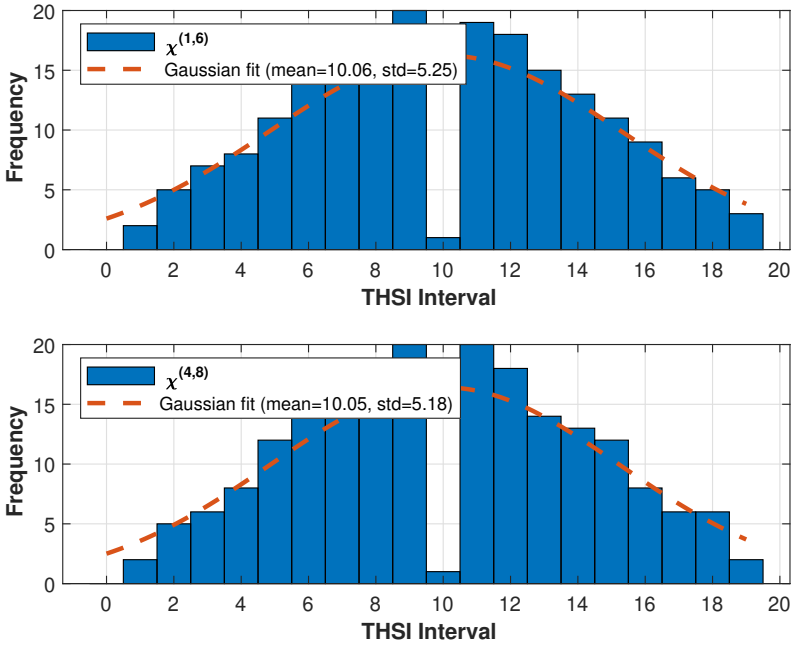

figure 2.18: Distributional Histograms of SITs derived from Congruence Codes.

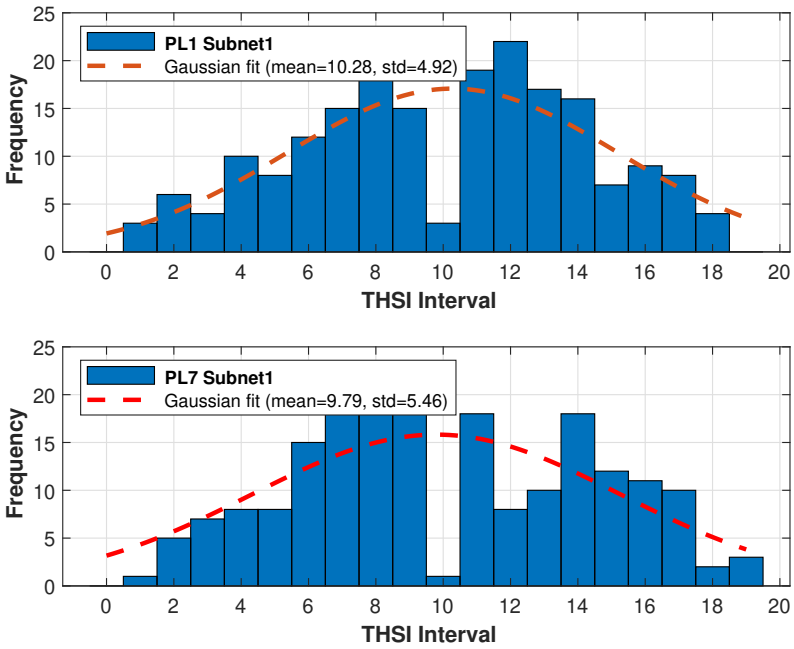

figure 2.19: Distributional Histograms of SITs derived from Locata scheme.

2.6 Conclusion

This chapter provided a detailed examination of signal design principles for both GNSS and PL positioning systems. The discussion initiated with the fundamental components of GNSS signals, establishing the roles of DSSS, PSD, and ACF in defining signal performance. A systematic analysis of prominent modulation schemes was conducted, including

BPSK, BOC, MBOC (with its CBOC and TMBOC implementations), and BSC (including the CBSC variant). This review emphasized a comparative assessment of their distinct ACF and PSD characteristics, which directly influence tracking precision and resistance to interference.

The chapter then addressed the near-far challenge in PL systems by presenting THMA as a robust mitigation technique. The analysis covered the structure of THMA-pulsed signals and delved into methods for generating the SITs essential for their operation. A key focus was the comparison between the established Locata scheme and a modern congruence codes-based approach, evaluating their respective THSI statistical distributions.

The insights into these varied signal architectures underscore the importance of deliberate signal design in modern navigation. This foundational knowledge is essential for evaluating performance enhancements and exploring the practical applications that will be investigated in the subsequent chapters.

Chapter 3

Acquisition, Tracking, and MP Mitigation in GNSS/PL Receivers

3.1 Introduction

This chapter dissects the core signal processing chain within GNSS and PL receivers, moving from the initial search for a signal to the fine-tuned lock required for navigation. We begin with signal acquisition, exploring the fundamental challenge of detecting faint signals by searching across a vast space of potential code delays and Doppler frequencies. The discussion covers classic serial and parallel search methods, as well as techniques such as zero-padding to overcome data bit transitions. Following the acquisition, the focus shifts to signal tracking, where the receiver must maintain a continuous lock on the signal. This section details the operation of the Phase-Locked Loops (PLL) for carrier tracking and the DLL for code tracking.

The chapter then covers PL signal processing, focusing on precise THMA pulse timing, and the overarching challenge of MP interference that degrades receiver performance. A significant portion is therefore dedicated to advanced baseband mitigation techniques, which are essential for robust positioning. This includes a comprehensive overview of sophisticated correlator strategies, covering the foundational NC method and the more complex DD, EDD, and SLG approaches. This survey provides the necessary background to critically analyze the limitations of each method, setting the stage for the novel solution proposed in the following chapter.

1.2 Signal Acquisition

The acquisition phase of the GNSS navigation process is critical because it attempts to detect and acquire the visible satellite signals. It tries to find the two signal parameters: the code delay and the Doppler frequency shift [26]. To obtain the two parameters, a correlation matrix is generated for a synchronized two-dimensional search over time and frequency. This requires a thorough search through all possible combinations of Doppler frequency and code delay to find the peak correlation [5]. Ultimately, the acquisition module successfully identifies the criteria and parameters, marking a successful detection. These parameters will then be utilized in the signal tracking stage, which is performed after the acquisition stage [27].

1.2.1 Serial Search Acquisition

The fundamental structure of the serial search acquisition system is depicted in Figure 1.1. As illustrated, the incoming digital GNSS signal $S_r(t)$, which is given in Equation 1.1, undergoes processing to extract an intermediate frequency. Within the acquisition block, this signal undergoes a multiplication process with a locally produced signal replica. This local signal replica contains at least the primary PRN code $c_1(t)$, the sub-carrier $S_{sc}(t)$, and sometimes the secondary code $c_2(t)$.

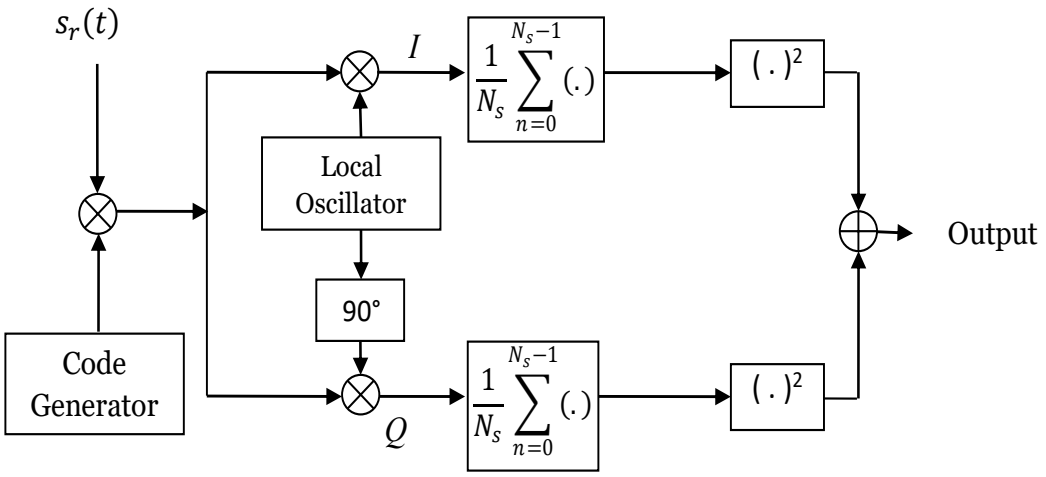

figure 1.1: Block diagram of serial search acquisitions.

The received signal $S_r(t)$ can be expressed as:

$$S_r(t) = A \cdot b(t-\tau) \cdot c(t-\tau) \times \cos(2\pi(f_{IF} + f_{dop})t + \phi_{IF}(t)) + w(t) \tag{3.1}$$

Where:

- A: Instantaneous received signal power;
- $b(t)$: Navigation data;
- $c(t)$: PRN code corresponding to a specific satellite;
- τ: Received signal delay;
- f_{IF}: Intermediate frequency;
- f_{dop}: Doppler shift frequency for a specific satellite;
- ϕ_{IF}: Phase of the received signal's carrier;
- $w(t)$: Additive White Gaussian Noise (AWGN).

The GNSS signal local replica is delayed intentionally by an amount $\hat{\tau}$. This predetermined delay is given by:

$$\hat{\tau} = \hat{\tau}_{min} + h_1 \Delta t \quad \text{for } h_1 = 0, 1, ..., H_1 - 1 \tag{3.2}$$

The hypothesis H_1 tests a range of possible delays, which allows the acquisition unit to determine the delay corresponding to the incoming signal $S_r(t)$. After this step, the signal is split into two branches to form its in-phase (I) and quadrature (Q) components. These components are formed by multiplying the signal with cosine and sine carriers, and then separately deriving the products. This method generates two new signals, as described in [84].

$$S_I(t, \hat{\tau}, \hat{f}_{dop}) = S_r(t) c_1(t - \hat{\tau}) \cos(2\pi \hat{f}_{dop} t) \tag{3.3}$$

$$S_Q(t, \hat{\tau}, \hat{f}_{dop}) = S_r(t) c_1(t - \hat{\tau}) \sin(2\pi \hat{f}_{dop} t) \tag{3.4}$$

Multiplication of the input signal by the two configured sinusoids effectively shifts the signal down to baseband level, thereby mitigating the effects of the Doppler shift. The estimated Doppler frequency, $\hat{f}_{dop}$, is a quantized digital frequency, which means it is normalized for the sampling rate of the Analogue-to-Digital Converter ADC . The normalized frequency $\hat{f}_{dop}$ is given by :

$$\hat{f}_{dop} = (f_{IF} + \hat{f}_{dop})T_e = \frac{f_{IF} + \hat{f}_{dop}}{f_e} \tag{1.5}$$

Where f_{dop} is the local Doppler frequency, selected from a predefined set:

$$\hat{f}_{dop} = \hat{f}_{dop,min} + l_d\Delta f \quad \text{for } l_d = 0, 1, ..., L_d - 1 \tag{1.6}$$

Consequently, L_d distinct Doppler frequencies are evaluated to ascertain the frequency excursion for the incoming signal. For a stationary receiver, it is conventionally assumed that the frequency variation is confined within -10 KHz $\leq f_{dop} \leq 10$ KHz [27, 28].

The in-phase $S_I(t, \hat{\tau}, \hat{f}_{dop})$ and quadrature branch signals $S_Q(t, \hat{\tau}, \hat{f}_{dop})$ are both processed in parallel and sent to a coherent integration (or Integrate and Dump) block. This integration is performed over one or several code periods to provide a correlation value. This form of coherent integration yields greatly improved performance by noise variance reduction. The expressions for the outputs of the correlators for the in-phase and quadrature branches are given by:

$$\hat{S}_I(t, \hat{\tau}, \hat{f}_{dop}) = \frac{1}{N_s}\sum_{n_s=0}^{N_s-1} S_I(t, \hat{\tau}, \hat{f}_{dop}) \tag{1.7}$$

And

$$\hat{S}_Q(t, \hat{\tau}, \hat{f}_{dop}) = \frac{1}{N_s}\sum_{n_s=0}^{N_s-1} S_Q(t, \hat{\tau}, \hat{f}_{dop}) \tag{1.8}$$

In this context, N_s refers to the number of samples taken to compute the in-phase and quadrature components, which helps determine the coherent integration time, T_i. This integration time is SNR dependent; a lower SNR requires a longer integration time. It is most common to set T_i as some integer multiple of the primary PRN code period, where:

$$T_i = N_s T_e \tag{1.9}$$

The last step in the acquisition process is to compute the power by performing a squaring operation followed by the summation of the two integrated in-phase and quadrature components. Therefore the output $S(t, \hat{\tau}, \hat{f}_{dop})$ can be represented as:

$$S(t, \hat{\tau}, \hat{f}_{dop}) = (\hat{S}_I(t, \hat{\tau}, \hat{f}_{dop}))^2 + (\hat{S}_Q(t, \hat{\tau}, \hat{f}_{dop}))^2 \tag{1.10}$$

The quantity $S(t, \hat{\tau}, \hat{f}_{dop})$ defines a function of two variables, the parameters: estimation of the Doppler frequency $\hat{f}_{dop}$ and the code delay $\hat{\tau}$. Typically, the results of this

function are plotted on a two-dimensional grid, commonly referred to as the search space or correlation matrix. Each pair of $(\hat{f}_{dop}, \hat{\tau})$ values is associated with a time/frequency cell in this search space [83] in Figure 3.2, we illustrate the concept of time-frequency code sweeping: a joint search over time (code) and frequency (Doppler). More specifically, for every intermediate frequency $\hat{f}$ within the range of -10 KHz to $+10$ KHz, with a step size of $\Delta f = 500$ Hz, we traverse through 1023 code chips. The objective of the acquisition algorithm is to determine the appropriate cell that provides the maximum correlation value. It is noteworthy that the correlator output will be at peak value (a correlation peak equal to its maximum value) when the locally generated code is aligned with the incoming signal's code and the locally generated frequency is equal to the transmitted signal's frequency.

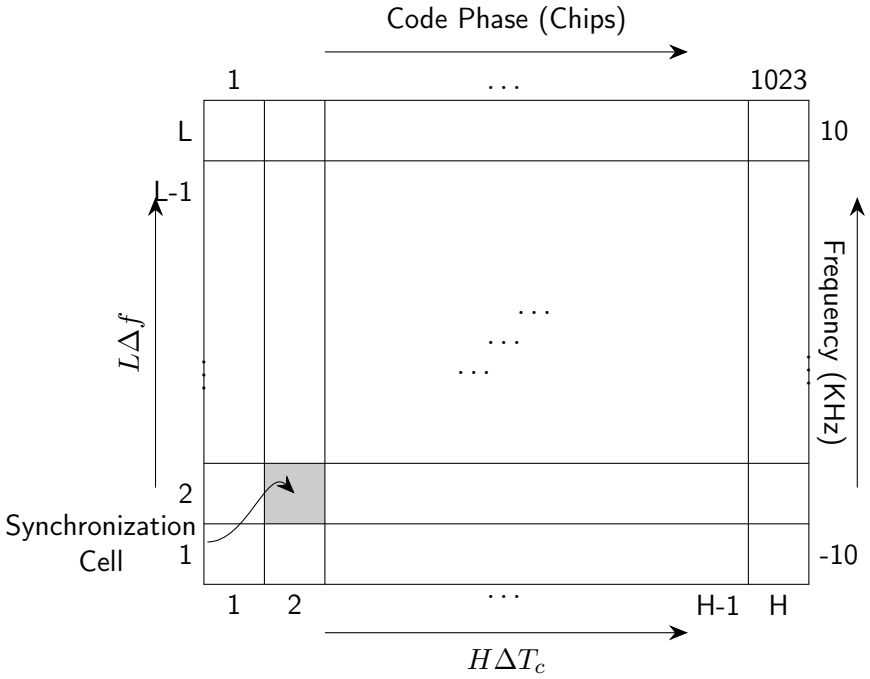

figure 3.2: Frequency and Time offsets.

The surpassing of a certain threshold during the computation of $S(t, \hat{\tau}, \hat{f}_{dop})$ indicates successful acquisition. At this moment, the estimated parameters of $\hat{f}_{dop}$ and $\hat{\tau}$ are accepted as optimal estimates. As a result, the GNSS receiver has locked onto the satellite signal, and a correlation peak is noted which matches the one shown in Figure 3.3.

3.2.2 Parallel Search Acquisition.

Figure 3.4 illustrates the block diagram for the code parallel search acquisition method using the classic FFT method. The received signal $S_r(n)$ is divided into I and Q com-

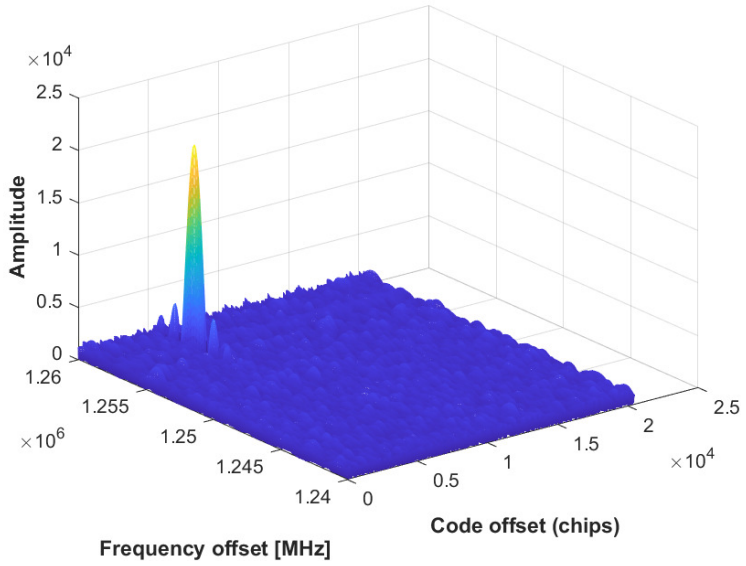

figure 3.3: CA code and navigation data.

ponents. These I and Q parts are then fused to yield the complex signal $I + Q$ [85]. The functional components of the signal, the real part $S_{r,re}(t)$ and the imaginary part $S_{r,im}(t)$, are processed by the FFT block. The outputs for $S_r(t)$'s complex samples are multiplied with the complex conjugate samples of the local code $c_1(n)$'s FFT. The product is an intermediate result that is transformed back into the time domain through Inverse FFT (IFFT). These transformations achieve circular convolution, which results in complete correlation over the integration period. Thus, this technique allows for the parallel computation of all possible code delays within a single operation. [85, 86].

This acquisition system, which utilizes the FFT algorithm for correlation computation, yields better performance than serial search techniques. It also parallelizes the code delay shifting steps for added efficiency. Equation 3.11 depicts how convolution is calculated via FFT/IFFT functions [87].

$$S_r(t) \otimes c_1(t) = \sum_{n_s=0}^{Ns-1} S_r(t) \times c_1(t+\tau) = \mathcal{F}^{-1}[\mathcal{F}(S_r(t)) \times \mathcal{F}(c_1(t))^*] \tag{3.11}$$

Here, $\mathcal{F}$ and $\mathcal{F}^{-1}$ represent the FFT and the IFFT, respectively.

3.2.3 Zero-Padding for Bit Sign Transitions

In a parallel code phase search, the circular correlation operates on a received signal segment equal in length to one full code period. However, this segment is often not

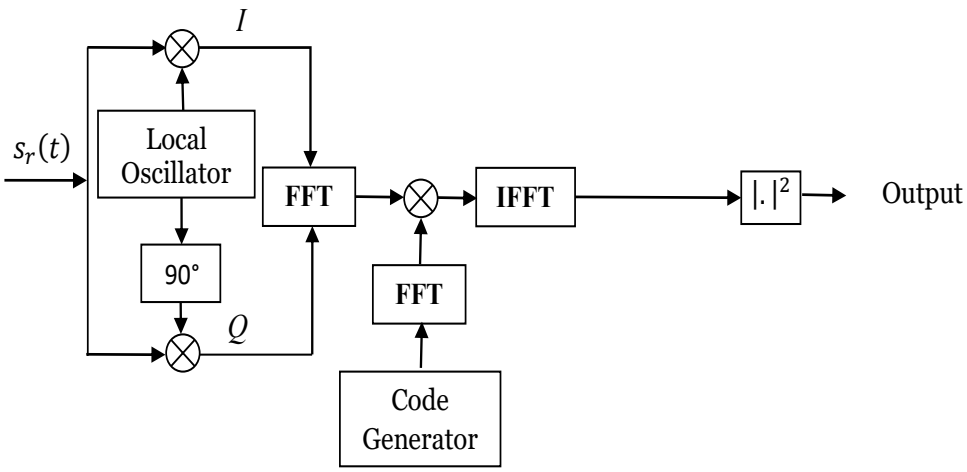

figure 3.4: Block diagram of parallel search acquisition.

perfectly aligned with the underlying code and may span the boundary between two consecutive periods (Figure 3.5). If a data bit or secondary code transition happens at this boundary, part of the signal segment will have an inverted sign, which causes the correlation peak to drop significantly and complicates acquisition [88].

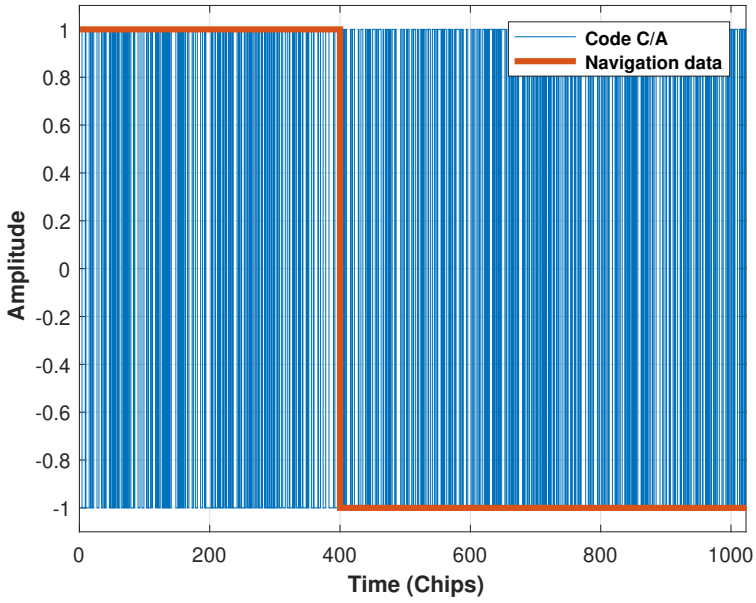

figure 3.5: CA code and navigation data.

In the absence of secondary codes and data, the two codes, when correctly aligned,

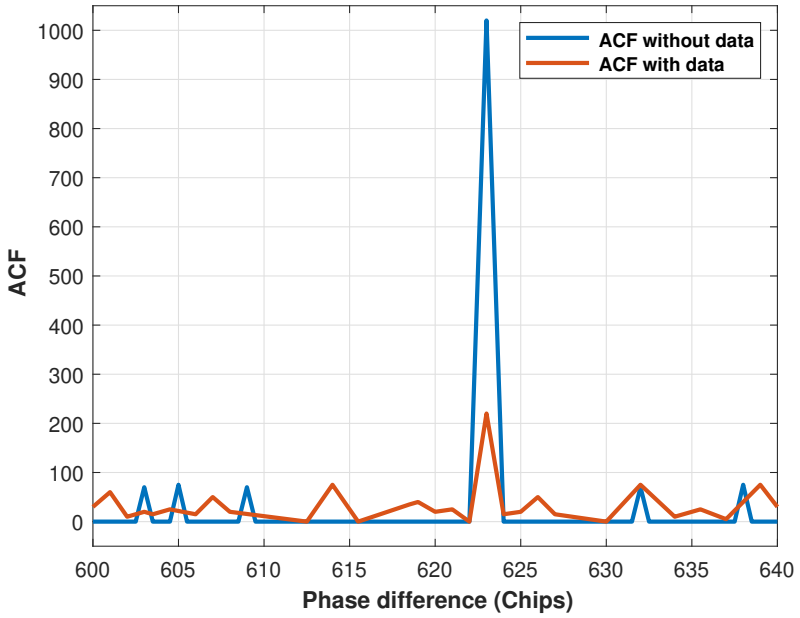

figure 3.6: Correlation with and without data.

can be multiplied to form a composite signal that consists entirely of ones. Hence, from the signal, the sum of ones can be accumulated to result in a sum which is equal to the number of chips. However, in the presence of data, after performing the multiplication of the two codes, some points remain at 1, while the rest switch to -1. This dramatically diminishes the correlation value after accumulation, as shown in Figure 3.6.

One approach to solving the bit sign transition issue is to increase the correlation length while using Zero-Padding [89, 90]. This method executes circular correlation using two consecutive periods of a received code and one zero-padded period of the corresponding code. This guarantees that there is always a complete period of the received code. Thus, the first half of the correlation output is guaranteed to contain a maximum correlation peak, and the second half is susceptible to being affected by the sign transition [89, 90].

The corresponding correlation equations are given by :

$$y[n_z] = \sum_{k_z=0}^{2N_z-1} h_z[k_z]x[(n_z + k_z) \pmod{2N_z}] \quad \text{for } n_z = 0, \ldots, 2N_z - 1 \tag{3.12}$$

$$y = \mathcal{F}^{-1}(\overline{\mathcal{F}(h_z)}\mathcal{F}(x)) \tag{3.13}$$

Where N_z represents the total number of samples within one code period, and $h_z[k_z] = 0$ for $N_z \leq k_z \leq 2N_z - 1$.

Considering that the input code length has been increased to two periods, two peaks will emerge in the circular correlation output. Nonetheless, the peak in the first half of the

circular correlation is always the maximum peak (which suggests significant amplitude), while the peak arising from the second half may be diminished because of the sign shift. Therefore, only the first half of the circular correlation output is retained, while the second half is discarded. It should also be noted that the last sample of "X_z" is now redundant, so the correlation can be calculated for the $2N_z - 1$ points if one prefers [90].

3.3 THMA Pseudolite Signal Acquisition

In PL systems, the acquisition process at the receiver is critical, extending beyond merely generating unique SITs at the transmitter. Practical PL assistance requires robust SIT detection at the receiver, which fundamentally involves searching for the precise THMA pulse positions within the incoming PL signal. These THSIs must exhibit a pseudo-random characteristic to preserve the essential spectral properties of the initial DSSS transmission. This maintains the resolution of the Doppler frequency ambiguities present during the acquisition and tracking stages of the PL signal, which serves to enhance signal lock accuracy [6, 13]. Historically, THMA pulse signal acquisition was done using fixed exhaustive search techniques that tested matched THMA intervals [91]. Although these approaches incorporated techniques such as Maximum Likelihood Estimation (MLE) and Non-coherent Squaring Detection (NSD), these exhaustive approaches tended to break down in low SNR situations with erroneous training intervals, often causing suboptimal acquisition probabilities [91, 92].

As a result, a new acquisition method improves upon previous techniques. This method follows a process composed of three stages (Figure 3.7): first obtaining a mapped code sequence from the ACF peaks indices of the DSSS component; second deriving the corresponding code sequences from different THST groups within the SIT; and third, performing a circular correlation of the derived sequence with the SIT's sequences to locate the maximum correlation peak. This method significantly enhances the acquisition of the TH pulse position relative to traditional techniques, which rely on exhaustive searching [6].

3.3.1 Criticality of Accurate THMA Pulse Time Estimation

Accurately detecting the position of THMA pulses is essential for two main reasons: it provides the time delay information required for ranging, and it is critical for the demodulation needed to mitigate pulse interference. The goal is to determine the time delay, τ_p, of a pseudo-random THMA pulse by comparing its measured position to a predicted one.

As illustrated in Figure 3.8, this total time delay τ_p is composed of an **integral part**

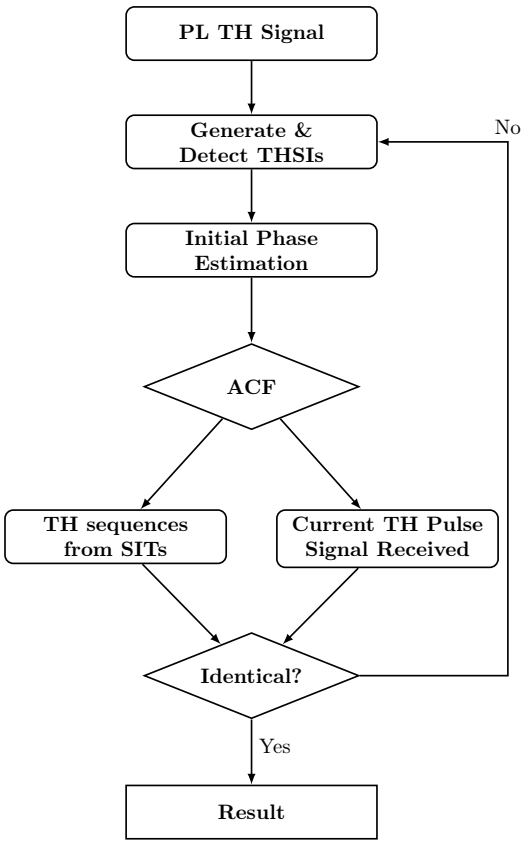

figure 3.7: THMA pulse Detection Flowchart.

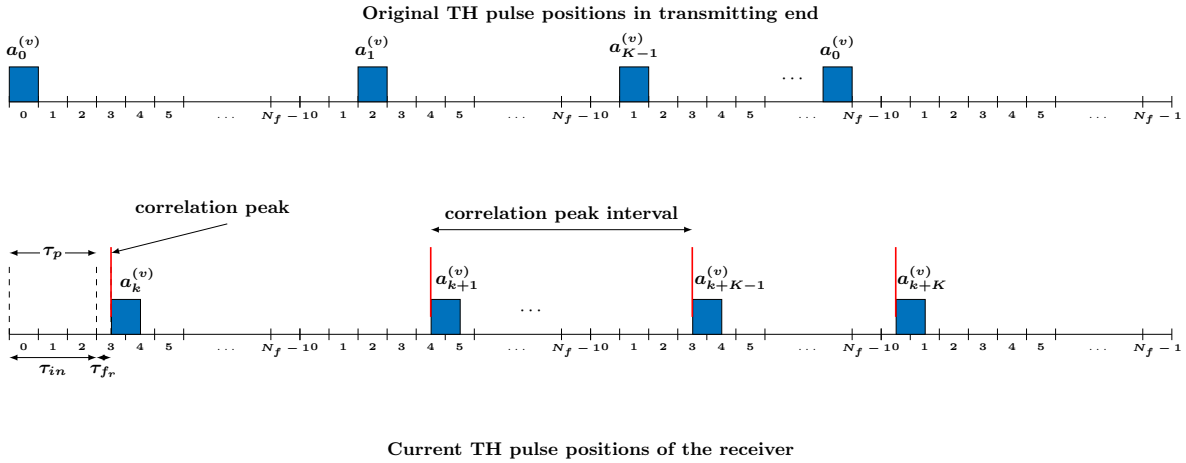

figure 3.8: THMA pulse Time Estimation from the initial phases linked to ACF peaks of the DSSS signal.

(τ_{in}) and a **fractional part** (τ_{fr}), both measured in time slots. The fractional part, τ_{fr}, corresponds to the leading segment of the DSSS component. Its value is unambiguously found from the peak positions of the ACF used to determine the DSSS component.

3.3.2 Initial Phase Acquisition

The generation of ACF peaks necessitates the proper formation of the PRN code; thus, the first step involves acquiring the initial phase of the code. While the Pulsed-PL signal is received intermittently, most methods used to set the initial PRN code phase using satellite GNSS signals apply to PL signals [93].

Considered [94], the parallel PRN code phase search acquisition method gives a basic idea on how to compute the initial PRN code phase for a Pulsed-PL signal:

$$\tau_{fr} = \arg \underset{\hat{\tau}}{} \left(\max_{\hat{\tau}, \hat{f}_{\text{dop}}} \sqrt{I^2 \left(\hat{\tau}, \hat{f}_{dop} \right) + Q^2 \left(\hat{\tau}, \hat{f}_{dop} \right)} \right) \tag{3.14}$$

In this expression, $\hat{\tau}$, $\hat{f}_{dop}$ denote the estimated initial PRN code phase and the estimated Doppler frequency, respectively. The terms $I\left(\hat{\tau}, \hat{f}_{dop}\right)$ and $Q\left(\hat{\tau}, \hat{f}_{dop}\right)$ signify the in-phase and quadrature phase integration outcomes derived from two successive TH frames.

3.3.3 Slot-Level Timing Resolution

Applying Equation 3.3.2, the locally generated baseband signal is defined as $s_L(\tau_{fr}) = \sum_{m_c=0}^{M_c-1} cu_{T_c}(t - m_c T_c - \tau_{fr})$. The local signal $s_L(\tau_{fr})$ can be correlated with the received pulsed-PL signal within each segment, and the ACF peaks associated with the underlying PRN code sequence can be tracked alongside their exact timestamps (Figure 3.8) [6]. The binary sequence generated from the intervals containing the ACF peak values is generally employed to identify the SIT of the PL signal. Let us assume that $\mathcal{N}_{pk}$ ACF peaks are detected. Their corresponding positions are $\left\{\vartheta_{k_p}, k_p = 0, 1, \cdots, \mathcal{N}_{pk} - 1\right\}$, then the THMA pulse intervals of the PL signal can be determined in units of T_{p} as [6]:

$$\Gamma_{k_p-1,k_p} = \left\lfloor \frac{\vartheta_{k_p} - \vartheta_{k_p-1}}{T_{\text{p}} f_{samp}} \right\rfloor, \quad k_p = 1, 2, \ldots, \mathcal{N}_{pk} - 1 \tag{3.15}$$

where f_{samp} is the sampling frequency.

The set of THMA pulse intervals can be represented as $\left\{\Gamma_{k_p-1,k_p} \mid k_p = 1, 2, \cdots, \mathcal{N}_{pk} - 1\right\}$. From these intervals, a corresponding binary code sequence, $\mathbf{Q}$, can be generated, defined as $\mathbf{Q} = \{q(i) \mid i = 0, 1, \cdots, \sum_{k_p=1}^{\mathcal{N}_{pk}-1}\}$, where the specific value of $q(i)$ is determined by:

$$q(i) = \begin{cases} 1, & i = \sum_{k=1}^{J} \Gamma_{k_p-1,k_p}, J = 0, 1, 2, \cdots, \mathcal{N}_{pk} - 1 \\ 0, & \text{others.} \end{cases} \tag{3.16}$$

Following a similar methodology to how the binary code sequence is derived from auto-

correlation peak intervals, each SIT stored within the receiver can also be transformed into a unique binary code sequence. Specifically, for the $\mathcal{V}$-th SIT out of a total of $\mathcal{N}$ stored results, the corresponding binary code sequence, $\mathbf{P}^{(\mathcal{V})}$, can be expressed as $\mathbf{P}^{(\mathcal{V})} = \left\{p^{(\mathcal{V})}(i) \mid i = 0, 1, \cdots, 2KN_{\mathrm{f}} - 1\right\}$, where $\mathcal{V}$ ranges from 1 to $\mathcal{N}$, and $p^{(\mathcal{V})}(i)$ is defined as:

$$p^{(\mathcal{V})}(i) = \begin{cases} 1, & i = a_j^{(\mathcal{V})}, j = 0, 1, \cdots, 2KN_{\mathrm{f}} - 1 \\ 0, & \text{others} \end{cases} \tag{3.17}$$

where $a_j^{(\mathcal{V})}$ is the THSI of the $\mathcal{V}$-th SIT.

Having generated the binary code sequences for the ACF peak intervals and the $\mathcal{N}$ stored SITs, identification of pulse positions for the transmitted Pulsed-PL signal is now straightforward. As described in the methodology, this is done through circular correlation. The iterative procedure follows:

$$d_t^{(\hat{\mathcal{V}})} = \underset{i,\mathcal{V}}{\arg} \left(\max_{\substack{i=0,1,\cdots,\mathcal{L}-1; \\ \mathcal{V}=1,2,\cdots,\mathcal{N}}} \left(\overline{\mathbf{Q}}(i) \otimes \tilde{\mathbf{P}}^{(\mathcal{V})}(i) \right) \right) \tag{3.18}$$

In this notation, $\hat{\mathcal{V}}$ denotes the estimated value of $\mathcal{V}$, representing the identified subgroup ID within the list corresponding to the slot indices in the THMA table. The expressions $\overline{\mathbf{Q}}(i)$ and $\tilde{\mathbf{P}}^{(\mathcal{V})}(i)$ indicate the sequences $\overline{\mathbf{Q}}$ and $\tilde{\mathbf{P}}^{(\mathcal{V})}$ circularly shifted by i positions, with each sequence having length $\mathcal{L}$. The operators "$\otimes$" and "max" represent circular correlation and the maximum selection, respectively.

To streamline the system's processing, $d_t^{(\hat{\mathcal{V}})}$ can be calculated using a more efficient method that applies FFT algorithms. The methodology for this case is described as:

$$d_t^{(\hat{\mathcal{V}})} = \underset{i',\mathcal{V}}{\arg} \left(\max_{\substack{i'=0,1,\ldots,\mathcal{L}-1; \\ \mathcal{V}=1,2,\ldots,\mathcal{N}}} \left| \mathcal{F}^{-1^{(i')}} \left\{ \mathcal{F}(\overline{\mathbf{Q}}) \cdot \left[\mathcal{F}\left(\tilde{P}^{(\mathcal{V})} \right)^* \right] \right\} \right| \right) \tag{3.19}$$

3.4 Signals Trucking

In the previous discussion, the acquisition phase has offered only rough estimates of the carrier frequency and the code delay. To complete the signal demodulation, one must proceed to the code tracking phase [15, 27]. In this phase, the system continuously attempts to achieve better precision on both the carrier frequency and the alignment of the received and locally generated codes by refining the set of Doppler shifts and the code delay.

The PLL handles the estimation of the carrier frequency, while the DLL estimates the code delay [54]. Note that any locally generated code and received code pair that are out of phase will result in insufficient signal energy for a reliable detection in the data demodulator at the receiver end, causing the signal energy to drop below the threshold [84].

3.4.1 Phase-Locked Loop

The PLL is crucial for coherent communication receivers, which track the frequency of the modulated signal carrier. For perfect demodulation, the carrier frequency and the phase are ideally available [54]. However, there might be noise, or the satellite or the receiver might be moving, which factors into the received carrier frequency having a slight offset. This offset can be considered a time-varying phase, provided it is small relative to the carrier frequency and the PLL feedback system can effectively track it. This facilitates carrier and phase lock with sufficient precision [95].

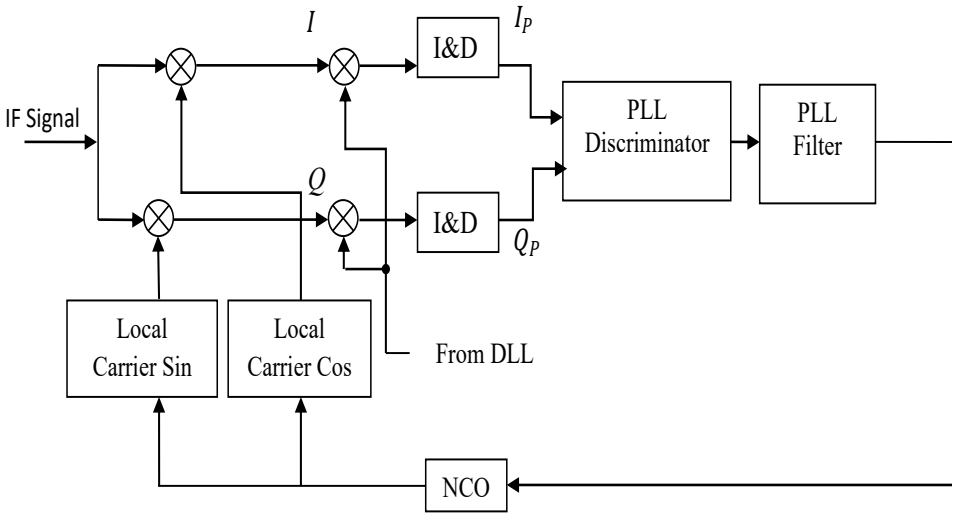

figure 3.9: PLL loop structure.

The PLL structure is shown in Figure 3.9. It can be noted from the figure that the PLL can be divided into two branches, I and Q. The signal after conversion to the intermediate

frequency (IF) is first multiplied by a replica of the spreading signal generated by the DLL. Then, two local carriers—one in phase and the other in quadrature—are multiplied with the input signal separately. Performing these multiplications in the I and Q branches results in [94]:

$$b^i(t)\cos(2\pi f_{IF}t)\cos(2\pi f_{IF}t+\varphi) = \frac{1}{2}b^i(n)\cos(\varphi) + \frac{1}{2}b^i(t)\cos(4\pi f_{IF}t+\varphi) \tag{3.20}$$

$$b^i(t)\cos(2\pi f_{IF}t)\sin(2\pi f_{IF}t+\varphi) = \frac{1}{2}b^i(t)\sin(\varphi) + \frac{1}{2}b^i(t)\sin(4\pi f_{IF}t+\varphi) \tag{3.21}$$

Here, φ represents the phase difference between the input signal's phase and the local replica's phase. The two resulting signals are then filtered by low-pass filters to eliminate double-frequency terms, leading to:

$$I^i = \frac{1}{2}b^i(t)\cos(\varphi) \tag{3.22}$$

$$Q^i = \frac{1}{2}b^i(t)\sin(\varphi) \tag{3.23}$$

3.4.2 Phase Discriminator

A phase discriminator's primary function is to determine the phase error, φ, between the local carrier signal and the residual carrier phase of the received signal. For signal tracking in GNSS systems, and particularly because of navigation bit changes, a Costas loop is often preferred (see Figure 3.10) [54]. This loop type employs a phase discriminator that is insensitive to offsets of 0° and ±180° [54]. In fact, at these phase offsets, the only times the outputs of the discriminator are non-zero are when the actual phase error is 0° or $pm180°$. The output of the discriminator must be some function of the phase error φ [15].

There are different types of discriminators, depending on the application, and their complexity varies according to the level of implementation complexity. One of the most common and widely accepted types is the Dot Product (DP) discriminator. Its formulation can be found in [94] and is presented as follows :

$$D_P = I_P Q_P \tag{3.24}$$

The output of the DP discriminator is proportional to $\sin(2\varphi)$. Another possible discriminator is the classic arctangent discriminator, defined as [94].

$$\varphi = \arctan\left(\frac{Q}{I}\right) \tag{3.25}$$

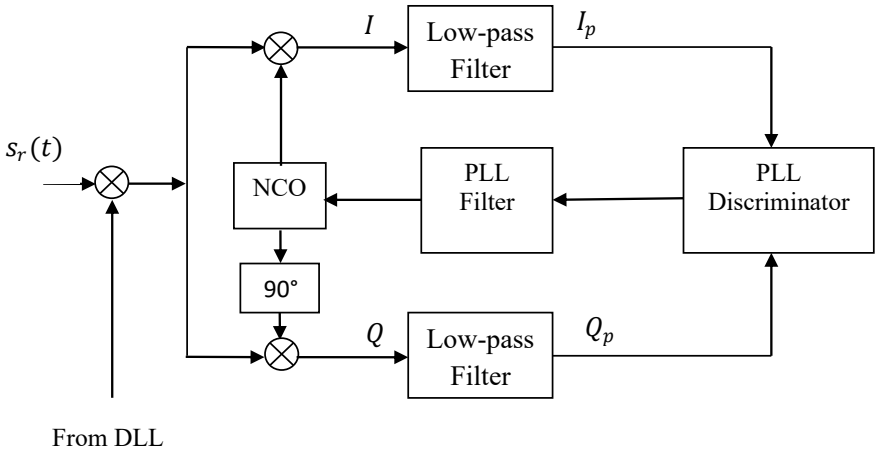

figure 3.10: Costas loop block diagram.

The output from this type of discriminator represents the frequency error. This output will then be used to produce a control signal for the Numerically Controlled Oscillator (NCO), which makes adjustments to the carrier frequency f_{cr}.

3.4.3 Delay Locked Loop

The primary objective of a code tracking loop is to continuously follow the time-varying phase of the received PRN code, $c(t-\tau)$, within the GNSS signal. This is achieved by maximizing the CF between the locally generated code and the received code, relative to their phase difference τ, while accounting for the Doppler frequency shift, f_{dop}, caused by the Doppler effect [15]. Upon successful tracking, the code tracking loop outputs a replica of the code that is perfectly aligned with the incoming received code. This loop is fundamentally a DLL, often referred to as an early-late tracking loop [15]. 3.11 illustrates the basic functional diagram of a DLL, which typically comprises a discriminator, a loop filter, an NCO, and a PRN code generator [15].

The two primary classes of DLL for code tracking are coherent and non-coherent. Coherent DLL employs PLL to lock local carrier replicas to the phase of the incoming signal, deriving discriminator functions necessary for ACF peak detection. However, this approach is often too GNSS-sensitive because it requires code tracking to be completed fully before the carrier lock is achieved. On the other hand, a non-coherent DLL operates

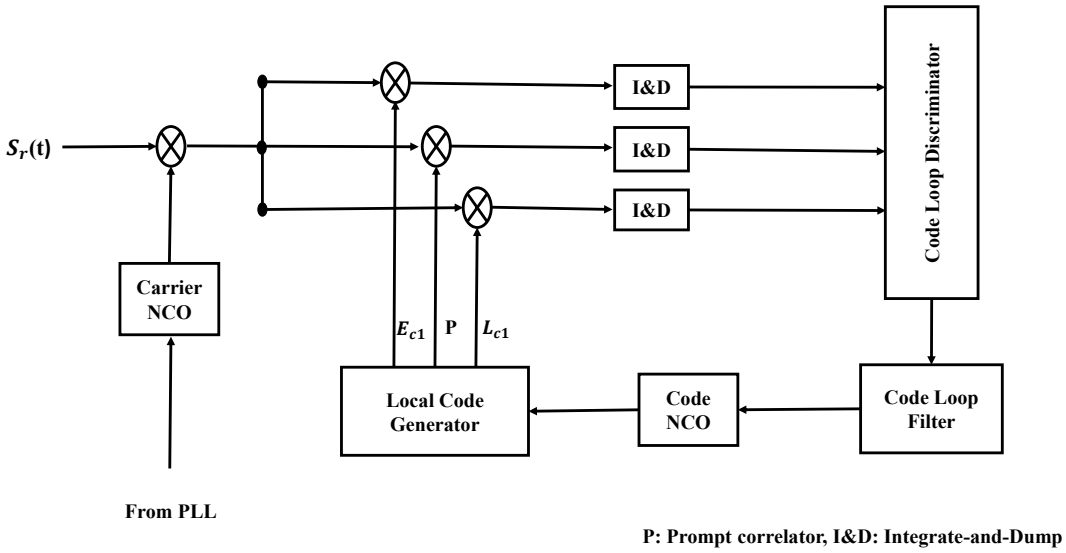

figure 3.11: Basic DLL block diagram.

at the intermediate frequency level. Non-coherent DLL addresses the Doppler shifts and unknown phases of the carrier. They show robust tracking with bandpass correlators and envelope detectors when carrier phase alignment is absent.

Both configurations utilize two independent code correlators to refine the estimated delay, $\hat{\tau}$. The input signal, $S_{IF}(t)$, after intermediate frequency conversion, is correlated with an early version, $c(t-\hat{\tau}+\frac{\Delta}{2}T_c)$, and a late version, $c(t-\hat{\tau}-\frac{\Delta}{2}T_c)$, of the locally generated PRN code. The parameter Δ represents the normalised phase difference between the early and late correlators. Thus, the output from the early correlator is given by [15]:

$$E_{c1}(t,\tau,\hat{\tau}) = c(t-\tau)c(t-\hat{\tau}+\frac{\Delta}{2}T_c) \tag{3.26}$$

Moreover, the output from the late correlator is given by [75]:

$$L_{c1}(t,\tau,\hat{\tau}) = c(t-\tau)c(t-\hat{\tau}-\frac{\Delta}{2}T_c) \tag{3.27}$$

The output of the DLL discriminator is the difference between the late ($L_{c1}(t)$) and early (E_{c1}) correlator outputs. This difference generates the error signal, denoted as $\epsilon(t,\tau,\hat{\tau})$, which is given by [94]:

$$\epsilon_r(t,\tau,\hat{\tau}) = L_{c1}(t,\tau,\hat{\tau}) - E_{c1}(t,\tau,\hat{\tau}) \tag{3.28}$$

$$= c(t-\tau)\left[c(t-\hat{\tau}-\frac{\Delta}{2}T_c) - c(t-\hat{\tau}+\frac{\Delta}{2}T_c)\right] \tag{3.29}$$

The characteristic function of the discriminator, $\epsilon(\tau-\hat{\tau})$, can take various forms, which will be detailed later. This discriminator function is used to control the NCO, which in turn adjusts the code generator's clock to establish fine synchronization.

3.5 THMA Performance in MP Environments

In addition to the previously mentioned "near-far" problem, MP can also arise from reflection or diffraction of the PL signal by tall buildings, trees, and other objects, potentially causing performance degradation in participatory GNSS receivers [96]. In the following, the primary focus will be on the effect of MP on THMA signal estimation. Finally, this chapter presents detailed methods for mitigating MP.

Based on the THMA signal estimation technique given in 3.3.1, it is known that the influence of the MP on the THMA pulse can be reduced to the effect on τ_p, which also includes the effect on the integral part τ_{in} and the fractional part τ_{fr} [6].

3.5.1 Integral Part Performance

The distortion of peak interval estimation for τ_{ip} due to MP interference can compromise the accuracy of the detected τ_{in}. Fortunately, this adverse effect can be alleviated through a simple peak consolidation step.

MP suppression is effective provided that the MP delay τ_{MP} exceeds a single chip period T_c. However, if an MP component remains after DSSS signal despreading, its correlation peak will typically appear close to the LOS peak, as illustrated in Figure 3.12. Since the TH pulse duration T_p is much larger than the chip duration T_c (where $T_p = \mathcal{M}T_c$), it is feasible to merge the MP correlation peak into the LOS peak. The merged result is normalized to 1, enabling reliable mapping and ensuring that the detection process for τ_{ip}, as described in 3.3.1, remains valid.

3.5.2 Fractional Part Performance

Regarding the τ_{fr} parameter, the PL signal is affected by MP in the same way as a standard GNSS signal. A significant disturbance in the detection of τ_{fr} arises only when the MP delay is shorter than a single PRN chip duration, T_c.

According to the analysis presented in [94], MP can introduce a maximum detection error of approximately one-quarter of the E-L spacing within the DLL. For the case of a

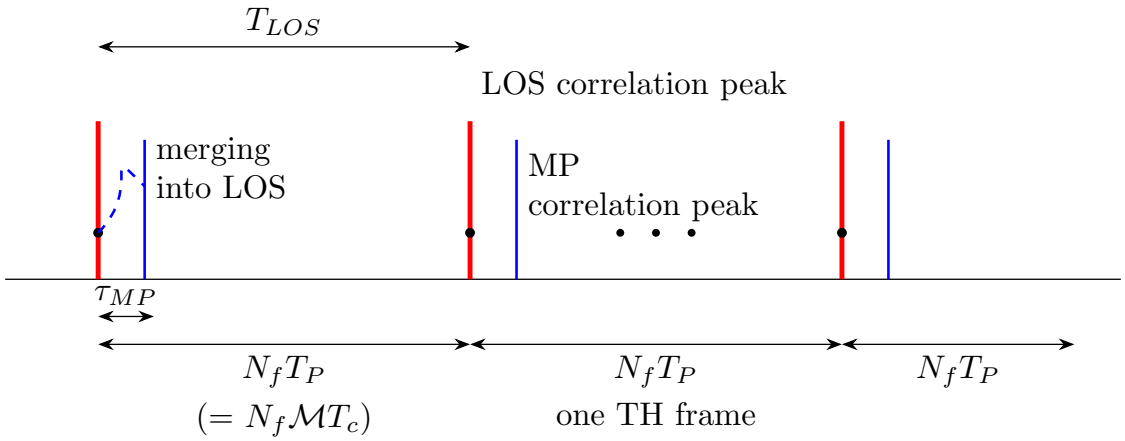

figure 3.12: Merging of MP and LOS correlation peaks.

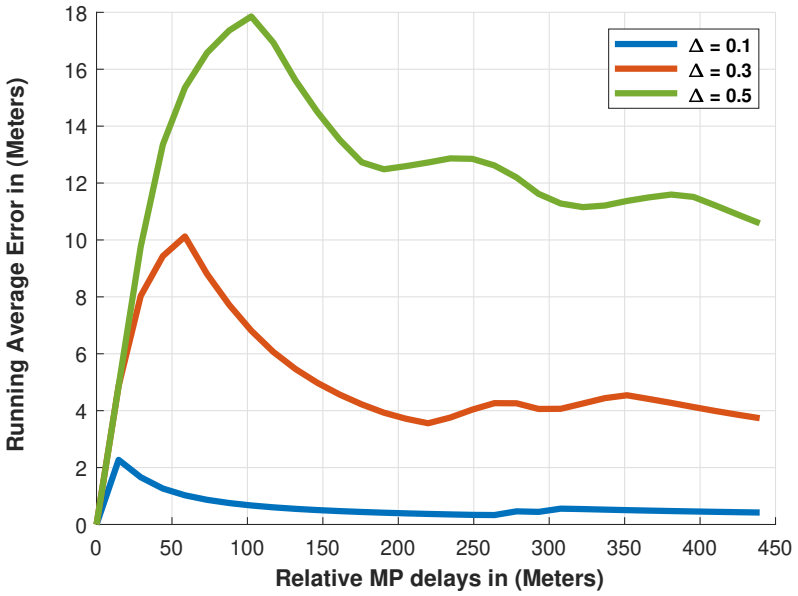

figure 3.13: RAE of the DLL, considering a range of MP delays and E-L spacings (Δ), given a fixed MP-to-LOS signal amplitude ratio of 0.5.

single MP component, Figure 3.13 illustrates the DLL's RAE across different MP delays and E-L correlator spacings. In practice, a common strategy to enhance robustness against MP is to adopt narrow correlator spacing, for example, $\Delta \leq 0.1T_c$.

Mitigating the MP interference has been a central challenge in GNSS research for decades, leading to the development of various mitigation techniques. These include improvements in antenna design [58, 59], advanced signal-processing methods [97–100], and baseband-level strategies. Among these, baseband techniques are particularly attractive due to their simplicity and cost-effectiveness, especially when compared to the adoption

of modern GNSS signals, such as BOC [101].

Baseband MP mitigation approaches can be broadly categorized into two types: parametric and nonparametric. Parametric methods model the MP channel by estimating parameters such as delay, amplitude, and phase, which are then used to cancel the interference actively. Nonparametric methods, by contrast, modify the receiver's correlator architecture to reduce sensitivity to MP without explicitly modeling the channel. This thesis focuses on mitigating MP effects in the fractional component of the TH signal, a challenge closely analogous to that encountered in conventional GNSS signals. As such, the study of these techniques is both relevant and necessary [19].

Building on this focus, the following sections provide an overview of several influential nonparametric baseband techniques. These methods primarily rely on carefully designed correlators that reshape the DLL discriminator function to suppress MP-induced errors. We review approaches ranging from the foundational NC to more advanced architectures such as the DD, EDD, and SLG.

In this context, the received signal $r(t)$ is modeled as the sum of the transmitted signal $s(t)$, its MP components, and additive noise. The LOS signal's propagation delay τ_0 is particularly important, as it directly impacts trilateration-based receiver localization. The received signal can be expressed as:

$$r(t) = \sum_{k=0}^{K-1} \alpha_k s(t - \tau_k) + w(t) \tag{3.30}$$

Here, α_k denotes the complex gain (amplitude and phase) of the k^{th} path, τ_k is the delay introduced by the k^{th} path, $w(t)$ represents AWGN, and τ_0 corresponds to the LOS propagation delay.

The transmitted signal $s(t)$ is modeled as [19]:

$$s(t) = \Re\left\{ b(t)\, \mathrm{BOC}(m, n, \varphi)\, e^{j2\pi f_{cr} t} \right\}, \tag{3.31}$$

where f_{cr} is the carrier frequency, $b(t)$ represents the data signal with power P_{owr}, and the modulated signal envelope $\mathrm{BOC}(m, n, \varphi)$ encodes the PRN code $c(t)$ onto a sinusoidal waveform.

In such an environment, the DLL discriminator function (DLL-DF) is given by [19, 102, 103]:

$$\mathrm{DF}_{s,\bar{s}}(\tau,\Delta)=\sum_{k=0}^{K-1}\alpha_k\left[R_{s,\bar{s}}(\tau+\Delta/2-\tau_k)-R_{s,\bar{s}}(\tau-\Delta/2-\tau_k)\right]+\left[\bar{w}(\tau+\Delta/2)-\bar{w}(\tau-\Delta/2)\right], \tag{3.32}$$

In this expression, $R(\tau)=\int s(t-\tau_k)\,\bar{s}(t-\tau)\,dt$ denotes the correlation between the received and local signals, while $\bar{w}(\tau)=\int w(t)\,\bar{s}(t-\tau)\,dt$ accounts for the correlated noise. The early ($E(\tau,\Delta)=R(\tau+\Delta/2-\tau_k)$) and late ($L(\tau,\Delta)=R(\tau-\Delta/2-\tau_k)$) correlators are derived directly from this CF.

3.6 Baseband MP Mitigation tehcniques: An Overview

Non-parametric MP mitigation, which is inherently important in designing a GNSS receiver, has made significant progress. Early refinements in code tracking due to the NC [104] were thwarted by BOC-modulated signals owing to the complexity of their CFs [105]. This stimulated further developments such as the High-Resolution Correlator (HRC) [106], Pulse Aperture Correlator (PAC) [107] as well as Strobe Correlator (SC), all of which are modifications of DD correlator [108] and other robust MP suppression techniques utilizing a multitude of advanced correlator configurations with sophisticated weighting. A summary comparison of several DD correlator variants, including PAC, SC, and HRC, is provided in Table 3.1. The table highlights key differences in their weighting schemes, implementation complexities, and strengths of MP mitigation.

table 3.1: Comparative Analysis of DD Correlator Variants

Aspect	**DD**	**PAC**	**SC**	**HRC**
Weighting Strategy	Fixed: 1 for prompt, 0.5 for secondary correlator.	Dynamic: derived from correlator pair slopes.	Fixed: 2 for primary, 1 for secondary correlator.	Adaptive: optimized for linearity and MP suppression.
Implementation Complexity	Lower.	Higher (requires slope calculation).	Moderate.	Moderate to High (dynamic optimization).
Strengths	General-purpose MP suppression.	Enhanced suppression for short-to-mid delays.	Effective for short-delay MP.	Improved robustness against MP; superior tracking accuracy.

As well as the previously mentioned innovations, differential processing and intricate correlator setups have been applied in the SLG-based method [109] and EDD correlator [110], which enhance the performance of DLL and reduce MP effects. This improves the reliability of GNSS under challenging environments.

Table 3.2 offers a concise comparative overview of the four nonparametric MP mitigation techniques: NC, DD correlator, EDD correlator, and SLG-based method. The specific details and operational characteristics of each technique will be thoroughly discussed in the following subsections.

table 3.2: Comparative Analysis of Nonparametric MP Mitigation Techniques

Feature	NC	DD	EDD	SLG
Core Principle	Narrow E-L spacing Δ.	Secondary E-L spacing (2Δ).	Multiple optimal E-L ($N \geq 2$). Flexible Δ_i/β_i.	CF reconstruct: SLG codes or diff. E-L CFs.
MP Mitigation	Significant in short-delay (up to 10x error reduction).	Enhanced in short delay. HRC/PAC: narrower Δ improvement.	Superior in short-delay via Δ_i/β_i opt.	Better in medium delay, and eliminating ambiguities.
BOC Compatibility	Problematic (CF side peaks and DLL ambiguities).	Better than NC; 2Δ sensitive in CF negative region.	Improved adaptability; potential for higher error compared to DD.	Unambiguous BOC CFs. Applicable to BOCs(m, n).
Complexity	High (BW, sampling, DSP).	Moderate (vs. NC).	High (multi-pair, β_i opt.).	Varies.
Tracking Performance	Precise; reduced dynamic range.	Improved accuracy/stability.	Optimized MP/noise/accuracy. Slight higher error ($N = 2, 3$) vs. DD.	Robust stability (clear CFs); adaptable Δ.
Key Trade-off	MP immunity vs. load/dynamic range.	MP mitigation vs. placement/weighting (Δ-dep.).	Flexibility/MP suppression vs. error/complexity.	Ambiguity resolution vs. processing effort.

3.6.1 Narrow Correlator (NC)

The NC technique enhances code phase estimation accuracy by reducing the E-L correlator interval. While traditional GNSS receivers typically use a one-chip E-L interval, which limits the counteraction of MP interference, the NC method shortens this interval, denoted as Δ, bringing the tracking point closer to the CF peak and minimizing distortions. Initially, GNSS receivers were configured to set Δ to 0.5 chips, thereby maintaining a total interval of one chip. However, the NC technique, specifically Δ_{NC}, reduces this to as little as 0.05 chips [104], significantly boosting tracking precision. Modern GNSS receivers employ even smaller values, often between 0.025 and 0.1 chips, achieving a tenfold decrease in MP-induced errors compared to standard designs.

Despite its effectiveness in improving MP mitigation and tracking accuracy, narrowing the E-L spacing introduces several challenges for receiver design, including:

- **Increased Computational Load:** Tighter correlator spacing increases the amount of pre-correlation bandwidth, sampling rates, as well as the required digital signal processing capabilities, and increases power consumption and computational complexity.

- **Compromised Dynamic Range:** Reducing the spacing of correlators diminishes the range within which the discriminator operates linearly, making it difficult for the code-tracking loop to handle large signal dynamics. This may worsen the tracking performance in situations with highly dynamic receiver conditions or rapid signal changes.

- **Challenges with BOC Signals:** NC is effective with BPSK modulated signals, but its use on BOC signals poses challenges. The side peaks of BOC signals exhibit multiple side peaks in their CFs, which lead to ambiguous tracking, increasing the chances of the code-tracking loop locking onto wrong peaks, which could result in errors or undetected signals [104].

Consequently, employing NC-based tracking techniques for GNSS receivers means there is a need to find a balance between reducing correlator spacing to suppress MP and robust tracking maintenance. This balance is critical for next-generation GNSS signals with high-order BOC modulations. Achieving the best positioning precision under changing operating conditions depends on the narrow gauge of correlator spacing, the system's signal processing performance, and the system architecture.

3.6.2 Double Delta (DD) Correlator

The DD correlator method enhances MP mitigation by introducing a second pair of E-L correlators, which modifies the conventional discriminator function. The assumption is that additional correlation points will suppress the additional short-delay MP signal distortions that are usually present in the CF. The DD method enhances direct path signal estimation by adding another pair of correlators, which are usually spaced at 2Δ, thus improving tracking accuracy and mitigating the effects of MP interference [108].

The enhancement enables seamless integration of an extra pair of correlators to the standard DF, resulting in:

$$\mathrm{DF}_{\mathrm{DD}}(\tau) = \mathrm{DF}(\tau, \Delta) - 0.5\mathrm{DF}(\tau, 2\Delta). \tag{3.33}$$

Here, employing a weighting factor of 0.5 reduces the impact of the second correlator pair, achieving a balanced compromise between MP mitigation and tracking stability. This improvement has led to the creation of numerous discriminators tailored to particular sets of signals, including the following:

- **SC method:** Unlike the DD discriminator, which symmetrically applies a weighted average to both correlator pairs, the SC technique uses 2:1 weighting on the first

pair, thereby favoring its performance:

$$\mathrm{DF}_{\mathrm{SC}}(\tau) = 2\mathrm{DF}(\tau, \Delta) - \mathrm{DF}(\tau, 2\Delta). \tag{3.34}$$

This configuration leads to improved performance in code tracking, enhancing the stability and responsiveness of the loop, lowering susceptibility to noise, and providing a reliable signal lock. At the same time, the lesser-weighted correlator pair provides short-delay MP interference suppression that is corrected without destabilizing tracking. SC is beneficial for strong tracking with effective MP suppression [111].

- **HRC / PAC approaches:** The primary distinction between DD and HRC/PAC discriminators lies in the difference in correlator spacing approach. While DD uses E-L spacing with Δ for the first pair and 2Δ for the second, HRC and PAC refine this by significantly decreasing Δ by NC principles [106, 107]. This improves the estimation of the code phase by better resolving the correlation peak, thus improving MP interference suppression, particularly for shorter delay interference. The HRC discriminator is formulated as follows [106]:

$$\mathrm{DF}_{\mathrm{HRC}} = \mathrm{DF}(\tau, \Delta_{\mathrm{NC}}) - 0.5\mathrm{DF}(\tau, 2\Delta), \tag{3.35}$$

Showing how it integrates a Svelte DD correction and utilizes an NC architecture. Through the use of reduced Δ, both HRC and PAC not only achieve better MP suppression but also improved tracking sensitivity, making them optimal for stringent GNSS applications that require precise tracking.

DD outperforms NC with a 0.1 chip spacing, but underperforms at a 0.2 chip spacing. This difference derives from where the second pair of correlators ($\mathrm{DF}(\tau, 2\Delta)$) is situated within the CF. In particular, if the spacing exceeds 0.15, the separation of $\mathrm{DF}(\tau, 2\Delta)$ will exceed 0.3, which places them in the negative region of the CF. This results in decreased sensitivity of the discriminator, impeding its ability to navigate on the direct route and alleviate MP. Therefore, NC and DD cannot be considered uniformly, as an NC system would outperform a DD system at different correlator spacings and MP conditions [112].

3.6.3 Extended Double-Delta Correlator (EDD)

The EDD correlator enhances the basic DD framework by introducing optimally spaced and weighted arrays of E-L correlator pairs, thereby improving MP and tracking resilience. The discriminator function of the EDD correlator can be defined as:

$$D_{\text{EDD}} = DF(\tau, \Delta_1) - \sum_{i=2}^{N} \beta_i DF(\tau, \Delta_i) \tag{3.36}$$

In this expression, N is the total number of E-L correlator pairs with spacing Δ_i and weight β_i. For consistent weighing, we assign a reference weight $\beta_1 = 1$ to the narrowest pair, which then serves as a basis for comparison for other pairs. This approach offers greater flexibility in the placement and adjustment of weights for the correlators, enabling the EDD correlator to perform better in eliminating short-delay MP interference compared to DD approaches. Through appropriate settings of Δ_i and β_i, the EDD technique can optimize the competing requirements of MP suppression, noise immunity, and tracking precision [110].

Determining the optimal performance of the EDD correlator requires finding the best correlator weights that minimize the theoretical enclosed area of the MP error envelope, thereby enhancing MP mitigation performance. However, with an increasing number of correlator pairs, the analytical determination of optimal weights becomes increasingly complex. For $N = 2$, the spacing between the two E-L correlator pairs primarily dictates the MP error envelope. Conversely, for $N = 3$, both the spacing and the weighting parameter β play a substantial role in shaping this envelope. To minimize its enclosed area, the optimal weights are given by [110]:

$$\beta_{\text{opt}} = \frac{2\Delta_1}{2\Delta_1 + \sqrt{2\left(\Delta_2 - \Delta_1\right)\left(\Delta_3 - \Delta_1\right)}} \tag{3.37}$$

$$\beta_{2,\text{opt}} = \frac{\beta_{\text{opt}}\Delta_3 - \Delta_1}{\Delta_3 - \Delta_2} \tag{3.38}$$

$$\beta_{3,\text{opt}} = \frac{\Delta_1 - \beta_{\text{opt}}\Delta_2}{\Delta_3 - \Delta_2} \tag{3.39}$$

Unlike standard DD discriminators, which confine the second correlator pair's area to $\Delta_2 = 2\Delta_1$, the EDD method removes this limitation, allowing for increased freedom in the selection of the correlator spacing. To further improve EDD performance, two alternative spacing designs are suggested:

- **Design 1:** The spacing of the second correlator pair is dynamically adjusted according to the relative amplitude of the MP component a_k, requiring, for its practical realization, an estimate $\hat{a}_k$:

$$(1 + a_k)\Delta_1 < \Delta_2 < 2\Delta_1, \quad \Delta_3 = 2\Delta_1 \tag{3.40}$$

- **Design 2:** A fixed spacing design which is independent of a_k, thereby facilitating more straightforward implementation:

$$\Delta_2 \geq 2\Delta_1, \quad \Delta_2 < \Delta_3 < 2\Delta_2 - \Delta_1 \tag{3.41}$$

Both designs preserve the linearity of the discriminator and enhance the robustness of tracking. However, the investigation shows that the EDD configurations ($N = 2, 3$) have slightly higher code tracking errors compared to conventional DD, indicating that the balance between flexibility and precision is geared towards flexibility [110].

3.6.4 Specified Locally Generated (SLG) method

The SLG-based approach reconstructs the CF to clear ambiguities and allow for distinct peak identification, which can be tracked as signals. This is achieved by two primary methods [109]:

- The first approach utilizes pre-constructed SLG codes to derive unambiguous CFs from BOC signals. As depicted in Figure 3.14, the SLGs code is formed by taking the difference of the shifted and iterative sums of the E-L PRN sequence. The SLGc code, on the other hand, is formed by summing the same iterative shifts and differences. Both SLGs and SLGc can be formulated as follows:

$$\mathrm{SLG}_\eta(t) = c\,(t - \Delta_\eta) \pm_\eta c\,(t + \Delta_\eta) \tag{3.42}$$

  where $\Delta_s = T_X/2m$ and $\pm_s = -$ for SLGs, while $\Delta_c = \Delta_s/2$ and $\pm_c = +$ for SLGc. These particular spacings ensure that the CF retains the primary peak of the signal and eliminates the problematic side lobes, thereby reducing tracking ambiguities.

- The second approach differs from the first one in that it keeps the original PRN sequence and does not generate new SLG-dependent codes. This approach preserves the original PRN configuration. Instead, the approach employs differential E-L (BOC-PRN) processing to reduce tracking system ambiguities while preserving, most importantly, the CF's basic properties. Assigning chip spacings in the two approaches presents a key difference. The first approach uses non-uniform spacings and $\Delta_c = \Delta_s/2$, while this approach uses uniform spacing where $\Delta_c = \Delta_s$ for both sine and cosine components. This uniformity and consistency improve overall computational efficiency while reducing side lobes and eliminating zero crossings. The effects of this method are demonstrated in Figure 3.15, which shows how differen-

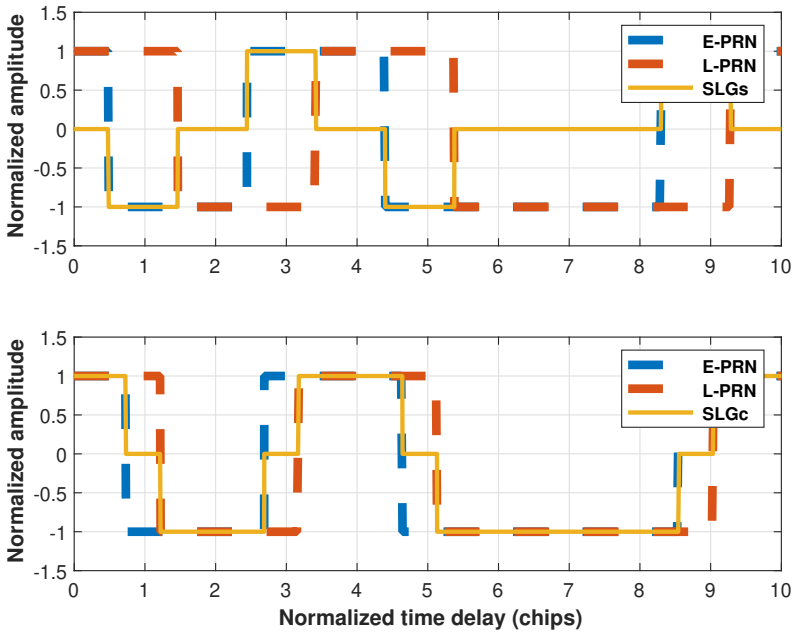

figure 3.14: Generation of SLG codes from shifted PRN sequences. (Top) Formation of the SLGs code by subtracting shifted PRN sequences. (Bottom) Formation of the SLGc code by adding shifted PRN sequences.

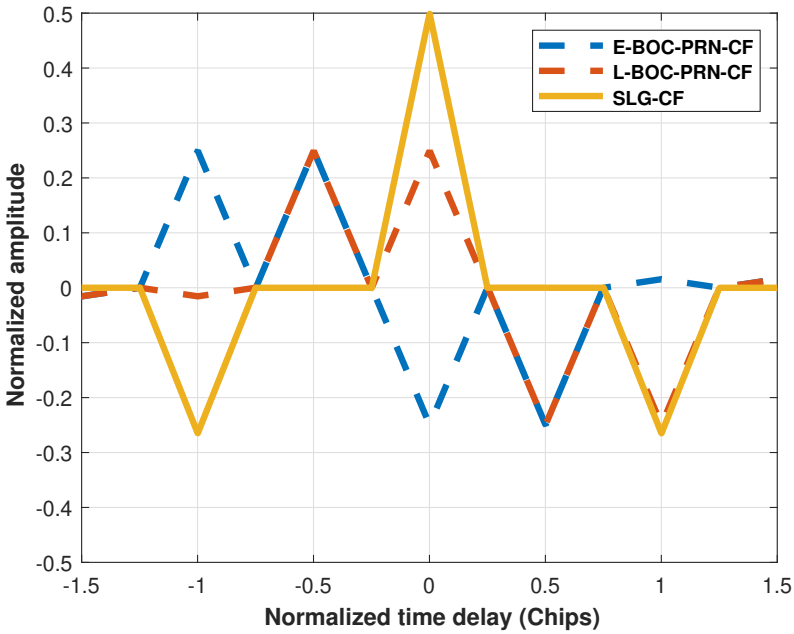

figure 3.15: Normalized amplitude responses of Early-BOC-PRN CF, Late-BOC-PRN CF, and SLG-CF for a BOC(2,1) signal, illustrating the spectral shaping effect of SLG processing on the CF.

tial processing improves tracking stability through modification of the CF without changing the PRN architecture.

Figure 3.16 depicts the E-L SLG CFs along with their DFs and the normalized DFs

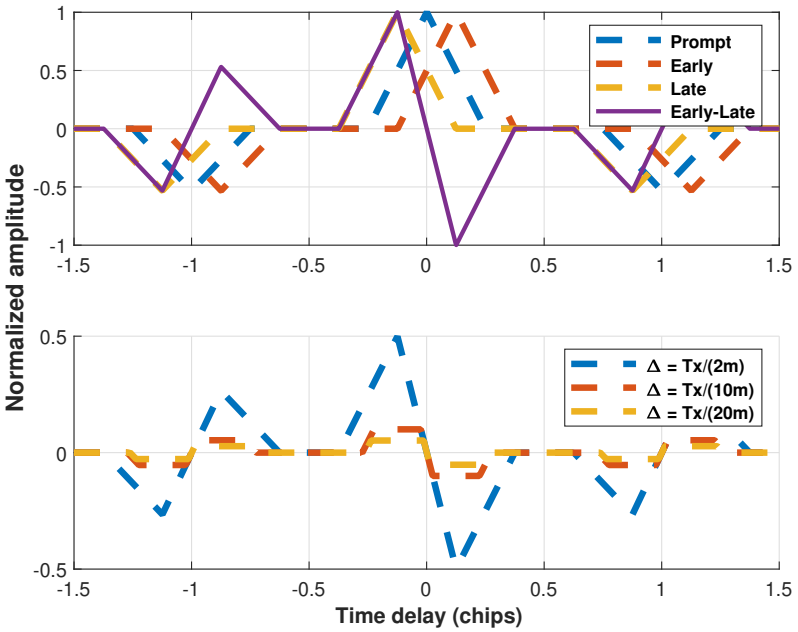

figure 3.16: Formation of SLG DF. (Top) Prompt and E-L SLG CFs contributing to the derivation of the SLG DLL-DF. (Bottom) Normalized SLG DF evaluated over varying chip spacings Δ.

concerning varying chip spacings (Δ) in the top and bottom panels, respectively. Similar to the DFs obtained using the conventional BOCc-PRN approach, the DFs obtained from the proposed method presented in this paper have the important benefit of being adaptable to varying chip spacings, rather than being fixed to a single configuration. The adaptability of Δ offers a pronounced advantage in resiliency to MP distortions because MP errors, which scale with Δ, become significantly less problematic. Furthermore, the described SLG technique enhances the versatility of any BOCs (m, n) modulated signals, thereby increasing their utility and robustness against MP interference [109].

3.7 Conclusion

This chapter has systematically detailed the essential signal processing stages within GNSS and PL receivers, covering acquisition, tracking, and MP mitigation. The discussion on signal acquisition outlined the primary objective of resolving code delay and Doppler frequency, comparing serial and parallel search methodologies, and addressing the bit sign transition problem with the zero-padding technique. The principles of signal tracking were then explored, with a detailed description of the PLL for carrier phase tracking and the DLL for code tracking, highlighting the operational distinctions between coherent and non-coherent configurations.

A special focus was placed on the unique processing requirements of PL signals. This included the critical steps for THMA signal acquisition, emphasizing the importance of accurate THMA pulse timing estimation for both pulse positioning and achieving slot-level timing resolution. The analysis also examined how MP interference specifically impacts the integral and fractional components of the THMA signal, a crucial consideration for robust PL performance.

The chapter presented an extensive overview of baseband MP mitigation techniques, providing a thorough review of advanced correlator strategies. This survey covered the foundational NC method, the DD correlator and its variants, the highly flexible EDD architecture, and the SLG-based approach. The concepts presented are fundamental to understanding how modern receivers overcome complex signal propagation challenges to achieve reliable and precise positioning. This review of established mitigation techniques provides a solid foundation for the innovative approaches that will be introduced in the chapter to follow.

Chapter 4

Efficient MP Mitigation Using Dynamic Selection and Weighting of Early-Late Correlators

4.1 Introduction

This chapter introduces a novel method to enhance positioning accuracy by mitigating MP interference, a principal obstacle for GNSS and PL systems. MP interference primarily affects THMA signals by distorting the initial phase, an effect that can be decomposed into integral and fractional components. While the integral part can be partially addressed by merging the LOS and MP peaks of the CF, the fractional component is more resilient to correction. Its mitigation requires advanced baseband strategies, similar to the techniques for standard GNSS signals discussed in the previous chapter.

However, the influence of MP on the DLL-DFs of various baseband MP mitigation techniques is especially harmful. MP parts delay, attenuate, and phase-shift signal replicas, which distort the DLL-DF. These extra terms cause systematic errors in code tracking by deviating from ideal zero-crossing behavior and drastically increasing the non-linear bounded range of the discriminator's nominal operating range. Such degradation can cause the DLL to misidentify the true correlation peak, thereby increasing the risk of tracking instability in MP-rich environments. The LOS component, which defines the ideal zero-crossing in MP-free conditions, is inherently perturbed by the presence of MP signals, causing a shift in the DF and adversely affecting its linear response. This perturbation, which can result in specific code phase shifts and offset errors, underscores the limitations of conventional fixed-number and weighting correlator approaches. Consequently, existing attempts to solve this problem often offer only partial solutions, which emphasize

a growing and critical need to develop robust, adaptive MP mitigation techniques capable of enhancing receiver performance under varying and dynamic MP conditions.

The objective of this chapter is to propose and present an adaptive strategy for more effectively mitigating the detrimental effects of MP interference within an MAA-DLL framework. This novel MAA-DLL architecture first estimates the real-time MP delay to refine the code phase. Then it reconfigures the DLL by dynamically selecting and weighting E-L correlators based on this estimation. This chapter evaluates the MAA-DLL framework using a comprehensive set of performance evaluation metrics and a suite of modern, complex GNSS signals, including BOC(2,1), BOC(4,1), higher-order BOC(10,5), BOC(14,2), and MBOC(6,1,1/11). The results demonstrate that the MAA-DLL consistently outperformed the NC, DD, EDD, and SLG methods. Notably, in MP mitigation scenarios, the architecture achieved lower RAE values across the full range of MP delays. Furthermore, its robustness was validated in combined MP and noise conditions, where it yielded a lower RMSE. This superior performance was confirmed at a fixed SNR of -30 dB and across a variable SNR range from -35 dB to -20 dB, validating its exceptional tracking accuracy.

4.2 MP Effect on the Discriminator Function

The MP components of the DF for $k \geq 1$ in Equation 3.32 add additional delayed, attenuated, and phase-shifted replicas of the received signal, therefore changing the overall DF. The added terms distort the ideal zero-crossing characteristic and introduce systematic biases, resulting in inaccurate code tracking and a reduced effective linear range within which the discriminator operates optimally. This inaccuracy may cause the DLL to misestimate the correlation peak, which increases the potential for tracking instability in areas with a high density of MP signals. In contrast, the LOS component, $k = 0$ in 3.32, represents the ideal zero-crossing value without the influence of MP. However, MP signals shift this reference point, thus moving the DF and distorting its linear response.

As shown in Figure 4.1, the DF from the LOS and MP parts of the BOC(1,1) Galileo signals within a coherent DLL is divided into six operational zones. Each of these zones alters the zero-crossing location with a coded phase change, owing to shift errors, resulting in offset errors that diminish the performance of the DLL.

As an example, the influence of four different MP delay zones on the composite DF is given in Figure 4.2. When the MP DF is non-zero and intersects with the linear region of the LOS DF, it results in a zero-crossing shift in the composite DF. This is illustrated in zones 2 (Figure 4.2a), 3 (Figure 4.2b), and 4 (Figure 4.2c). Crucially, Figure 4.2d

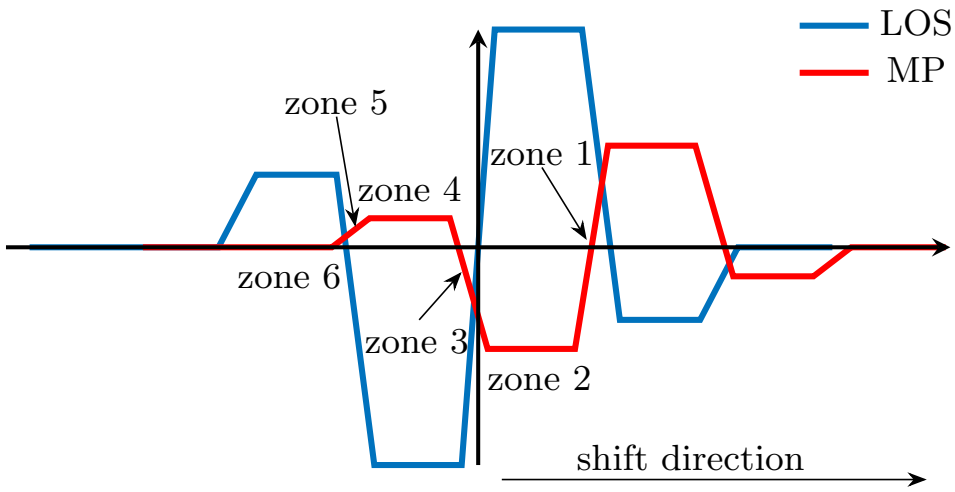

figure 4.1: DF for LOS and MP components in a coherent DLL.

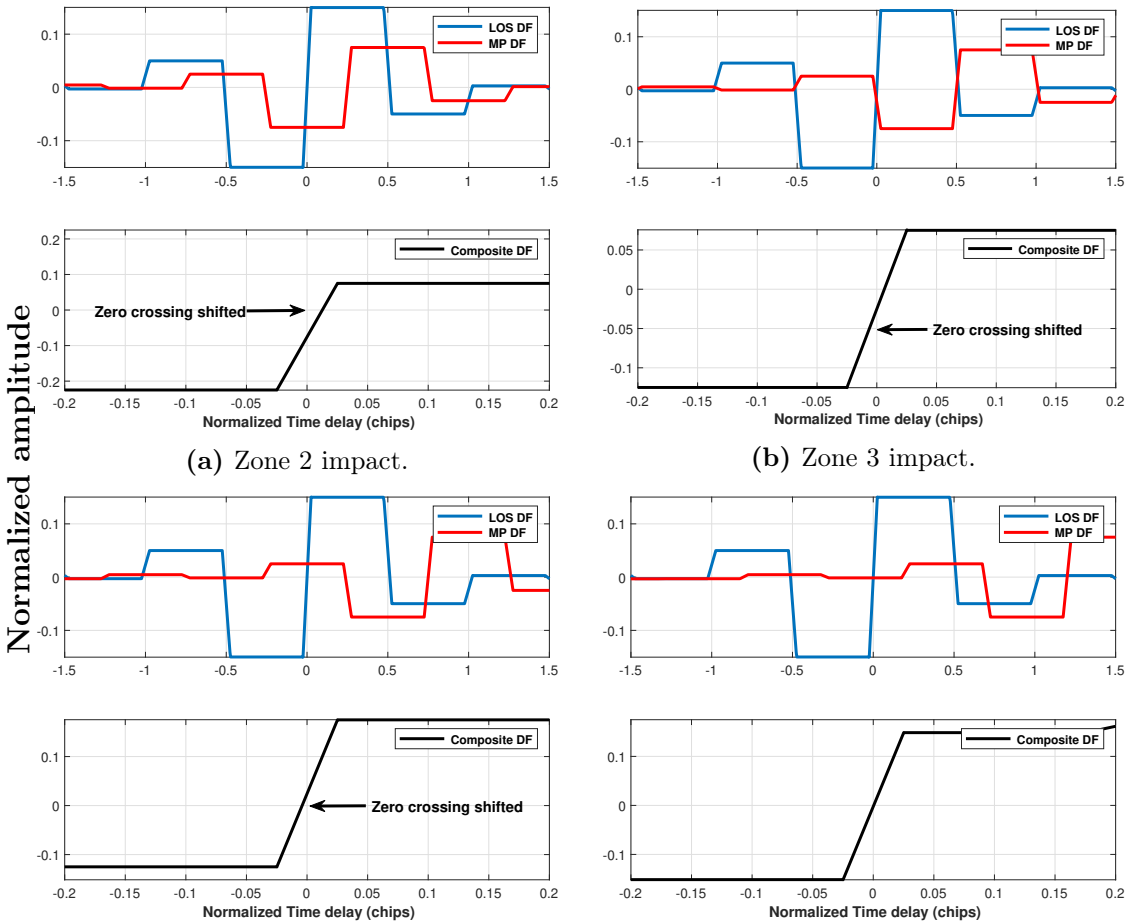

(a) Zone 2 impact.

(b) Zone 3 impact.

(c) Zone 4 impact.

(d) Zone 6 impact.

figure 4.2: Impact of different MP delay zones on the LOS DF zero-crossing point for BOC(1,1) signals.

shows that in Zone 6, where the MP DF has a value of zero at the origin, the linear range and zero-crossing point of the composite DF remain unaffected, resulting in no tracking error. This illustrates that a tracking bias is only introduced when the interfering MP DF component directly distorts the central linear slope of the LOS DF.

The analytical model for the code offset error in the general BOC(m,n) case is given in [113]:

$$\epsilon_r = A \begin{cases} \dfrac{\tau_k}{1+A} \\ 0 \le \tau_k \le (1+A)\Delta/2 \\ \dfrac{2(M-\gamma)+1}{2(1-2M)}\Delta(-1)^{\gamma} \\ d_{t2,\gamma} \le \tau_k \le d_{t1,\gamma+1} \\ -(-1)^{\gamma}\dfrac{(2(M-\gamma)+3)\,\Delta + \{4(-M+\gamma-1)\}\left\{\tau_k + \Delta/2 - T_{C/A}(\gamma-1)/(2m)\right\}}{2(1-2M)+A(-1)^{\gamma+1}\{4(-M+\gamma-1)\}} \\ d_{t1,\gamma} \le \tau_k \le d_{t2,\gamma} \\ \dfrac{(-1)^{M}\left(-\tau_k + T_X + \Delta/2\right)}{2(1-2M)-A(-1)^{M}} \\ d_{t,M} \le \tau_k \le T_X + \Delta/2 \\ 0, \\ \text{elsewhere} \end{cases} \tag{4.1}$$

In this equation, $A = \Re(a_k)$, and the auxiliary terms are defined as:

$$\gamma = \left\lceil \frac{\tau_k}{T_{sc}} \right\rceil \tag{4.2}$$

$$d_{ti,\gamma} = \Delta A(-1)^{\gamma+2-i}\frac{2(M-\gamma)+5-2i}{2(1-2M)} \quad + (-1)^{i}\Delta/2 + (\gamma-1)T_{sc}$$

$$d_{t,M} = \Delta(-1)^{M}\frac{A}{2(1-2M)} - \Delta/2 + T_X \tag{4.3}$$

In Figures 4.3 and 4.4, the SLG DF of the BOC(4,1) signal is decomposed to analyze MP interference under multiple scenarios. The figures show the DF components of the LOS signal, the MP contributions, and the resulting combined DF, obtained for different τ_k values to capture the impact of MP delays.

Figure 4.3 shows the composite DF with MP-induced zero-crossing shifts, while Figure 4.4 shows the ideal case. Analysis uses $\Delta = 0.1T_c$, $|\alpha| = 0.5$, and infinite signal bandwidth. These results highlight the impact of MP on the stability of zero-crossing estimation.

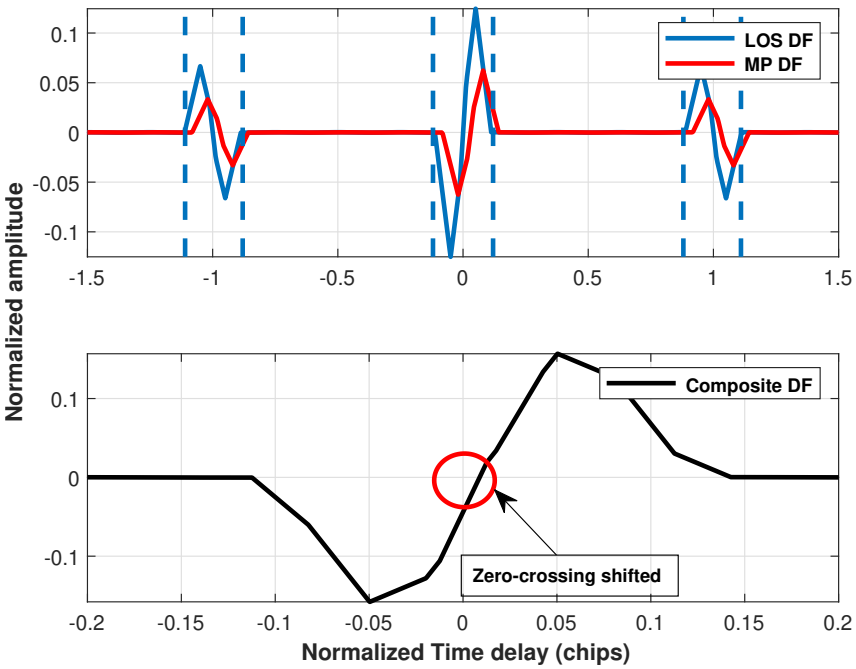

figure 4.3: MP effect on SLG-based DF for BOC(4,1) signals with $|\alpha| = 0.5$, and $\Delta = 0.1T_c$. (Top) LOS and MP-associated DF components. (Bottom) Resultant composite DF, showing the shifted zero-crossing point.

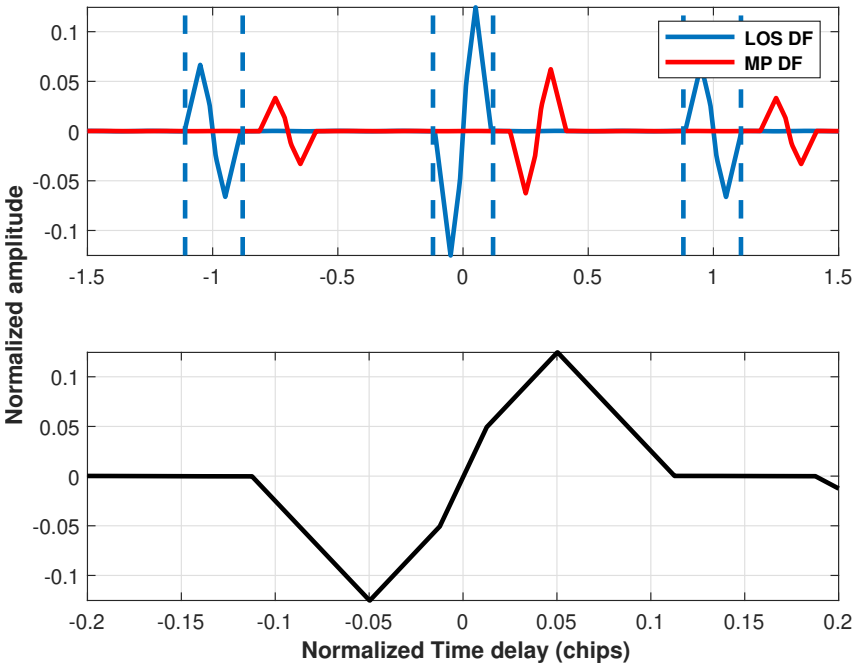

figure 4.4: Analysis of MP impact on the SLG-based DF for BOC(4,1) signals. MP amplitude is $|\alpha| = 0.5$, and correlator spacing is $\Delta = 0.1T_c$. (Top) LOS and MP-associated DF components. (Bottom) Resultant composite DF, showing the correct zero-crossing point.

Findings show that for specific MP delay ranges (dashed lines), the MP DF components

overlap with the linear segment of the LOS DF, causing a significant shift in the zero-crossing point of the composite DF. When the MP delay exceeds these ranges, its influence becomes negligible, preserving the linear region of the LOS DF and maintaining zero-crossing stability.

Additionally, as these figures demonstrate, the SLG-based approach outperforms the other methods in terms of tracking ambiguities, which is particularly evident for high modulation orders, such as $M = 8$. The more substantial this formulation, the more MP distortions vary with time delay due to the reduced influence of MP DF regions on the zero-crossing point shift.

Figures 4.5 and 4.6 present an analysis of LOS DF and the corresponding code offset errors for both SLG and DD techniques on BOC(1,1) modulated signal. This analysis illustrates how differing relative delays of a singular MP signal produce varying responses across different DLL-DF architectures, thus revealing how each shape responds to the disturbance introduced by MP signals.

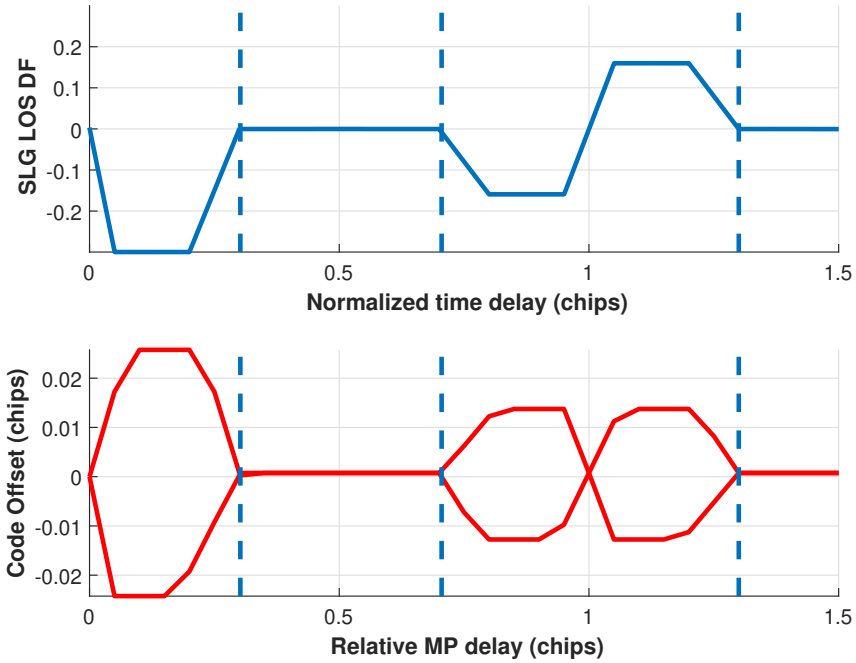

figure 4.5: MP effect on the SLG-based method DLL-DF for the BOC(1,1) modulation scheme. (Top) LOS DF. (Bottom) Code offset errors.

Figure 4.5 shows the LOS DF produced by the SLG method, which serves as the undistorted reference, thereby providing the baseline, alongside the code offset errors that indicate tracking errors due to MP interference. At the same time, Figure 4.6 shows the same case but with the DD method.

As illustrated by the boundaries, the analysis shows that each DLL-DF configuration has unique intervals of delay at which MP distortions cause different levels of code phase

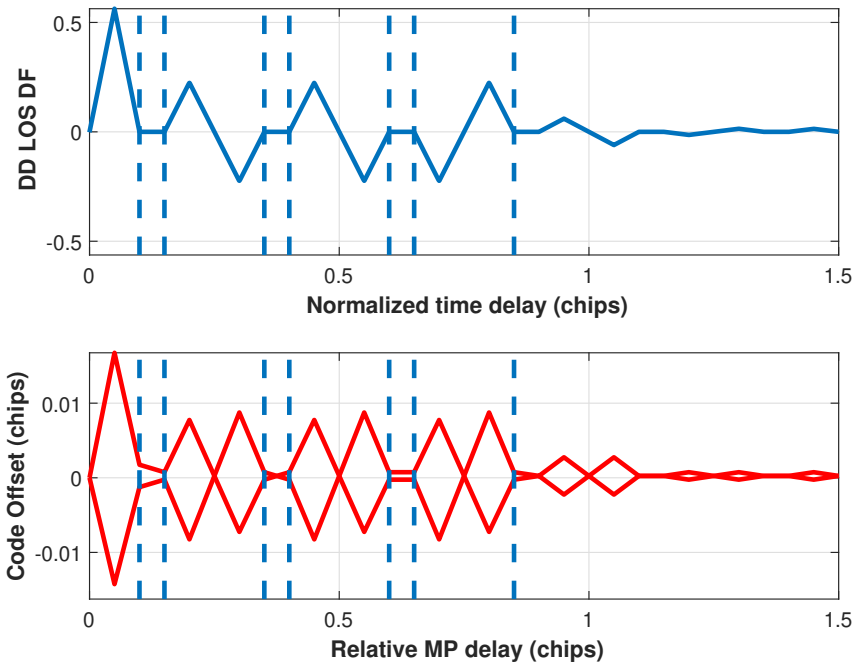

figure 4.6: MP effect on the DD-based method DLL-DF for the BOC(1,1) modulation scheme. (Top) LOS DF. (Bottom) Code offset errors.

offset error. The SLG-based strategy is more resilient in medium MP delay scenarios; it minimizes tracking bias and maintains a stable region around the zero-crossing point. On the contrary, at very short or very long delay intervals, the SLG is more prone to nonlinear drifting, causing higher levels of tracking inconsistency.

In comparison, the structure based on DD shows that the error is distributed more uniformly across the entire range of delay, which indicates that it is more robust to MP code distortions. This evaluation complements the discussion on trade-offs in the performance of SLG and DD discriminator designs about the mitigation of MP effects for different delay ranges.

4.3 Proposed Multipath-Aware Adaptive DLL

The proposed MAA-DLL improves DLL-based tracking accuracy by integrating real-time MP delay estimation with dynamic selection and adaptive weighting of E-L correlators. First introduced in our earlier work [19], it represents the core contribution of this thesis and operates in two main stages, as illustrated in Figure 4.7.

In the first stage, code phase refinement is performed by estimating the relative MP delay, $\hat{\tau}_k$, to compensate for propagation-induced errors. The second stage, referred to as adaptive DLL reconfiguration, adaptively modifies the discriminators based on selected

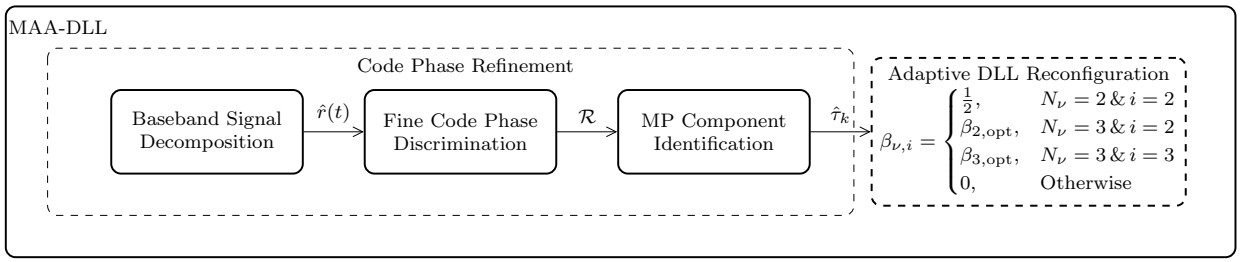

figure 4.7: Proposed MAA-DLL Block Diagram.

E-L correlator pairs and their corresponding weight coefficients, which are determined through lookup-based mapping functions. This two-stage design enables real-time adjustment of correlator spacings and weighting factors, thereby reducing tracking errors and enhancing the robustness of DLL-DF configurations against MP distortions. The following subsections detail these stages, with particular emphasis on the estimation framework and adaptive weighting technique that underpin this MP-driven approach to code phase estimation.

4.3.1 Code Phase Refinement

Our proposed methodology starts with the down-conversion of the incoming signal, $r(t)$, to its baseband form. This transformation is performed by demodulating the received signal with a complex exponential $e^{-j2\pi f_c t}$ and passing the product through a Low-Pass Filter (LPF). The resulting baseband signal, $\hat{r}(t)$, is mathematically expressed as:

$$\hat{r}(t) = \text{LPF}\left[r(t)e^{-j2\pi f_c t}\right] = \sum_{k=0}^{K-1} \alpha_k \hat{s}(t - \tau_k) + \hat{w}(t), \tag{4.4}$$

Here, $\hat{r}(t)$ signifies the downconverted received signal, $\hat{s}(t)$ represents the baseband form of the transmitted modulated signal, $\hat{w}(t)$ accounts for the filtered noise, and LPF[$\cdot$] denotes the operation of low-pass filtering, which isolates the desired baseband signal.

After conversion to baseband, the system performs an initial delay estimate to determine the estimated time for the first point in time for synchronization and processing. This estimation is performed by computing the cross-correlation of the acquired baseband signal $\hat{r}(t)$ with a locally generated code, specifically the SLG code $\bar{s}_{SLG}(t)$:

$$R_{\hat{r}(t),\bar{s}}(\tau) = \int \hat{r}(t)\bar{s}_{SLG}(t - \tau)dt. \tag{4.5}$$

The coarse delay estimate, τ_{acq}, is then identified during the signal acquisition phase as the specific τ value that maximizes this CF:

$$\tau_{acq} = \arg\max_{\tau} R_{\hat{r}(t),\bar{s}}(\tau). \tag{4.6}$$

This initial step provides a rough approximation of the signal's propagation delay. To assess the magnitude of tracking error introduced by MP distortion, the zero-crossing points ($\tau_{z,i}$) of the DF are subsequently identified using Equation 3.32:

$$\mathrm{DF}_{\hat{r}(t),\bar{s}}(\tau_{z,i}, \Delta) = 0, \quad i = \{1, 2, \cdots\}. \tag{4.7}$$

After the coarse delay acquisition, the cross-correlation process is refined by re-evaluating it with a set of precisely defined delay instants, τ_l. These refined delay instants are calculated as:

$$\tau_l = \tau_{min} + l \cdot \Delta\tau, \quad l = -\tfrac{N_0}{2}, \ldots, +\tfrac{N_0}{2} - 1, \tag{4.8}$$

where τ_l falls within the range $[\tau_{\min}, \tau_{\max}]$. The bounds are established as $\tau_{min} = \tau_{acq} - T_{C/A}$ and $\tau_{max} = \tau_{acq} + 2T_{C/A}$. The parameter N_0 is derived from $N_0 = \lfloor(\tau_{\max} - \tau_{\min})/\Delta\tau\rfloor$, and $\Delta\tau$ represents the step size, inversely related to the sampling frequency $F_e = (\Delta\tau)^{-1}$. The notation $\lfloor\cdot\rfloor$ indicates the floor operation. The refined correlation function between the received signal and the time-shifted BOC reference signal $\hat{s}_{BOC}(t - l\Delta\tau)$ is then computed:

$$R_{\hat{r}(t),\hat{s}}(\tau_l) = \int \hat{r}(t)\hat{s}_{BOC}(t - l\Delta\tau)dt. \tag{4.9}$$

The peak values of these computed correlation results, $R_{\hat{r}(t),\hat{s}}(\tau_l)$, along with their corresponding delay instants, τ_l, are subsequently stored in an array, $\mathcal{R}$, for further analytical use. This array specifically includes pairs where the correlation value is greater than its immediate neighbors:

$$\mathcal{R} = \{(\tau_l, R_{\hat{r}(t),\hat{s}}(\tau_l)) \mid R_{\hat{r}(t),\hat{s}}(\tau_l) > R_{\hat{r}(t),\hat{s}}(\tau_l \pm \Delta\tau)\}. \tag{4.10}$$

Next, the system generates updated local reference signals for both BOC and SLG components, denoted as $\tilde{s}_{BOC}(t)$ and $\hat{s}_{SLG}(t)$, respectively. These signals are adjusted to incorporate the estimated MP parameters, leading to a more precise emulation of the actual received signal. These adjusted reference signals are defined as:

$$\tilde{s}_{BOC}(t) = \hat{a}\mathrm{BOC}(m, n, \varphi)\big|_{t-\hat{\tau}_z} e^{-j\hat{\phi}} \tag{4.11}$$

$$\hat{s}_{SLG}(t) = \hat{a}\bar{s}_{SLG}(t)\big|_{t-\hat{\tau}_z} e^{-j\hat{\phi}} \tag{4.12}$$

where the refined MP delay estimate, $\hat{\tau}_z$, is identified as the delay instant in $\mathcal{R}$ that is closest to the zero-crossing point, specifically:

$$\hat{\tau}_z = \arg\min_{\tau_l \in \mathcal{R}} |\tau_l - \tau_z|, \tag{4.13}$$

The corresponding amplitude $\hat{a}$ is calculated as the fundamental part of the complex correlation value $R_{\hat{r}(t),\hat{s}}(\hat{\tau}_z)$ compensated by the phase, $\hat{a} = \Re[R_{\hat{r}(t),\hat{s}}(\hat{\tau}_z)e^{-j\hat{\phi}}]$, and the phase shift $\hat{\phi}$ is derived from the argument of this complex correlation value, $\hat{\phi} = \arg[R_{\hat{r}(t),\hat{s}}(\hat{\tau}_z)]$. These refined local reference signals are subsequently employed to compute the following residual correlations:

$$R_{\mathrm{BOC},\tilde{s}}(\tau_l) = R_{\hat{r}(t),\hat{s}}(\tau_l) - \int \mathrm{BOC}(m,n,\varphi)\tilde{s}_{BOC}(t-\tau_l)\,dt \tag{4.14}$$

$$R_{\mathrm{BOC},\hat{s}}(\tau) = R_{\hat{r}(t),\bar{s}}(\tau) - \int \mathrm{BOC}(m,n,\varphi)\hat{s}_{SLG}(t-\tau)\,dt \tag{4.15}$$

To improve the precision of estimating MP delays, the procedure involves removing the reference CFs from the primary correlation. Solving the primary correlation masks allows for capturing unmodeled MP distortions. The MP delay, $\hat{\tau}_k$, is computed from the residual signal by detecting the zero-crossing of the DF and the closest local maximum of the residual correlation function. This rigorous procedure yields an accurate description of the bias caused by propagation time delays, enabling the provision of information for the adaptive reconfiguration stage to address the computed distortion efficiently. The formal description of the procedures above is given as follows:

$$\hat{\tau}_k = \arg\min_{\tau_l \in \mathcal{Z}} |\tau_l - \hat{\tau}_{zc}|, \tag{4.16}$$

where $\hat{\tau}_{zc}$ is determined by satisfying the condition:

$$\mathrm{DF}_{\mathrm{BOC},\hat{s}}(\hat{\tau}_{zc,i},\Delta) = 0, \quad i = \{1,2,\cdots\}. \tag{4.17}$$

In this context, $\mathrm{DF}_{\mathrm{BOC},\hat{s}}(\tau,\Delta)$ is defined as the difference $R_{\mathrm{BOC},\hat{s}}(\tau+\Delta/2) - R_{\mathrm{BOC},\hat{s}}(\tau-\Delta/2)$, and the set $\mathcal{Z}$ encompasses pairs of delay instants and residual correlation values where the residual correlation exhibits local peaks:

$$\mathcal{Z} = \{(\tau_l, R_{\mathrm{BOC},\tilde{s}}(\tau_l)) \mid R_{\mathrm{BOC},\tilde{s}}(\tau_l) > R_{\mathrm{BOC},\tilde{s}}(\tau_l \pm \Delta\tau)\}. \tag{4.18}$$

Finally, the estimated MP delay $\hat{\tau}_k$ is then applied in the second stage of the proposed DLL, facilitating the dynamic selection and weighting of the E-L correlator.

4.3.2 Adaptive DLL Reconfiguration

This stage represents the 'adaptive' part of the MAA-DLL, the part in which the system dynamically adjusts its DLL-DF for the specific MP delay information obtained from the code phase refinement stage. This is done optimally by picking the E-L correlator pairs and their corresponding weighting coefficients.

The MAA-DLL system, illustrated in Figure 4.8, is a real-time adaptive system to MP interference, whose core operation is the MP Delay estimation block that computes the delay of the signal reflection, $\hat{\tau}_k$, and drives a query to the Lookup table, which contains optimal, pre-determined strategies; this table, generated through prior weights computation for different E-L correlator spacings (Δ_1, Δ_2, Δ_3), is designed to relay a computed delay to a specific control index, ν.

The measurement is processed by the table, which in turn predicts the delay, maps it to a specific control index ν, and deliberately activates its programmed actions. Through the three actions and control index ν, the Lookup table simultaneously governs the number of active E-L correlator pairs (N_ν), the adaptive weights ($\beta_{\nu,i}$), and the binary state (S_ν) of the subcarrier NCO. This dynamic reconfiguration allows the system to generate a composite DLL-DF precisely tailored to mitigate prevailing MP conditions, ensuring robust and accurate tracking.

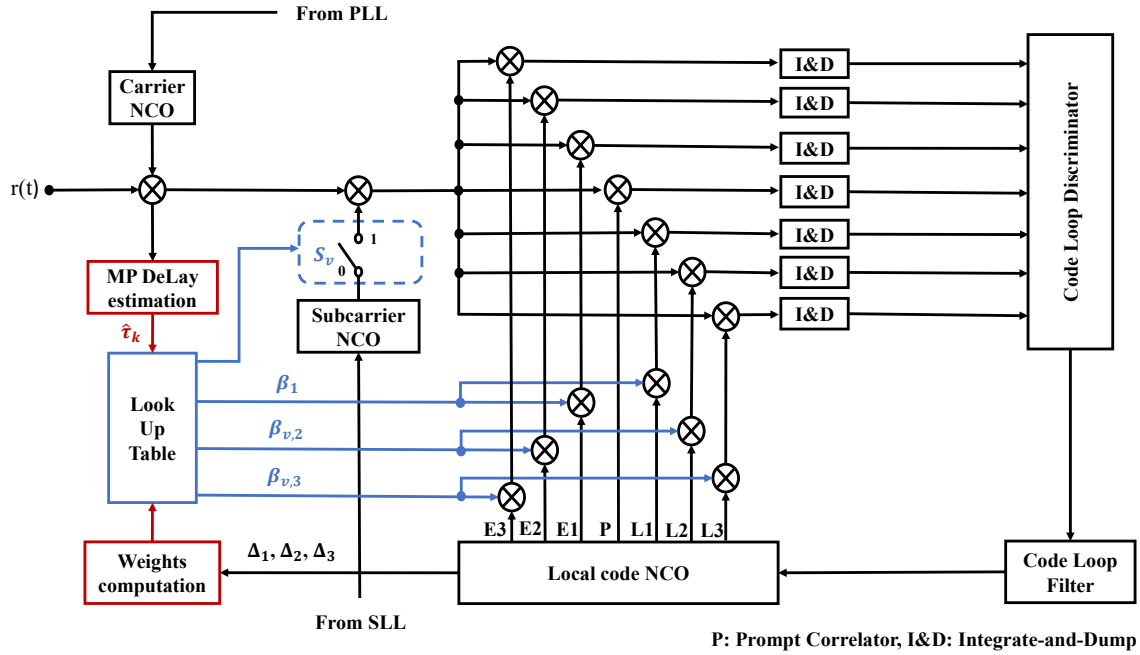

figure 4.8: Schematic illustration of the proposed MAA-DLL.

The fundamental goal of this design is to generate a new discriminator characteristic

that offers improved linearity and significantly reduced sensitivity to the errors induced by MP. The mathematical formulation for the MAA-DLL's DF is given by:

$$D_{\text{MAA-DLL}} = DF(\tau, \Delta_1) + \sum_{i=2}^{N_\nu} \beta_{\nu,i} DF(\tau, \Delta_i) \tag{4.19}$$

Let's deconstruct the elements of this adaptive discriminator:

- **The Baseline Discriminator ($DF(\tau, \Delta_1)$):** This term stands for the DLL-DF created by the smallest spacing Δ_1 of the E-L correlator. Such narrow spacing is taken for precision in ideal, MP-free conditions, serving as the primary or foundational DF. It is always included in the composite discriminator.
- **Adaptive Weighted Contribution ($\sum_{i=2}^{N_\nu} \beta_{\nu,i} DF(\tau, \Delta_i)$):** This summation forms the core of the adaptive mechanism by incorporating the weighted contributions of wider E-L correlator pairs with spacings Δ_2, Δ_3, and beyond. The weighting coefficients are adjusted dynamically to reflect changing MP conditions:
  - **The MP-Driven Delay Interval Index (ν):** This index is directly associated with the estimated MP delay $\hat{\tau}_k$ from the code phase refinement step. ν describes a fixed delay interval which contains $\hat{\tau}_k$ so that $\hat{\tau}_k \in [T_{\nu-1}, T_\nu]$. This is the critical interlink that enables the MAA-DLL to be "MP-Aware," allowing it to respond to tailored MP conditions. Each specific delay interval ν is tied to a fixed set of parameters stored in a look-up table on the receiver side (Table 4.1).

table 4.1: Lookup Table for MAA-DLL method

Index (ν)	**MP Delay Interval**	S_ν	N_ν	$\beta_{\nu,2}$	$\beta_{\nu,3}$
1	$[0, T_1]$	S_1	N_1	$\beta_{1,1}$	$\beta_{1,2}$
2	$[T_1, T_2]$	S_2	N_2	$\beta_{2,1}$	$\beta_{2,2}$
3	$[T_2, T_3]$	S_3	N_3	$\beta_{3,1}$	$\beta_{3,2}$
$\vdots$	$\vdots$	$\vdots$	$\vdots$	$\vdots$	$\vdots$
n_1	$[T_{n_1-1}, T_{n_1}]$	S_{n_1}	N_{n_1}	$\beta_{n_1,1}$	$\beta_{n_1,2}$

  - **Dynamic Number of E-L Correlator Pairs (N_ν)**: From the table and based on ν, this parameter determines the additional E-L correlator pairs that are activated for tracking within the specified MP delay range. For example, in the case of milder MP, correlator pairs are less likely to be needed, which decreases the computational burden. On the other hand, more severe MP

conditions are likely to require more pairs to be processed to provide more information for the discriminator to use, which improves robustness.

– **Adaptive Weighting Coefficients** ($\beta_{\nu,i}$): Obtained from the lookup table, these coefficients define the contribution of additional correlator pairs to the composite DF. The narrowest correlator pair with spacing Δ_1 serves as the baseline, with its weight fixed at $\beta_1 = 1$. The remaining coefficients, $\beta_{\nu,2}$ and $\beta_{\nu,3}$, are considered optimal as they are derived from extensive simulations and are determined dynamically from the MP delay interval ν, with their values computed using Equations 3.38 and 3.39.

The general rules for these coefficients are:

$$\beta_{\nu,i} = \begin{cases} \frac{1}{2}, & N_\nu = 2 \text{ and } i = 2 \\ \beta_{2,\text{opt}}, & N_\nu = 3 \text{ and } i = 2 \\ \beta_{3,\text{opt}}, & N_\nu = 3 \text{ and } i = 3 \\ 0, & \text{Otherwise.} \end{cases} \tag{4.20}$$

– **Subcarrier State Adaptation (S_ν)** : For BOC modulated signals, this binary indicator, where $S_\nu = 1$ denotes a subcarrier presence and $S_\nu = 0$ indicates its absence, is pivotal. Different types of BOC signals exhibit different subcarrier behaviours. The system achieves optimal correlation alignment, essential for accurate tracking, particularly in the presence of MP interference, by modulating the local code's subcarrier state based on the lookup table in adaptive MP interference environments.

This adaptive configuration overcomes the limitations of fixed-weighting correlators. Traditional static spacings and weights cannot address all delays of MP interference (including short, medium, and long delays) within a single design, resulting in performance trade-offs in many environments. In contrast, the MAA-DLL continuously refines the discriminator settings in real time, making the system:

- **More Linear:** It maintains a broader linear operating range for the composite DF, which is paramount for stable and accurate tracking in dynamic environments.
- **Less Susceptible to MP Distortions:** With the MAA-DLL's intelligent engagement and weighting of different pairs of correlators, the systematic biases and shifts caused by MP interference can be effectively "cancelled" or substantially diminished.

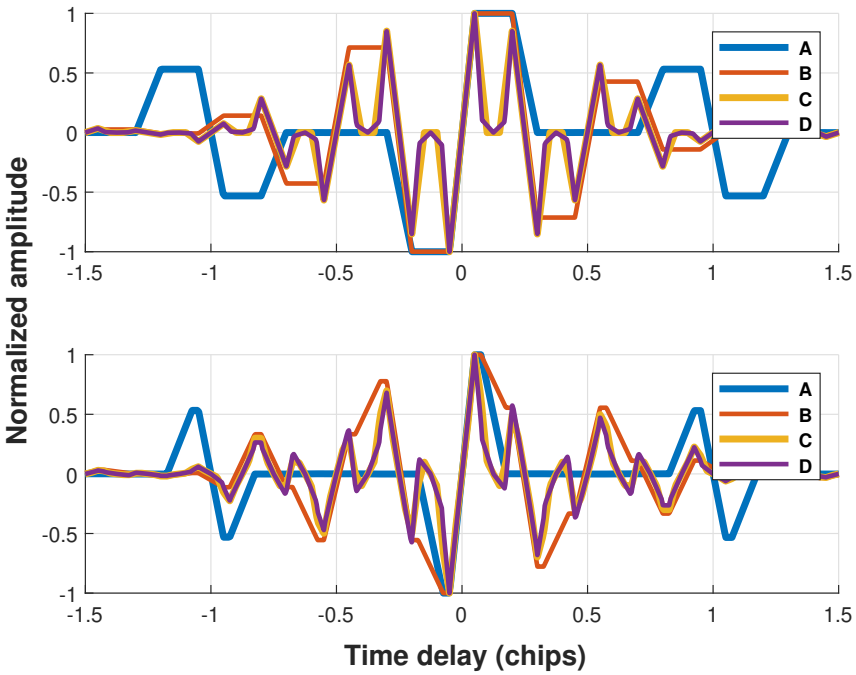

figure 4.9: MAA-DLL DF configurations presented in Table 4.2: $\mathrm{BOC}_s(2,1)$ (Top) vs. $\mathrm{BOC}_c(2,1)$ (Bottom) for $k = 0$ in Equation 3.32.

table 4.2: MAA-DLL DF configurations (A, B, C, D).

DLL-DF configurations	S_ν	N_ν	$\beta_{\nu,2}$	$\beta_{\nu,3}$
A	0	1	0	0
B	1	1	0	0.0
C	1	2	0.5	0
D	1	3	0.55	0.047

The MAA-DLL operates in four DF modes, labeled A–D, as summarized in Table 4.2. Each mode specifies a unique set of adaptive parameters: the subcarrier state (S_ν), number of active E-L correlator pairs (N_ν), and weighting coefficients ($\beta_{\nu,i}$). Mode A uses only the baseline correlator, while modes B–D progressively add correlator pairs with nonzero weights to improve robustness against MP. These configurations implement the governing equation 4.19, and their effect is illustrated in Figure 4.9, which shows the resulting composite DFs for sine- and cosine-phased BOC(2,1) signals.

As described in Section 4.2, each configuration produces a distinct DF shape with zones tailored to suppress specific classes of MP interference. To sustain optimal tracking performance, the MAA-DLL leverages a diverse set of DFs that respond effectively under varying conditions. Its core function is the dynamic real-time selection of the most suitable correlator setting from the predefined table, adapting to the prevailing MP delay and tracking environment.

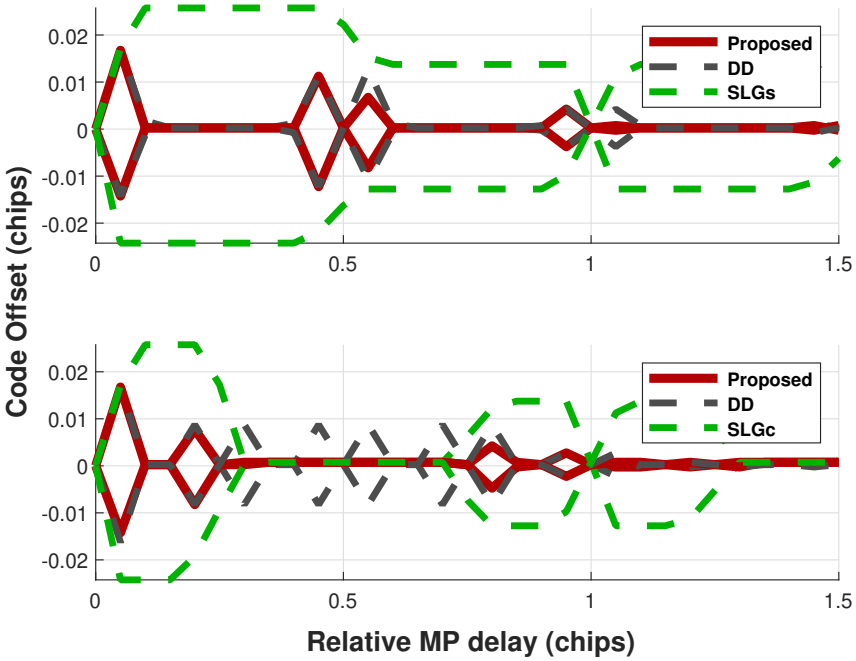

figure 4.10: Code offset behavior against relative MP delays of DD, SLG, and the proposed MAA-DLL method, for BOC(1,1) modulation schemes: (Top) $\text{BOC}_s(1,1)$; (Bottom) $\text{BOC}_c(1,1)$.

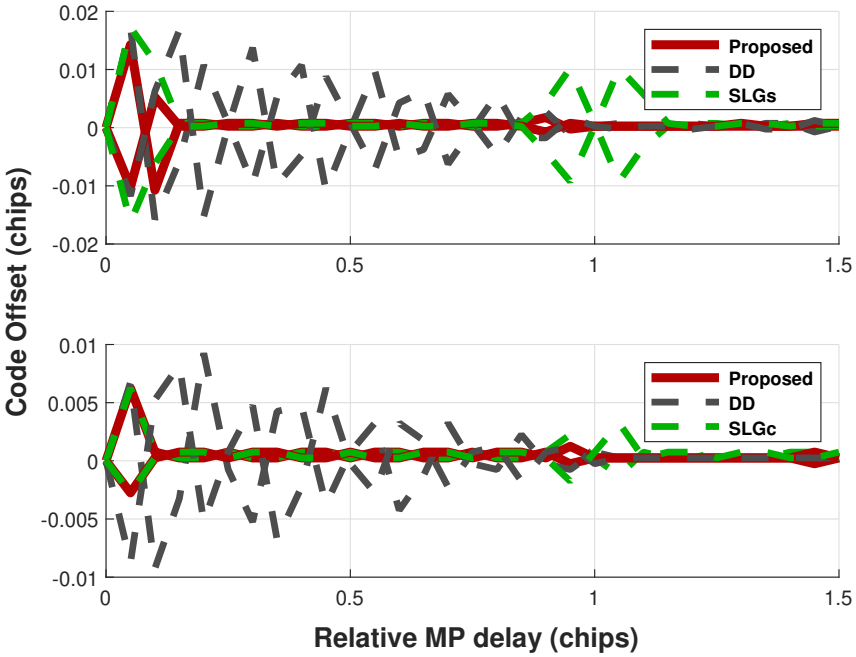

figure 4.11: Code offset behavior against relative MP delays of DD, SLG, and the proposed MAA-DLL method, for BOC(6,1) modulation schemes: (Top) $\text{BOC}_s(6,1)$; (Bottom) $\text{BOC}_c(6,1)$.

Figures 4.10 and 4.11 visually present the operational characteristics of the MAA-DLL's adaptive nature across different GNSS signal types. This includes $\text{BOC}_c(1,1)$, $\text{BOC}_s(1,1)$, $\text{BOC}_c(6,1)$, and $\text{BOC}_s(6,1)$ signals, representing both fundamental and com-

plex MBOC signal structures. For comparison, the code offset behavior of conventional fixed-configuration techniques, DD and SLG, is also depicted. A consistent correlator spacing configuration is maintained for all methods: $\Delta_1 = 0.1T_c$, $\Delta_2 = 1.6\Delta_1$, and $\Delta_3 = 2.5\Delta_1$.

table 4.3: MAA-DLL Lookup Table for BOC$_s$(1,1) Modulation (Corresponds to Top Panel of Figure 4.10)

Index (ν)	**MP Delay Interval**	S_ν	N_ν	$\beta_{\nu,2}$	$\beta_{\nu,3}$
1	$[0, 0.05T_c]$	1	3	0.55	0.047
2	$[0.05T_c, 0.4T_c]$	1	2	0.5	0
3	$[0.4T_c, 0.5T_c]$	1	3	0.55	0.047
4	$[0.5T_c, 0.55T_c]$	1	1	0	0
5	$[0.55T_c, 1T_c]$	1	2	0.5	0
6	$[1T_c, 1.05T_c]$	1	1	0	0
7	$[1.05T_c, 1.4T_c]$	1	2	0.5	0
8	$[1.4T_c, 1.5T_c]$	1	1	0	0

table 4.4: MAA-DLL Lookup Table for BOC$_c$(1,1) Modulation (Corresponds to Bottom Panel of Figure 4.10)

Index (ν)	**MP Delay Interval**	S_ν	N_ν	$\beta_{\nu,2}$	$\beta_{\nu,3}$
1	$[0, 0.15T_c]$	1	2	0.5	0
2	$[0.15T_c, 0.275T_c]$	1	3	0.55	0.047
3	$[0.275T_c, 0.7T_c]$	0	1	0	0
4	$[0.7T_c, 0.75T_c]$	1	3	0.55	0.047
5	$[0.75T_c, 0.8T_c]$	1	1	0	0
6	$[0.8T_c, 1T_c]$	1	3	0.55	0.047
7	$[1T_c, 1.1T_c]$	1	1	0	0
8	$[1.1T_c, 1.3T_c]$	1	3	0.55	0.047
9	$[1.3T_c, 1.5T_c]$	0	1	0	0

The specific dynamic selection and weighting strategies, implemented through lookup tables, underpin the MAA-DLL's adaptive behavior. Table 4.3 details the parameters for BOC$_s$(1,1) (top panel of Figure 4.10), while Table 4.4 corresponds to BOC$_c$(1,1) (bottom panel of Figure 4.10). Similarly, Table 4.5 outlines the strategy for BOC$_s$(6,1) (top panel of Figure 4.11), and Table 4.6 for BOC$_c$(6,1) (bottom panel of Figure 4.11).

Across all depicted signal schemes in Figures 4.10 and 4.11, the MAA-DLL consistently maintains a notably tighter and more uniform code offset curve across varying relative MP delays. This contrasts with fixed-configuration methods, such as DD and SLG, which typically exhibit more pronounced oscillations and wider variations in their code offset behavior.

The MAA-DLL's ability to maintain this relatively narrow and stable offset is a direct consequence of its dynamic adaptation. Optimal correlator pairs and their weights

table 4.5: MAA-DLL Lookup Table for $BOC_s(6,1)$ Modulation (Corresponds to Top Panel of Figure 4.11)

Index (ν)	**MP Delay Interval**	S_ν	N_ν	$\beta_{\nu,2}$	$\beta_{\nu,3}$
1	$[0, 0.1T_c]$	1	2	0.5	0
2	$[0.1T_c, 0.85T_c]$	0	1	0	0
3	$[0.85T_c, 1.05T_c]$	1	2	0.5	0
4	$[1.05T_c, 1.25T_c]$	1	1	0	0
5	$[1.25T_c, 1.4T_c]$	1	2	0.5	0
6	$[1.4T_c, 1.5T_c]$	0	1	0	0

table 4.6: MAA-DLL Lookup Table for $BOC_c(6,1)$ Modulation (Corresponds to Bottom Panel of Figure 4.11)

Index (ν)	**MP Delay Interval**	S_ν	N_ν	$\beta_{\nu,2}$	$\beta_{\nu,3}$
1	$[0, 0.025T_c]$	1	3	0.55	0.047
2	$[0.025T_c, 0.9T_c]$	0	1	0	0
3	$[0.9T_c, 1T_c]$	1	2	0.5	0
4	$[1T_c, 1.5T_c]$	1	1	0	0

are continuously adjusted based on real-time MP delay estimations (as specified in the corresponding tables above). This mechanism enables the MAA-DLL to exhibit a more consistent and controlled discriminator response across the entire spectrum of MP delays, even for the increased complexity of BOC(6,1) signals. By visually presenting these characteristic behaviors, this section illustrates the operational principle of the MAA-DLL's adaptive nature across diverse GNSS signal types.

table 4.7: Design Advantages: MAA-DLL vs. Conventional Approaches

Design Principle	**MAA-DLL**	**Conventional Approaches**
Adaptation	**Dynamic.** Actively reconfigures based on real-time environmental sensing.	**Static.** Employ a single, invariant configuration.
Robustness	**Engineered for Resilience.** Designed to mitigate "worst-case" scenarios.	**Inherently Vulnerable.** Prone to large errors at specific MP delays.
Linearity	**Actively Preserved.** Uses adaptive weighting to cancel MP-induced bias.	**Easily Compromised.** Susceptible to non-linear distortions and bias.
Signal Flexibility	**Highly Versatile.** Easily adapted for various signal types (e.g., BOC, BPSK) via lookup tables.	**Signal-Specific.** Architectures optimized for one signal type perform poorly on others.

Table 4.7 compares the design principles of the proposed MAA-DLL with those of conventional static approaches. It highlights how the MAA-DLL's dynamic and adaptive strategy is engineered to overcome the inherent vulnerabilities common to all fixed-configuration methods, justifying its design for robust performance.

4.4 Result and discussion

To evaluate the MAA-DLL system, two complementary scenarios were developed. The first examines MP mitigation by comparing MAA-DLL with NC, DD, EDD, and SLG across a wide range of signals, including BOC(2,1), BOC(4,1), higher-order BOC(10,5) and BOC(14,2), and MBOC(6,1,1/11). For each case, LOS plus MP realizations are generated with MP delays spanning short, medium, and long regimes, and the corresponding DFs are computed to extract RAE. Results consistently show that MAA-DLL achieves lower RAE values across all MP delays, demonstrating its effectiveness in reducing MP-induced tracking bias.

The second scenario evaluates robustness against combined MP and noise interference using the same correlator structures and signal set. Performance is analyzed at a fixed SNR of –30 dB and over a variable SNR range from –35 dB to –20 dB. Monte Carlo trials are performed to compute the RMSE under each condition, and comparisons are made directly with NC, DD, EDD, and SLG. In all cases, MAA-DLL achieves significantly lower RMSE, confirming its adaptability and resilience in degraded environments.

4.4.1 MP Mitigation Performance

The initial scenario examines the performance of our dynamic selection and weighting method in terms of MP. It compares the method's RAE with the relative MP delay observed in the NC, DD, and EDD schemes, each using three E-L correlator pairs ($N = 3$), as well as with the SLG method. A variety of modulation schemes are considered in all cases. We analyze LOS and single MP signals to derive error envelopes, then examine the DF zero crossings for an MP amplitude of 0.5 over a delay range of 0–450 meters relative to the LOS.

This analysis is performed for BOC(2,1), BOC(4,1), BOC(10,5), BOC(14,2), and MBOC(6,1,1/11) signals, covering the same delay range relative to the LOS. Following the same parameters and methodology consistent with previous research [109, 110], this study adopts an E-L spacing of the $\Delta_1 = 0.1$ chip, with the $\Delta_2 = 1.6\Delta_1$ chip and the $\Delta_3 = 2.5\Delta_1$ chip for the configuration of the paired correlator $N = 3$.

The RAE of the MP signal envelopes are calculated in critical phases, either in phase (0°) or 180° out of phase with the LOS signal, by assessing the absolute envelope values and their cumulative sums. The key parameters used in these simulations are summarized in Table 4.8.

table 4.8: Simulation Parameters

Parameter	**Value/Description**
Proposed Method	MAA-DLL
Comparison Methods	NC, DD, EDD ($N = 3$), SLG
Signal Types	BOCs/c(2,1), BOCs/c(4,1), BOC(10,5), BOC(14,2), and MBOC(6, 1, 1/11)
MP Scenario	Single MP signal ($\|\alpha\| = 0.5$)
Relative MP Delay Range	0 to 450 m (vs. LOS)
MP Phase	0° or 180° (vs. LOS)
E-L Correlator Spacing	$\Delta_1 = 0.1T_c$, $\Delta_2 = 1.6\Delta_1$, $\Delta_3 = 2.5\Delta_1$
Performance Metrics	RAE (Scenario 1) RMSE (Scenario 2)
SNR (RMSE vs. MP delays)	-30 dB
SNR Range (RMSE vs. SNR)	-35 dB to -20 dB

4.4.1.1 Performance with BOCs/c(2,1) Signals

In Figures 4.12 and 4.13, the RAE for BOCs(2,1) and BOCc(2,1) modulated signals is presented for five methods (MAA-DLL, DD, EDD, SLG, and NC). For both signals, the proposed MAA-DLL, based on dynamic selection and weighting, achieves the best RAE.

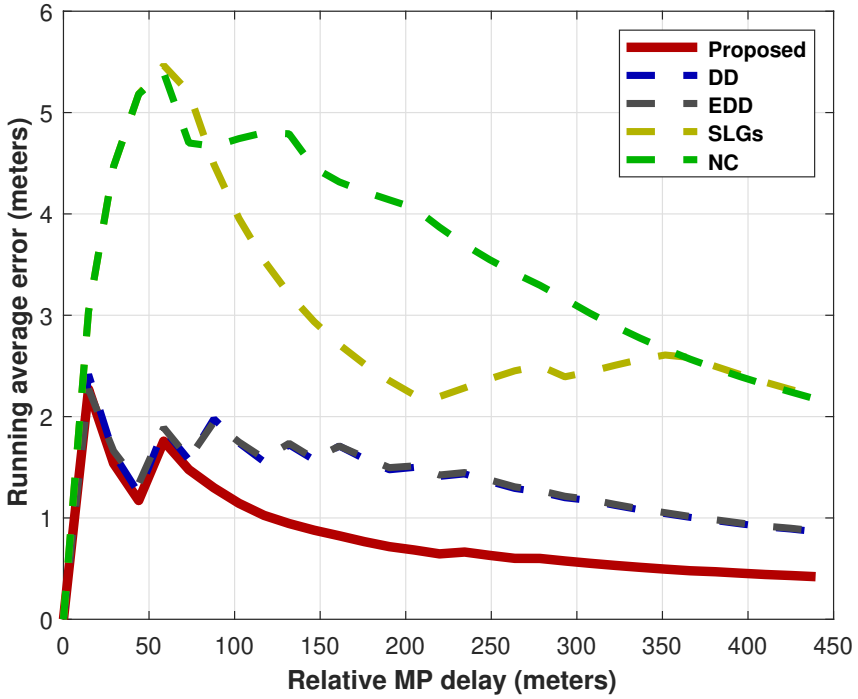

figure 4.12: Running average error comparison versus relative MP delays for NC, DD, EDD (N=3), SLG, and the proposed MAA-DLL method, for BOC$s(2,1)$ modulation schemes.

The advantage is compelling at short relative delays, where the proposed approach

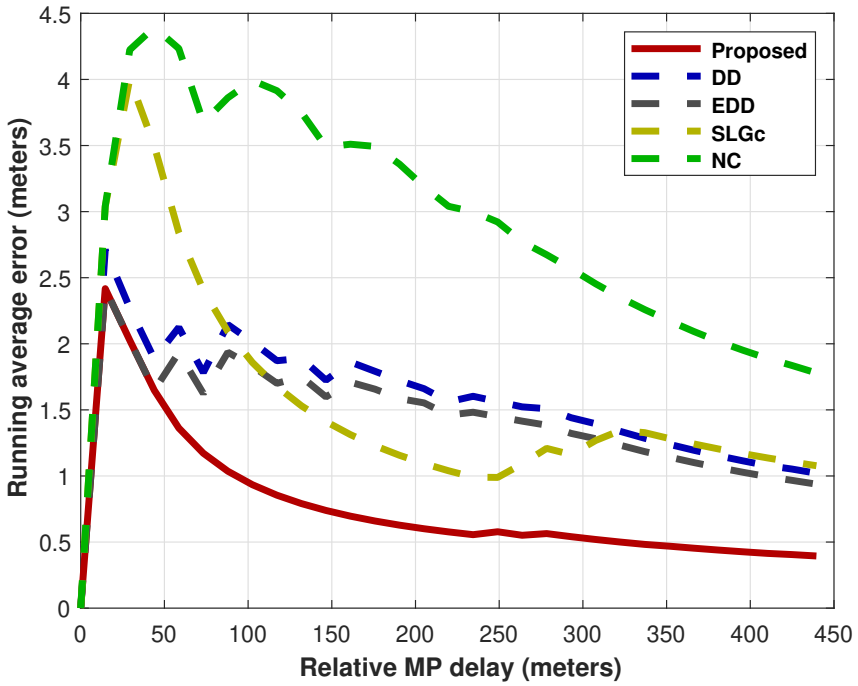

figure 4.13: Running average error comparison versus relative MP delays for NC, DD, EDD (N=3), SLG, and the proposed MAA-DLL method, for BOCc(2, 1) modulation schemes.

removes the first MP-induced distortions more efficiently. Compared to conventional NC, DD, EDD, and SLG methods, its RAE curves decline more rapidly toward zero. This strong performance demonstrates the effectiveness of the adaptive MAA-DLL approach in mitigating MP for the fundamental BOCs/c(2,1) signal across a wide range of MP conditions.

4.4.1.2 Performance with BOCs/c(4,1) Signals

In Figures 4.14 and 4.15, the RAE for the BOCs (4,1) and BOCc (4,1) modulated signals are displayed. For these more advanced BOC modulations, with additional BOC complexity due to more intricate CFs and broader spectral energy distributions, our approach still achieves a minimal RAE for all relative MP delay values.

The plots show that, unlike other techniques, which fail to control errors across all MP delay regions, the proposed MAA-DLL maintains robust performance, even in the medium-to-long delay ranges where most methods struggle to perform effectively.

Its ability to adapt correlator configurations to current MP delay estimates is especially beneficial for BOC(4,1), enabling the MAA-DLL to overcome the processing difficulties these signals present. The strong results obtained with advanced signal models further highlight the efficiency and robustness of the design, demonstrating reliable performance not only with simple BOC signals but also with more complex GNSS signals.

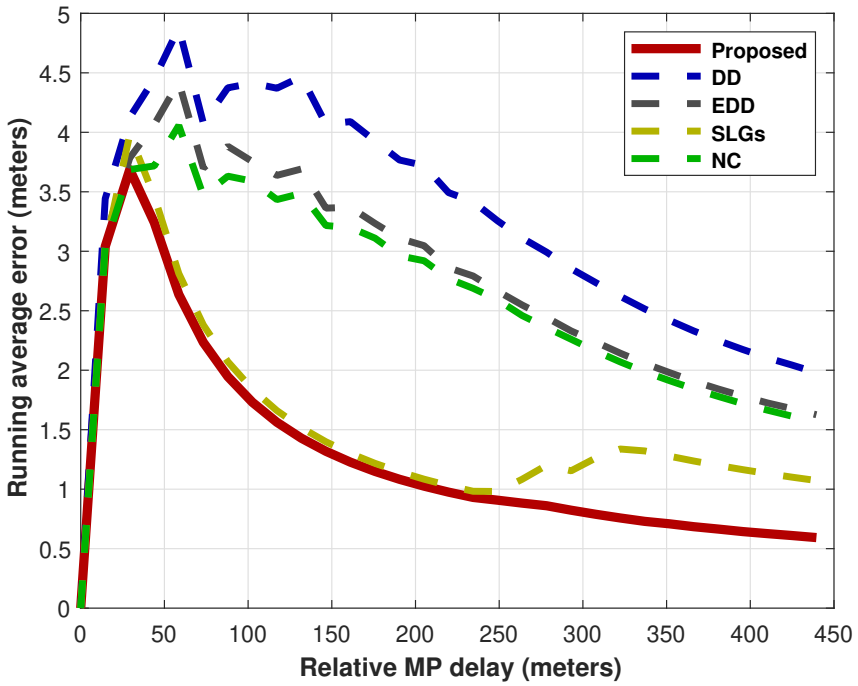

figure 4.14: Running average error comparison versus relative MP delays for NC, DD, EDD (N=3), SLG, and the proposed MAA-DLL method, for BOC$s(4,1)$ modulation schemes.

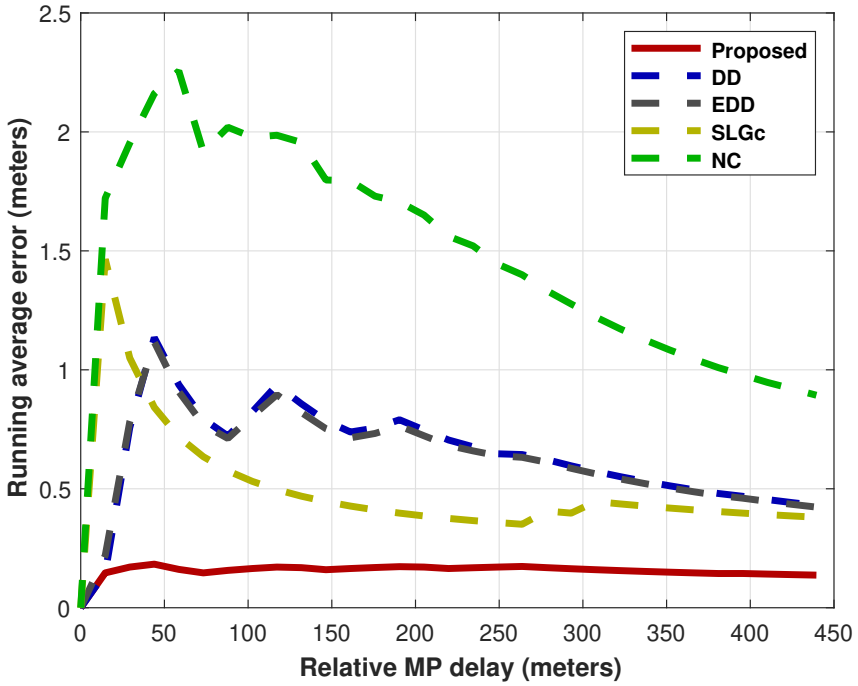

figure 4.15: Running average error comparison versus relative MP delays for NC, DD, EDD (N=3), SLG, and the proposed MAA-DLL method, for BOC$c(4,1)$ modulation schemes.

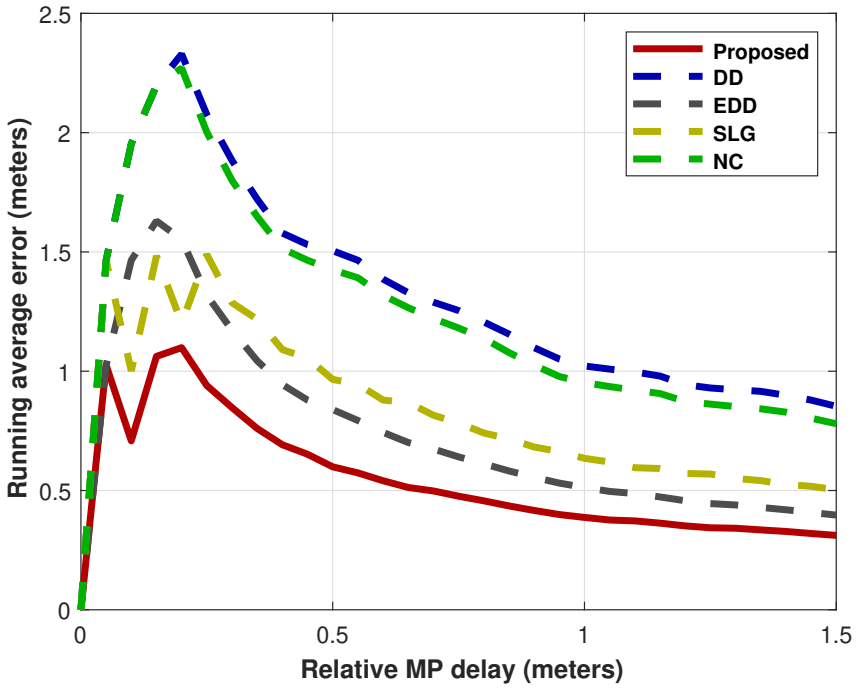

figure 4.16: Running average error comparison versus relative MP delays for NC, DD, EDD (N=3), SLG, and the proposed MAA-DLL method, for BOC(10, 5) modulation schemes.

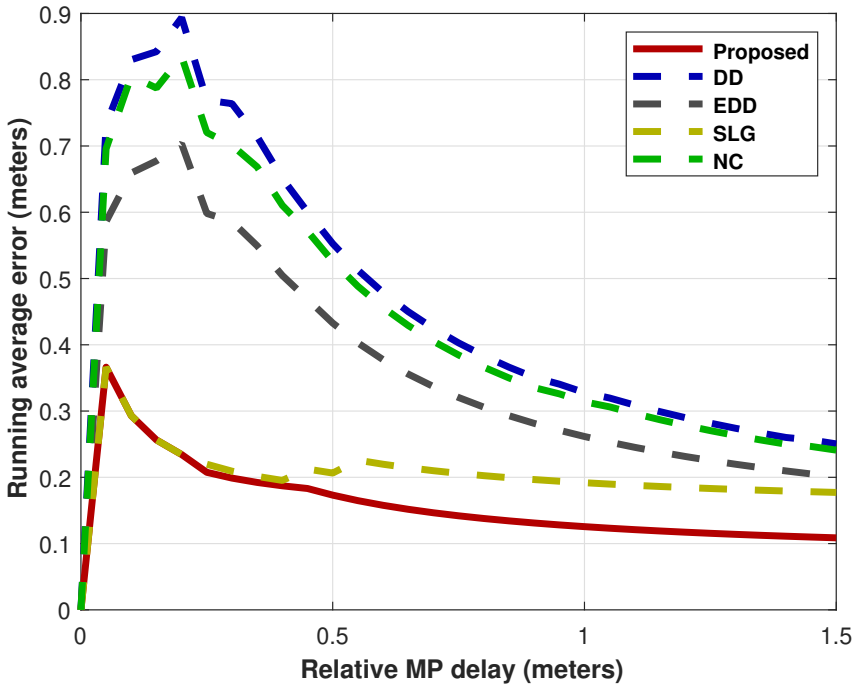

figure 4.17: Running average error comparison versus relative MP delays for NC, DD, EDD (N=3), SLG, and the proposed MAA-DLL method, for BOC(14, 2) modulation schemes.

4.4.1.3 Performance with BOC(10,5) and BOC(14,2) Signals

Figures 4.16 and 4.17 show the RAE for advanced BOC(10,5) and BOC(14,2) signals. This is especially significant given their complex CFs and higher processing demands. The

proposed MAA-DLL maintains low and consistent RAE across all MP delays, avoiding the degradation observed in other techniques.

Conventional methods often suffer from persistent errors and severe degradation in medium- to long-delay regions. By adapting correlator configurations in real time to current MP delays, the MAA-DLL eliminates the need for predefined settings and ensures stable processing. These results confirm the robustness and adaptability of the design, demonstrating reliable performance even with higher-order BOC signals.

4.4.1.4 Performance with MBOC(6, 1,1/11) Signal

The performance of the proposed MAA-DLL was further evaluated using the complex MBOC(6, 1, 1/11) signal, with the results presented in Figure 4.18. The plot demonstrates that the proposed adaptive method consistently achieves the lowest RAE across the entire range of simulated MP delays. While the DD and EDD techniques offer competitive performance, they still exhibit a slightly higher error. However, the conventional NC technique shows significantly poorer performance with a much larger error envelope. This result confirms the effectiveness and robustness of the MAA-DLL's dynamic selection and weighting strategy, even when applied to one of the most complex and modern GNSS signal structures.

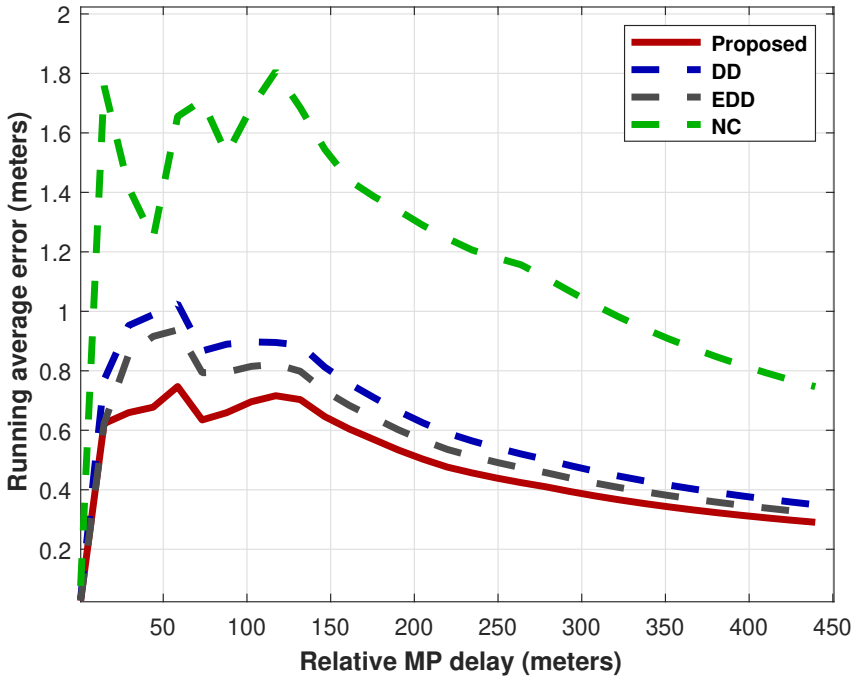

figure 4.18: Running average error comparison versus relative MP delays for NC, DD, EDD (N=3), SLG, and the proposed MAA-DLL method, for MBOC(6, 1,1/11) modulation schemes.

4.4.2 Synergy of MP and Noise Effects

In the second evaluation scenario, a study is conducted to analyze the effect of combined noise with MP interference on the performance of the proposed method. For consistency, all assumptions from the first scenario are maintained, with the SNR held at -30 dB. All previously analyzed structures have been simulated with RMSE as a function of the relative MP delay. Additionally, to provide a more comprehensive performance metric, this analysis was extended to account for varying noise conditions.

The RMSE for each method was also calculated under a range of SNR values -35, -30, -25, and -20 dB. For each of these distinct SNR levels, the RMSE was first evaluated across the full spectrum of relative time delays. The final result is then the mean of these individual RMSE curves, yielding a single, robust value that represents the algorithm's overall performance against the combined effects of both MP and varying noise levels.

4.4.2.1 Performance with BOCs/c(2,1) Signals

Figures 4.19 and 4.20 present the RMSE results for BOCs (2,1) and BOCc (2,1) modulated signals under combined noise and MP. The figures clearly show that the proposed MAA-DLL method significantly outperforms all other approaches across the entire range of MP delay values.

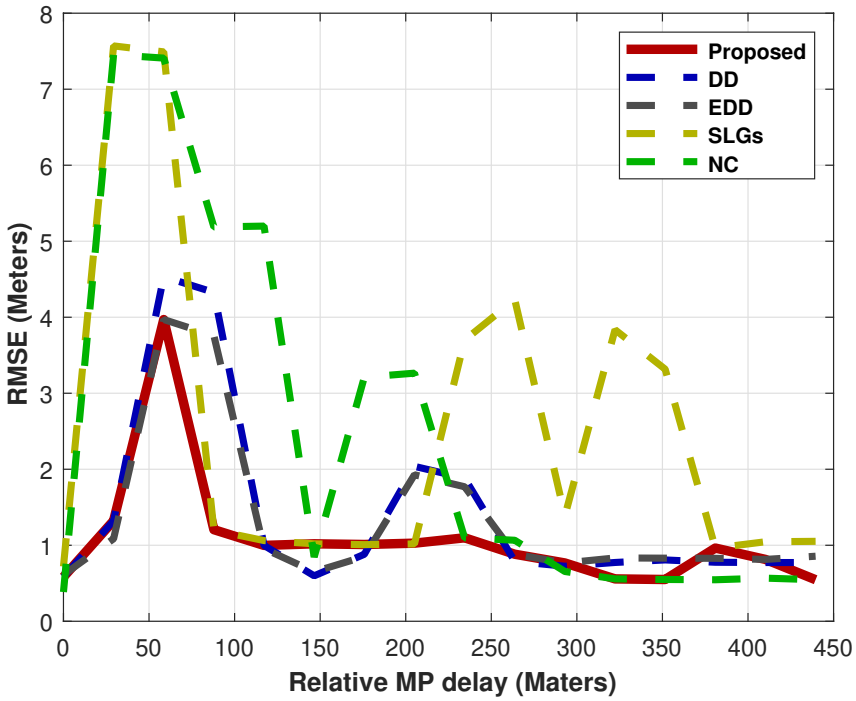

figure 4.19: RMSE comparison versus relative MP delays for NC, DD, EDD (N=3), SLG, and the proposed MAA-DLL method, for BOC$s(2,1)$ modulation schemes.

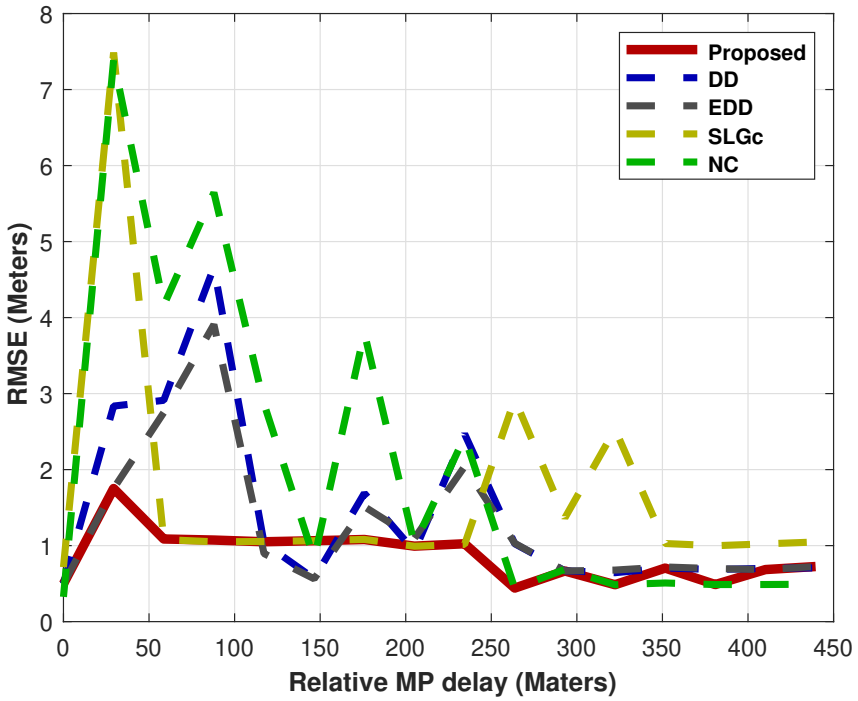

figure 4.20: RMSE comparison versus relative MP delays for NC, DD, EDD (N=3), SLG, and the proposed MAA-DLL method, for BOC$c(2,1)$ modulation schemes.

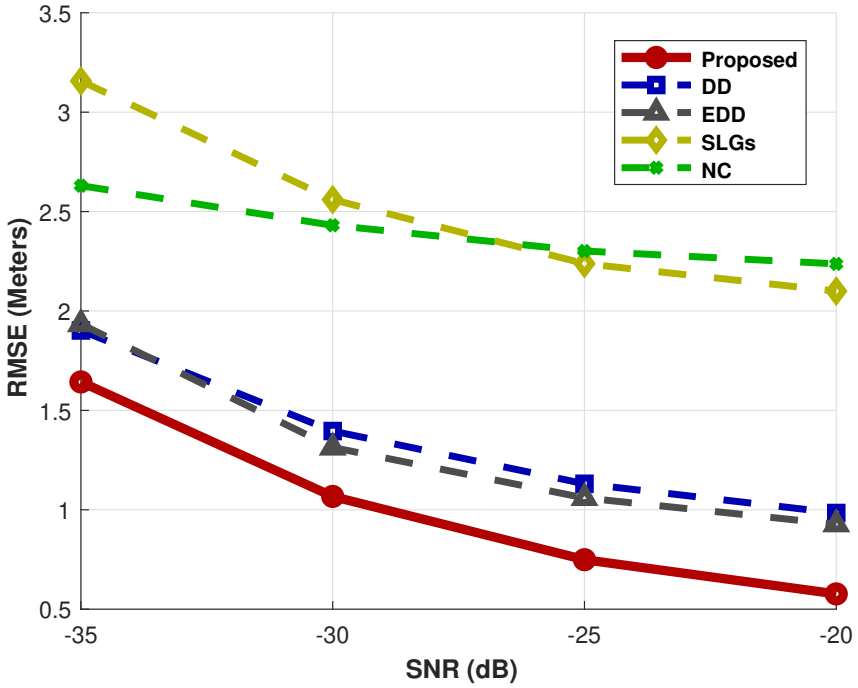

figure 4.21: RMSE comparison versus SNR values for NC, DD, EDD (N=3), SLG, and the proposed MAA-DLL method, for BOC$s(2,1)$ modulation schemes.

The adaptive nature of our MAA-DLL approach has successfully maintained tracking stability and accuracy even in low-SNR environments, demonstrating the fundamental

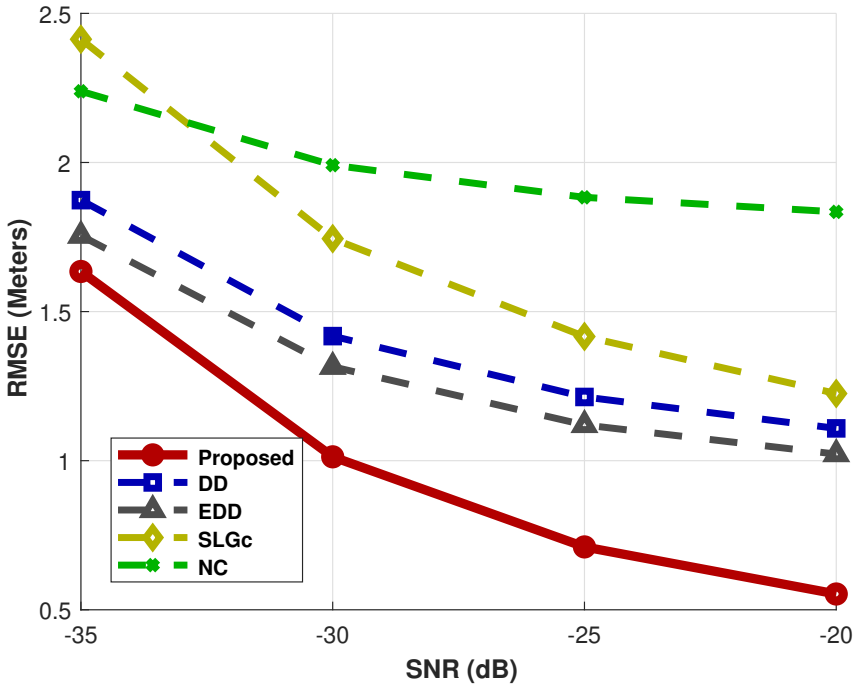

figure 4.22: RMSE comparison versus SNR values for NC, DD, EDD (N=3), SLG, and the proposed dynamic selection and weighting method, for BOC$c(2,1)$ modulation schemes.

resilience of the BOC signal to interference from noise and MP effects. For BOCs/c(2,1) waveforms, the combined effects of noise and MP are suppressed more effectively with our proposed method.

To further illustrate the method's robustness against varying noise levels, Figures 4.21 and 4.22 plot the aggregate RMSE as a function of SNR. The results are remarkable considering the competitive nature of the tracked range MP under substantial noise.

The observation holds in the context of BOC$s(2,1)$ and BOC$c(2,1)$; within the tested SNR range of -35 dB to -20 dB, the proposed method demonstrated the smallest RMSE. The NC, SLG, EDD, and DD approaches to the estimated SNR, in contrast, fall short of providing acceptable reliability. The substantial advantage is attributed to the MAA-DLL design, which adapts to the dynamic MP through the delay, suggesting that the MP and SNR resilient design is capable of effectively withstanding harsh noise environments.

4.4.2.2 Performance with BOCs/c(4,1) Signals

Figures 4.23 and 4.24 present RMSE versus relative MP delays for BOC$s(4,1)$ and BOC$c(4,1)$ under combined noise and MP conditions.

Across all delays, the proposed method outperforms conventional techniques, maintaining the lowest RMSE. This result highlights its robustness against broader spectral distributions and the added complexity of higher-order BOC(4,1) waveforms, further val-

idating the reliability of the MAA-DLL architecture.

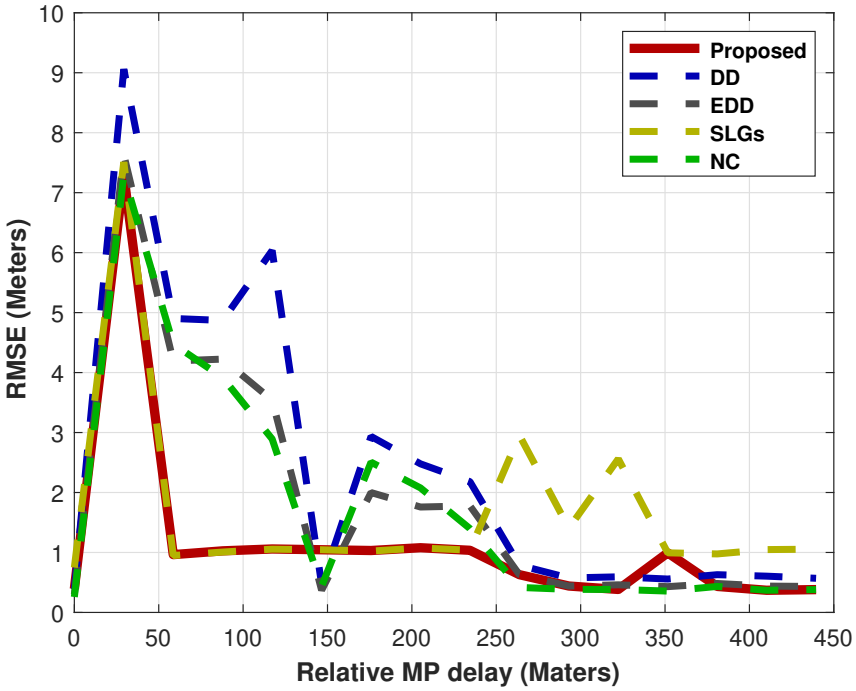

figure 4.23: RMSE comparison versus relative MP delays for NC, DD, EDD (N=3), SLG, and the proposed MAA-DLL method, for BOC$s(4,1)$ modulation schemes.

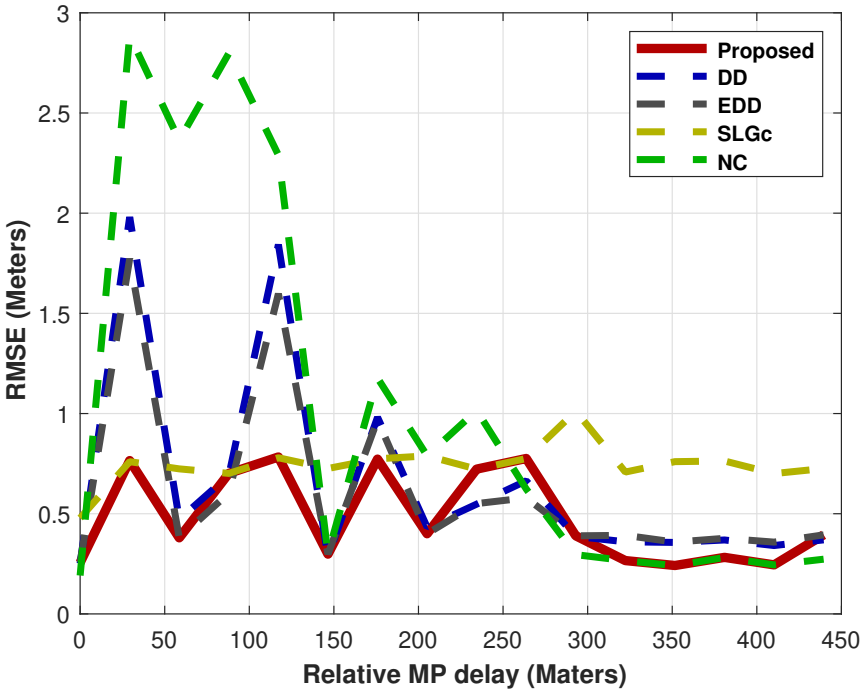

figure 4.24: RMSE comparison versus relative MP delays for NC, DD, EDD (N=3), SLG, and the proposed MAA-DLL method, for BOC$c(4,1)$ modulation schemes.

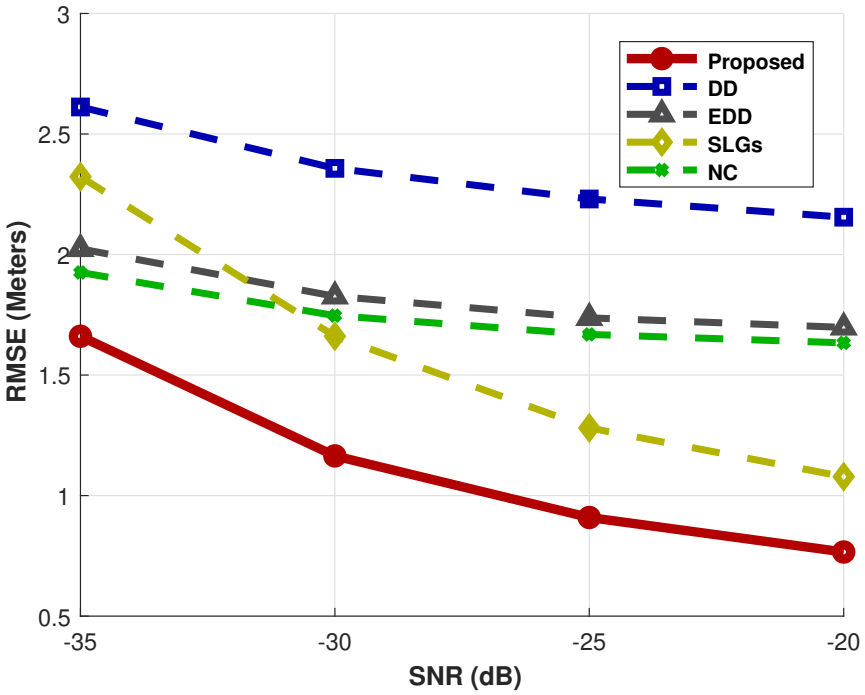

figure 4.25: RMSE comparison versus SNR values for NC, DD, EDD (N=3), SLG, and the proposed MAA-DLL method, for BOCs(4, 1) modulation schemes.

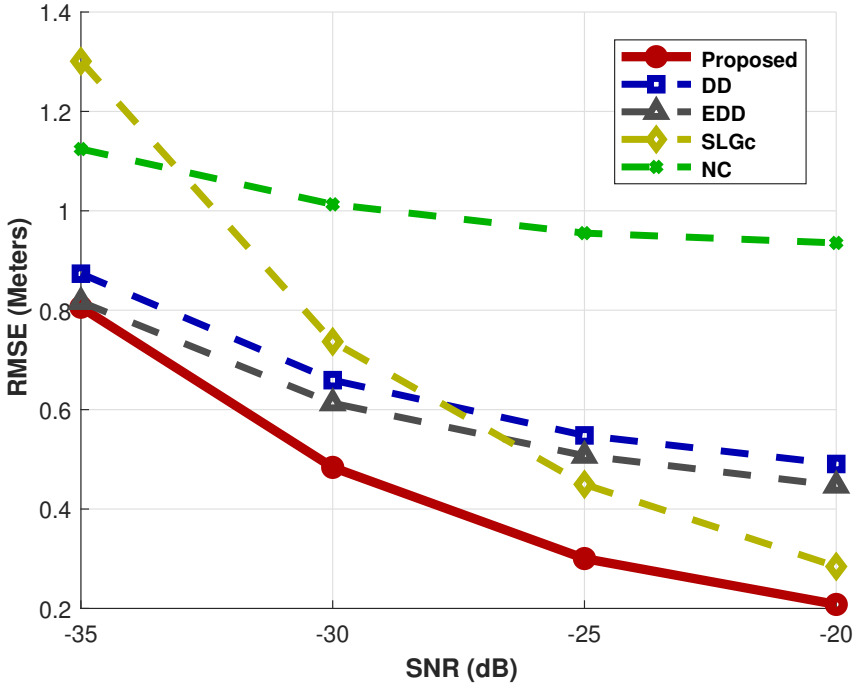

figure 4.26: RMSE comparison versus SNR values for NC, DD, EDD (N=3), SLG, and the proposed MAA-DLL method, for BOCc(4, 1) modulation schemes.

The strength of the MAA-DLL architecture becomes clear when assessing the aggregate RMSE about different SNR levels, particularly for BOCs(4,1) and BOCc(4,1) signals

shown in Figures 4.25 and 4.26. In both instances, the proposed method shows clear advantages, achieving the lowest RMSE in the entire SNR range from -35 dB to -20 dB.

The steadily increasing advantage of the MAA-DLL approach over conventional methods as SNR improves illustrates its effectiveness in MP mitigation, which becomes more pronounced as noise levels decrease. The results further demonstrate the MAA-DLL's adaptability concerning different complex signal modulations and the varying levels of noise and MP interference.

4.4.2.3 Performance with BOC(10,5) and BOC(14,2) Signals

The proposed MAA-DLL method was further evaluated with sine-phased BOC(10,5) and BOC(14,2) signals. Figures 4.27 and 4.28 show the RMSE results as a function of relative MP delay. These higher-order modulations produce chaotic and highly variable tracking errors, as evidenced by the plots.

In contrast, the proposed MAA-DLL maintains a consistently lower error envelope than DD, EDD, SLG, and NC, all of which exhibit large uncontrolled spikes at various MP delays. This demonstrates the superior stability of the adaptive approach when dealing with complex signal structures and higher-order configurations. The results indicate that the method's dynamic correlator adaptation effectively mitigates the erratic behavior of advanced BOC signals, ensuring reliable performance under challenging conditions.

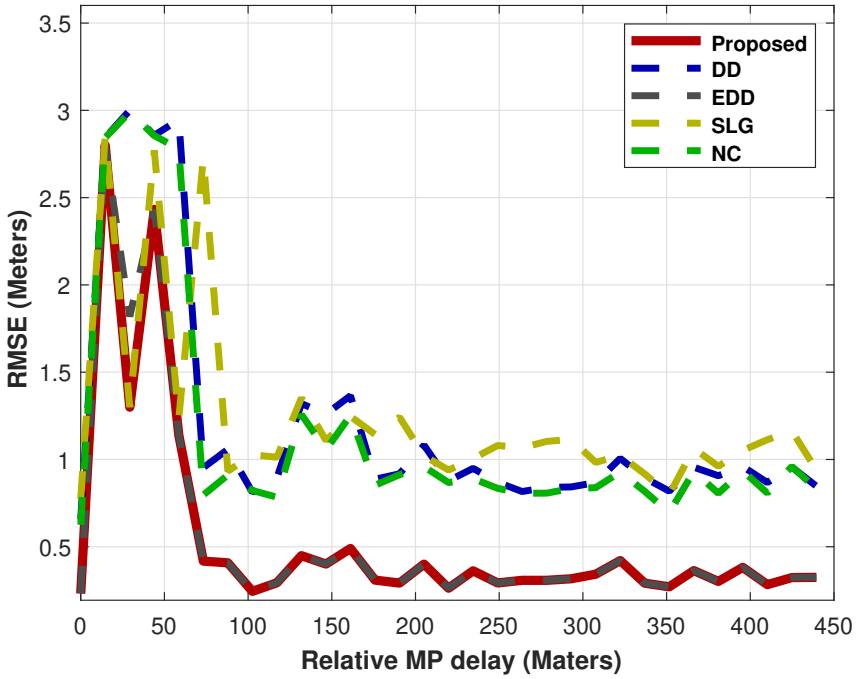

figure 4.27: RMSE comparison versus relative MP delays for NC, DD, EDD (N=3), SLG, and the proposed MAA-DLL method, for BOC(10, 5) modulation schemes.

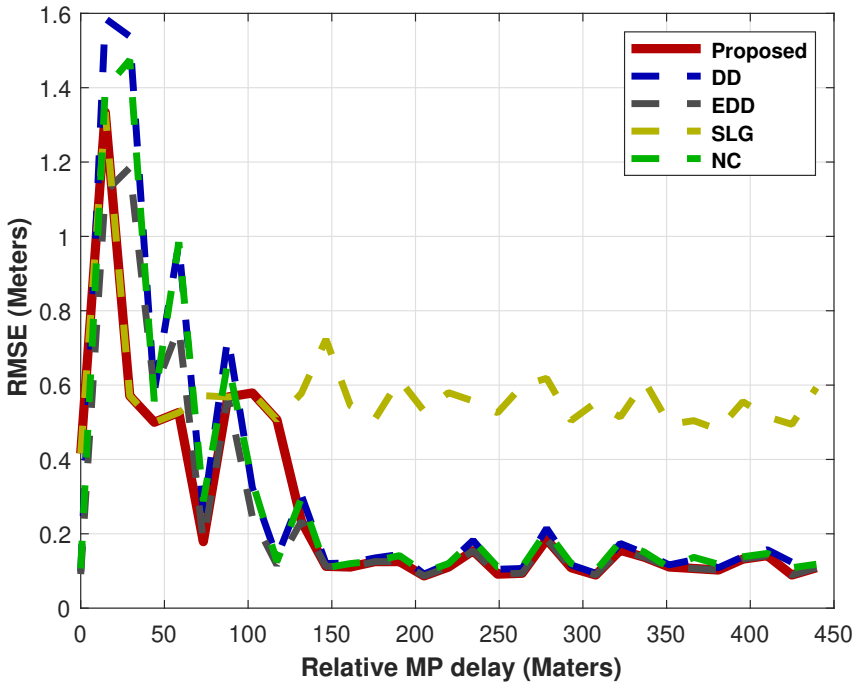

figure 4.28: RMSE comparison versus relative MP delays for NC, DD, EDD (N=3), SLG, and the proposed MAA-DLL method, for BOC(14, 2) modulation schemes.

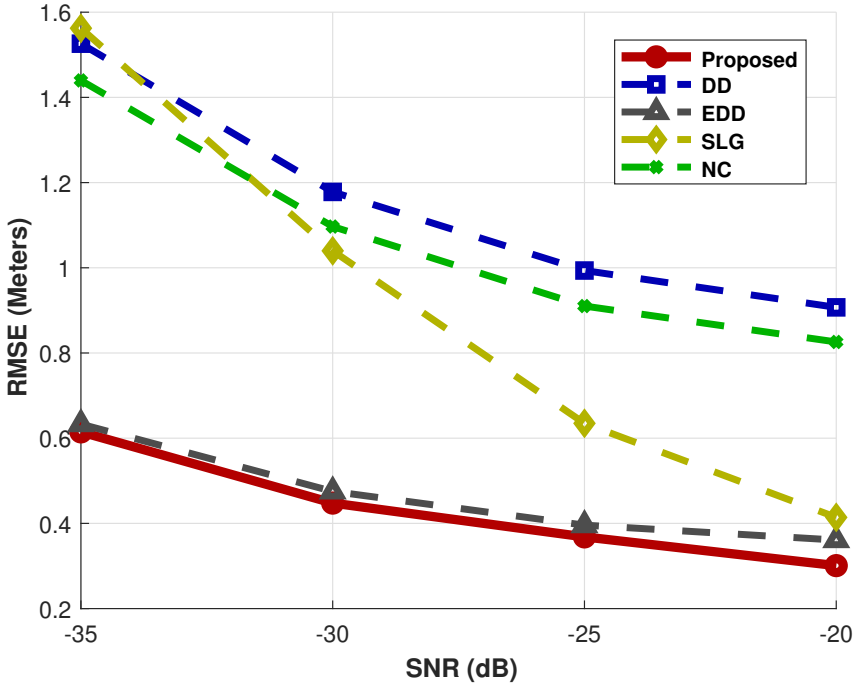

figure 4.29: RMSE comparison versus SNR values for NC, DD, EDD (N=3), SLG, and the proposed MAA-DLL method, for BOC(10, 5) modulation schemes.

As shown for BOC(10,5) and BOC(14,2) in Figures 4.29 and 4.30, the proposed MAA-DLL demonstrates strong robustness to noise, achieving lower RMSE across the full SNR

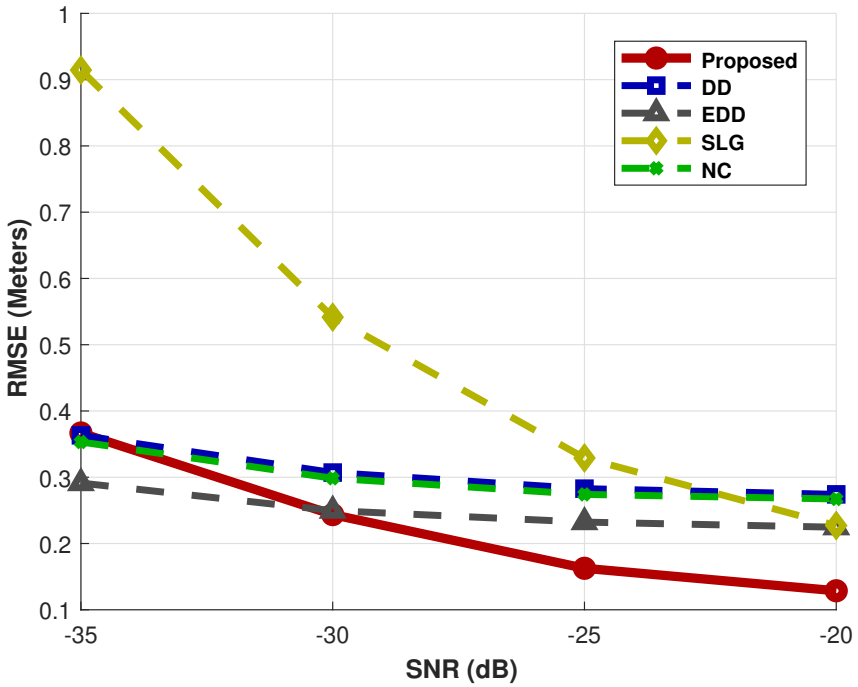

figure 4.30: RMSE comparison versus SNR values for NC, DD, EDD (N=3), SLG, and the proposed MAA-DLL method, for BOC(14, 2) modulation schemes.

range of –35 dB to –20 dB. This performance highlights the effectiveness of its dynamic selection and weighting, which mitigate both noise and MP distortion in higher-order GNSS signals.

4.4.2.4 Performance with MBOC(6, 1,1/11) Signal

The performance of the proposed method was also assessed using the complex MBOC(6, 1, 1/11) signal. The RMSE as a function of relative MP delay is shown in Figure 4.31.

The findings demonstrate that the MAA-DLL mitigates MP interference significantly more effectively than conventional techniques, exhibiting a lower and more stable error profile. This supports the robustness of the adaptive method in tackling MBOC signals, which are considered the most complex and challenging signals to work with for standard tracking loops.

The RMSE was also examined as a function of SNR to assess the variation in noise levels, with the outcomes displayed in Figure 4.32. The previous results are confirmed; the proposed MAA-DLL architecture demonstrates a distinctive and marked improvement, achieving the best RMSE value throughout the entire SNR range tested. This also provides additional evidence for the effectiveness of the selection and weighting dynamics, demonstrating how well it mitigates the compounded noise and MP effects for advanced, complex GNSS signals.

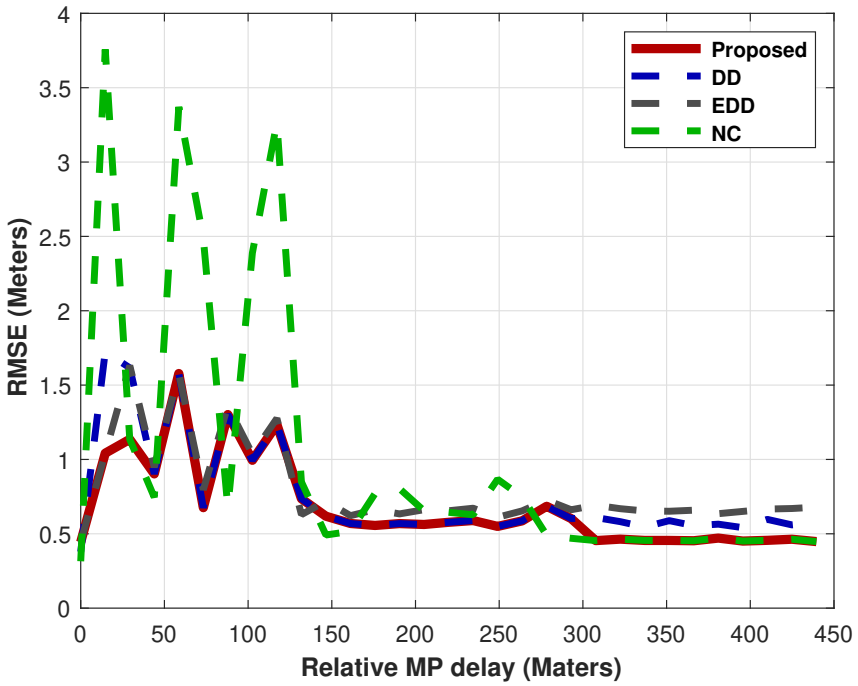

figure 4.31: RMSE comparison versus relative MP delays for NC, DD, EDD (N=3), SLG, and the proposed MAA-DLL method, for MBOC(6, 1,1/11) modulation schemes.

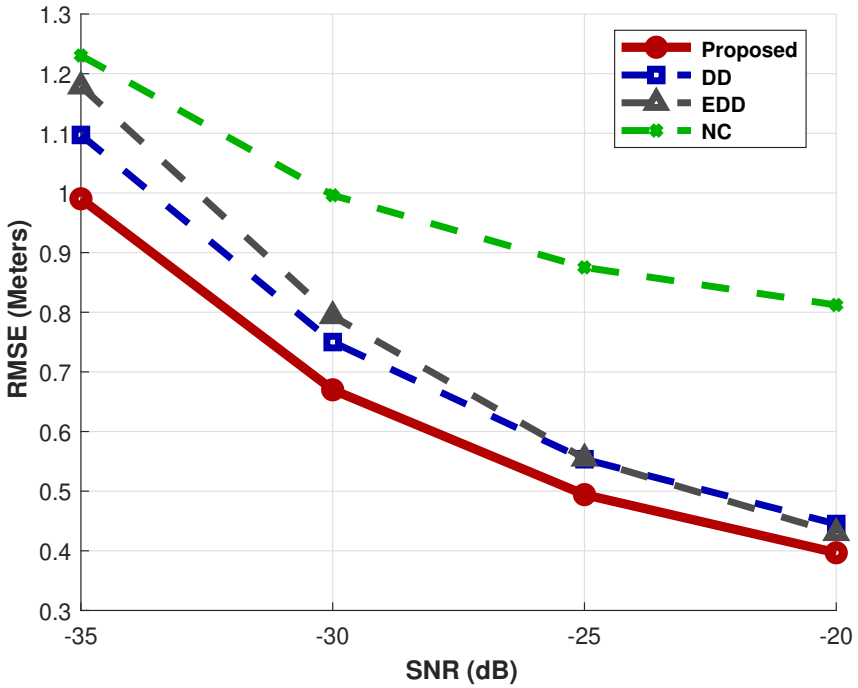

figure 4.32: RMSE comparison versus SNR values for NC, DD, EDD (N=3), SLG, and the proposed MAA-DLL method, for MBOC(6, 1,1/11) modulation schemes.

4.5 Conclusion

This chapter begins with a thorough analysis of the severe effects of MP on DFs and the disadvantages of fixed-weighting correlator techniques. To address these established challenges, this chapter proposes a new advanced MAA-DLL architecture designed to improve the tracking accuracy of GNSS and PL signals in difficult MP conditions.

The proposed MAA-DLL operates in two stages: a code phase refinement stage for accurate MP delay estimation and an adaptive DLL reconfiguration stage. This second stage dynamically selects optimal E-L correlator pairs and their corresponding weights using an empirically optimized lookup table. The continuous refinement of the DF features enhances the linearity and decreases the susceptibility of the DF parameters to linearity distortion.

Comprehensive simulations confirm that the MAA-DLL architecture consistently outperforms conventional techniques, such as NC, DD, EDD, and SLG. When tested against a wide range of complex signals, including higher-order BOC and MBOC, the architecture achieved the lowest RAE and RMSE values across all simulated MP delays and a challenging SNR range of -35 dB to -20 dB. This success, particularly with complex modulations, validates the MAA-DLL's robust and adaptable design, marking it as a promising solution for high-precision positioning in next-generation navigation systems.

General Conclusion

This thesis presents an exhaustive and comprehensive investigation into enhancing receivers' trustworthiness and positioning precision using GNSS and PL systems, with a particular interest in the performance of the THMA technique in unfavorable environments and a focus on mitigating the undesirable impacts of MP interference. First, it establishes the fundamental principles and architectures of the GNSS and PL positioning systems, examining the near-far problem in PLs and the various error sources that affect their performance. Subsequently, the thesis delves into the significant domain of signal design, offering an in-depth description of the GNSS signal (DSSS, PSD, ACF) and various modulation structures (BPSK, BOC, MBOC, BSC), outlining their main properties, and presenting a comparative assessment. In addition, it covers THMA as a mitigation strategy for the near–far problem in PL systems, describing the TH-pulsed signal structure, SIT generation, and associated statistical properties.

The thesis continues with an in-depth presentation of receiver signal processing strategies and acquisition techniques, including serial and parallel search methods, the zero-padding strategy to address data bit-transit issues, and tracking loops. This section concludes with a detailed investigation of MP effects on THMA signals, showing that its impact appears as distortions in the signal's initial phase, which can be separated into integral and fractional parts. The integral component reflects the number of timeslots in the initial phase, whereas the fractional component corresponds to the PRN code phase of the DSSS portion, representing the sub-timeslot delay of the received signal. In the integral part, the CF computed between the received signal and the local replica produces two peaks, representing the LOS and MP components; merging the MP peak with the LOS peak in the CF enables partial mitigation of MP effects. However, residual distortions in the fractional domain remain complex and demand advanced baseband MP mitigation techniques similar to those used in standard GNSS signals.

Following this investigation, the discussion provides an overview of existing baseband mitigation strategies together with their discriminator architectures and operating principles, such as NC, DD, EDD, and SLG. However, these methods offer only partial so-

lutions, as their fixed weighting schemes and correlator structures cannot adapt to the time-varying behavior of MP across different delays and modulation types. Consequently, distortions in the DLL-DF persist, leading to code-tracking biases such as zero-crossing shifts and linear range reduction, which degrade tracking accuracy and emphasize the need for more adaptive receiver architectures.

Building on this comprehensive foundation, the thesis addresses the limitations of conventional fixed DLL configurations by introducing the MAA-DLL architecture, an efficient mitigation method based on dynamic selection and adaptive weighting of E-L correlators. The MAA-DLL operates in two main stages: a precise code phase stage to refine MP delay estimation, and an adaptive DLL configuration stage. In the latter, the most suitable E-L correlator pairs and their weightings are selected using an optimized look-up table with empirically determined constants, continuously optimizing the DLL-DF for maximum linearity and minimal MP susceptibility.

The extensive simulation results presented in this thesis consistently validated the superior performance of the proposed MAA-DLL architecture. Its performance was rigorously evaluated against a comprehensive set of modern GNSS signals, including BOC (2,1), BOC (4,1), higher order BOC (10,5) and BOC (14.2), and complex MBOC (6, 1, 1/11). Across all these modulations, MAA-DLL demonstrated a significant advantage over conventional methods (NC, DD, EDD, and SLG). It achieved the lowest RAE against MP delay and maintained the lowest RMSE under the combined effects of MP and varying noise, both at a fixed -30 dB SNR and across a dynamic SNR range of -35 dB to -20 dB. These results demonstrate the excellent adaptability of the MAA-DLL under varying MP conditions and its venerability to various structures within GNSS/PL signals.

The proposed framework, which features an easy-to-implement design compatible with traditional receiver structures, introduces a robust adaptive mitigation strategy for civilian and military GNSS and PL receivers. Using real-time MP delay estimates, the MAA-DLL significantly enhances tracking accuracy and resilience under challenging navigation conditions, marking a valuable contribution to next-generation PNT applications.

Future work may extend the MAA-DLL framework to multi-frequency and multi-constellation GNSS/PL signals, incorporate machine learning for real-time multifunctional processor classification and adaptive tuning, and examine baseband with antenna-level techniques of hybrid mitigation to improve positioning accuracy and robustness.

Bibliography

[1] Basudeb Bhatta. *Global navigation satellite systems: new technologies and applications*. CRC Press, 2021.

[2] Irwan Gumilar, Ridhwan A Mahdiyanto, Brian Bramanto, Wedyanto Kuntjoro, and Hasanuddin Z Abidin. Study of gnss multi-constellation performance in single point positioning and differential positioning in indonesia. *J Aeronaut Astronaut Aviat Ser*, 54:195–213, 2022.

[3] Tong Liu, Jian Liu, Jing Wang, Heng Zhang, Bing Zhang, Yongchao Ma, Mengfei Sun, Zhiping Lv, and Guochang Xu. Pseudolites to support location services in smart cities: Review and prospects. *Smart Cities*, 6(4):2081–2105, 2023.

[4] Enkhtuvshin Boldbaatar, Donald Grant, Suelynn Choy, Safoora Zaminpardaz, and Lucas Holden. Evaluating optical clock performance for gnss positioning. *Sensors*, 23(13):5998, 2023.

[5] James Bao-Yen Tsui. *Fundamentals of global positioning system receivers: a software approach*. John Wiley & Sons, 2004.

[6] Yi Hu, Baoguo Yu, Maozhong Song, and Zhixin Deng. Pulse position detection of the pseudo random time-hopping pseudolite for the participative gnss receivers. *IEEE Access*, 8:216151–216161, 2020.

[7] Chongwon Kim, Hyoungmin So, Taikjin Lee, and Changdon Kee. A pseudolite-based positioning system for legacy gnss receivers. *Sensors*, 14(4):6104–6123, 2014.

[8] Yi Hu, Baoguo Yu, Zhixin Deng, and Wenjuan Yu. Generation of slot index tables for time-hopping pseudolites with the constructed congruence codes. *Radioengineering*, 32(1):113–123, 2023.

[9] H Stewart Cobb. *GPS pseudolites: Theory, design, and applications*. Stanford University, 1997.

[10] Yury V Yasyukevich, Alexander V Kiselev, Ilya V Zhivetiev, Ilya K Edemskiy, Semen V Syrovatskii, Boris M Maletckii, and Artem M Vesnin. Simurg: System for ionosphere monitoring and research from gnss. *GPS solutions*, 24:1–12, 2020.

[11] Ningbo Wang, Yunbin Yuan, Zishen Li, and Xingliang Huo. Improvement of klobuchar model for gnss single-frequency ionospheric delay corrections. *Advances in Space Research*, 57(7):1555–1569, 2016.

[12] Hongyang Ma, Dimitrios Psychas, Xuhuang Xing, Qile Zhao, Sandra Verhagen, and Xianglin Liu. Influence of the inhomogeneous troposphere on gnss positioning and integer ambiguity resolution. *Advances in Space Research*, 67(6):1914–1928, 2021.

[13] Xu Liu, Zheng Yao, and Mingquan Lu. Robust time-hopping pseudolite signal acquisition method based on dynamic bayesian network. *GPS Solutions*, 25:1–14, 2021.

[14] Jacek Januszewski. Sources of error in satellite navigation positioning. *TransNav: International Journal on Marine Navigation and Safety of Sea Transportation*, 11(3), 2017.

[15] Elliott D Kaplan and Christopher Hegarty. *Understanding GPS/GNSS: principles and applications*. Artech house, 2017.

[16] Bernhard Hofmann-Wellenhof, Herbert Lichtenegger, and Elmar Wasle. *GNSS—global navigation satellite systems: GPS, GLONASS, Galileo, and more*. Springer, 2008.

[17] Michael S Braasch. Performance comparison of multipath mitigating receiver architectures. In *2001 IEEE Aerospace Conference Proceedings (Cat. No. 01TH8542)*, volume 3, pages 3–1309. IEEE, 2001.

[18] Peng Xie and Mark G Petovello. Measuring gnss multipath distributions in urban canyon environments. *IEEE Transactions on Instrumentation and Measurement*, 64(2):366–377, 2014.

[19] Ayoub Bengherabi, Mustapha Flissi, Khaled Rouabah, Salim Attia, Diana W. Dawoud, Yassine Himeur, Shadi Atalla, and Wathiq Mansoor. Efficient multipath mitigation in gnss using dynamic selection and weighting of early-late correlators. *IEEE Access*, 13:110736–110751, 2025.

[20] John W Betz. Binary offset carrier modulations for radionavigation. *Navigation*, 48(4):227–246, 2001.

[21] Salim Attia, Khaled Rouabah, Djamel Chikouche, and Mustapha Flissi. Side peak cancellation method for sine-boc (m, n)-modulated gnss signals. *EURASIP Journal on Wireless Communications and Networking*, 2014:1–14, 2014.

[22] Yuanfa Ji, Ying Zhang, Xiyan Sun, Xizi Jia, and Jingjing Li. Enhanced synchronization algorithms for boc signals based on reconstructed sub-correlation functions. *Electronics*, 12(13):2839, 2023.

[23] Guenter W Hein, Jose-Angel Avila-Rodriguez, Stefan Wallner, Anthony R Pratt, John Owen, Jean-Luc Issler, John W Betz, Chris J Hegarty, Sean Lenahan, Joseph J Rushanan, et al. Mboc: the new optimized spreading modulation recommended for galileo l1 os and gps l1c. In *Proceedings of IEEE/ION PLANS 2006*, pages 883–892, 2006.

[24] JOSE-ANGEL AVILA-RODRIGUEZ, Guenter W Hein, Stefan Wallner, JEAN-LUC ISSLER, Lionel Ries, Laurent Lestarquit, ANTOINE de LATOUR, Jeremie Godet, Frederic Bastide, Tony Pratt, et al. The mboc modulation: the final touch to the galileo frequency and signal plan. *Navigation*, 55(1):15–28, 2008.

[25] Chris Hegarty, John W Betz, and Ali Saidi. Binary coded symbol modulations for gnss. In *Proceedings of the 60th Annual Meeting of The Institute of Navigation (2004)*, pages 56–64, 2004.

[26] VectorNav Technologies. Theory of operation: Gnss. Online Primer, 2025. Part of the Inertial Navigation Primer.

[27] Bernhard Hofmann-Wellenhof, Herbert Lichtenegger, and James Collins. *Global positioning system: theory and practice*. Springer Science & Business Media, 2012.

[28] Peter JG Teunissen, Oliver Montenbruck, et al. *Springer handbook of global navigation satellite systems*, volume 10. Springer, 2017.

[29] Asghar T Balaei, Andrew G Dempster, and Joel Barnes. A novel approach in detection and characterization of cw interference of gps signal using receiver estimation of c/no. In *Proceedings of IEEE/ION PLANS 2006*, pages 1120–1126, 2006.

[30] Xiang Huo, Xue Wang, Sen Wang, Xiaofei Chen, Ganghua Zhou, and Xiaochun Lu. Receiving and assessing l1c signal for in-orbit gps iii and qzss transmissions using a software-defined receiver. *Electronics*, 9(1):11, 2019.

[31] Karl Kovach, Jason Taylor, Andrew Elliott, and David Steare. The precise positioning service (pps) performance standard (ps). In *Proceedings of the 20th International Technical Meeting of the Satellite Division of The Institute of Navigation (ION GNSS 2007)*, pages 2529–2540, 2007.

[32] Brent A Renfro, Miquela Stein, Nicholas Boeker, and Audric Terry. An analysis of global positioning system (gps) standard positioning service (sps) performance for 2017. *See https://www. gps. gov/systems/gps/performance/2014-GPS-SPS-performance-analysis. pdf*, 2018.

[33] Richard D Fontana, Wai Cheung, and Tom Stansell. The modernized l2 civil signal. *GPS world*, 12(9):28–35, 2001.

[34] Sana U Qaisar, Craig Benson, and Michael J Ryan. A novel efficient signal processing approach for combined acquisition of gps l1 and l2 civilian signals. In *2016 Military Communications and Information Systems Conference (MilCIS)*, pages 1–5. IEEE, 2016.

[35] Tung Hai Ta, Marco Pini, and Letizia Lo Presti. Combined gps l1c/a and l2c signal acquisition architectures leveraging differential combination. *IEEE Transactions on Aerospace and Electronic Systems*, 50(4):3212–3229, 2014.

[36] Xingxing Li, Maorong Ge, Xiaolei Dai, Xiaodong Ren, Mathias Fritsche, Jens Wickert, and Harald Schuh. Accuracy and reliability of multi-gnss real-time precise positioning: Gps, glonass, beidou, and galileo. *Journal of geodesy*, 89(6):607–635, 2015.

[37] Yuri Urlichich, Valery Subbotin, Grigory Stupak, Vyacheslav Dvorkin, Alexander Povalyaev, and Sergey Karutin. Glonass modernization. In *Proceedings of the 24th International Technical Meeting of the Satellite Division of The Institute of Navigation (ION GNSS 2011)*, pages 3125–3128, 2011.

[38] M Zahidul H Bhuiyan, Salomon Honkala, Stefan Söderholm, and Heidi Kuusniemi. Glonass l1of receiver processing. *GNSS software receivers*, 126:139, 2022.

[39] Andreas Lewandowski, Brian Niehoefer, and Christian Wietfeld. Galileo/sar: Performance aspects and new service capabilities. *International Journal of Satellite Communications and Networking*, 29(5):441–460, 2011.

[40] Maxime Fontanier, Hélène Ruiz, and Chiara Scaleggi. Return link service provider (rlsp) acknowledgement service to confirm the detection and localization of the sar

galileo alerts. *Space Operations: Inspiring Humankind's Future*, pages 393–411, 2019.

[41] Guenter W Hein and José Ángel Ávila-Rodríguez. Performance of a galileo prs/gps m-code combined service. In *Proceedings of the 2005 National Technical Meeting of The Institute of Navigation*, pages 754–768, 2005.

[42] Seunghwan Kim, Nicolas Gault, Yongrae Jo, Hyosang Yoon, Byungwoon Park, Axel Garcia-Pena, Christophe Macabiau, and Dennis M Akos. Gnss l5/e5a code properties in the presence of a blanker. *NAVIGATION: Journal of the Institute of Navigation*, 72(2), 2025.

[43] Yuanxi Yang, Weiguang Gao, Shuren Guo, Yue Mao, and Yufei Yang. Introduction to beidou-3 navigation satellite system. *Navigation*, 66(1):7–18, 2019.

[44] Rui Li, Shuaiyong Zheng, Ershen Wang, Jinping Chen, Shaojun Feng, Dun Wang, and Liwen Dai. Advances in beidou navigation satellite system (bds) and satellite navigation augmentation technologies. *Satellite Navigation*, 1:1–23, 2020.

[45] S Sarkar. A study on compatibility and interoperability among multi-gnss. *AAOAJ*, 5:25–31, 2021.

[46] Jacek Januszewski. Compatibility and interoperability of satellite navigation systems in different modes of transport. *Prace Naukowe Politechniki Warszawskiej*, 95:199–208, 2013.

[47] James J Miller, Frank H Bauer, AJ Oria, Scott Pace, and Joel JK Parker. Achieving gnss compatibility and interoperability to support space users. In *Proceedings of the 29th International Technical Meeting of The Satellite Division of the Institute of Navigation (ION GNSS+ 2016)*, pages 3622–3634, 2016.

[48] P Kovar, P Kacmarik, and F Vejrazka. Interoperable gps, glonass and galileo software receiver. *IEEE Aerospace and Electronic Systems Magazine*, 26(4):24–30, 2011.

[49] Eltehs SIA Company. L1, l2, l5, l3, and simply l frequency bands. https://gnss.store/blog/post/l1-l2-l5-l3-and-simply-l-frequency-bands.html, April 2023. Accessed: 2025-07-21.

[50] J Januszewski. Compatibility and interoperability of satellite navigation systems. In *11th International Conference "Computer Systems Aided Science, Industry and Transport", TransComp*, volume 1, pages 289–294, 2007.

[51] Panpan Huang. *Airborne GNSS PPP Based Pseudolite System.* PhD thesis, UNSW Sydney, 2019.

[52] Constantina Isaia and Michalis P Michaelides. A review of wireless positioning techniques and technologies: From smart sensors to 6g. *Signals*, 4(1):90–136, 2023.

[53] Padma Bolla and Kai Borre. Performance analysis of dual-frequency receiver using combinations of gps l1, l5, and l2 civil signals. *Journal of Geodesy*, 93:437–447, 2019.

[54] Bradfrod W Parkinson. Global positioningb system: Theory and applications. *Progress in Astronautics and Aeronautics Series*, pages 547–568, 1996.

[55] Shuanggen Jin, Giovanni Occhipinti, and Rui Jin. Gnss ionospheric seismology: Recent observation evidences and characteristics. *Earth-Science Reviews*, 147:54–64, 2015.

[56] Lei Yang, Zeynep Elmas, Chris Hill, Marcio Aquino, and Terry Moore. An innovative approach for atmospheric error mitigation using new gnss signals. *The Journal of Navigation*, 64(S1):S211–S232, 2011.

[57] Kaifei He, Tianhe Xu, Christoph Förste, Zhenjie Wang, Qiang Zhao, and Yongseng Wei. A method to correct the raw doppler observations for gnss velocity determination. In *Beyond 100: The Next Century in Geodesy: Proceedings of the IAG General Assembly, Montreal, Canada, July 8-18, 2019*, pages 129–134. Springer, 2020.

[58] J. Wu, X. Tang, Z. Li, C. Li, and F. Wang. Cascaded interference and multipath suppression method using array antenna for GNSS receiver. *IEEE Access*, 7:69274–69282, 2019.

[59] H. Xu, A. Angrisano, S. Gaglione, and L.-T. Hsu. Machine learning based LOS/NLOS classifier and robust estimator for GNSS shadow matching. *Satellite Navig.*, 1:1–12, 2020.

[60] Lin Chen, Yuqi Liu, and Shaobin Guo. Method for gnss signal. In *China Satellite Navigation Conference (CSNC) 2020 Proceedings: Volume I*, volume 650, page 466. Springer Nature, 2020.

[61] Andrea Goldsmith. *Wireless communications.* Cambridge university press, 2005.

[62] Christopher J Hegarty. Gnss signals—an overview. In *2012 IEEE International Frequency Control Symposium Proceedings*, pages 1–7. IEEE, 2012.

[63] Supraja Reddy Ammana, Komal Kumar Songala, and Divya Bollavula. Performance evaluation of weil codes and gold codes for application in future navigation signals. In *2022 IEEE 2nd Mysore Sub Section International Conference (MysuruCon)*, pages 1–6. IEEE, 2022.

[64] Gangsan Kim, Hong-Yeop Song, and Deok Won Lim. Some constructions of truncated gold codes for gnss. In *2019 International Conference on Information and Communication Technology Convergence (ICTC)*, pages 1231–1233. IEEE, 2019.

[65] Priyanka Das, Lorenzo Ortega, Jordi Vilà-Valls, François Vincent, Eric Chaumette, and Loïc Davain. Performance limits of gnss code-based precise positioning: Gps, galileo & meta-signals. *Sensors*, 20(8):2196, 2020.

[66] Lorenzo Ortega, Jordi Vilà-Valls, Eric Chaumette, and François Vincent. On the time-delay estimation accuracy limit of gnss meta-signals. In *2020 IEEE 23rd International Conference on Intelligent Transportation Systems (ITSC)*, pages 1–6. IEEE, 2020.

[67] Chuanjun Hu, Tinghui Li, and Feijiang Huang. The design and implementation of gps ca code simulation experiment. In *IOP Conference Series: Materials Science and Engineering*, volume 768, page 062080. IOP Publishing, 2020.

[68] Christopher J Hegarty. A simple model for gps c/a-code self-interference. *NAVIGATION: Journal of the Institute of Navigation*, 67(2):319–331, 2020.

[69] Haochen Liu. Bpsk/boc modulation signal system for gps satellite navigation signals. In *Journal of Physics: Conference Series*, volume 2384, page 012023. IOP Publishing, 2022.

[70] Xu Yang, Wenquan Feng, Chen Zhuang, Qiang Wang, Xu Yang, and Zhe Yang. A multi-correlation peak phase deblurring algorithm for beidou b1c signals in urban environments. *Remote Sensing*, 15(17):4300, 2023.

[71] Jiangang Ma, Yikang Yang, Hengnian Li, and Jisheng Li. Expressions for the autocorrelation function and power spectral density of boc modulation based on convolution operation. *Mathematical Problems in Engineering*, 2020(1):2063563, 2020.

[72] Olivier Julien, Christophe Macabiau, J-A Avila Rodriguez, Stefan Wallner, Matteo Paonni, Guenter W Hein, J-L Issler, and Lionel Ries. On potential cboc/tmboc common receiver architectures. In *Proceedings of the 20th International Technical*

Meeting of the Satellite Division of The Institute of Navigation (ION GNSS 2007), pages 1530–1542, 2007.

[73] GPS Navstar. Space segment/user segment l1c interfaces, interface specification. Technical report, Draft IS-GPS-800, 2006.

[74] Myriam Foucras, Bertrand Ekambi, Fayaz Bacard, Olivier Julien, and Christophe Macabiau. Optimal gnss acquisition parameters when considering bit transitions. In *2014 IEEE/ION Position, Location and Navigation Symposium-PLANS 2014*, pages 804–817. IEEE, 2014.

[75] Francois D Cote, Ioannis N Psaromiligkos, and Warren J Gross. Gnss modulation: A unified statistical description. *IEEE Transactions on Aerospace and Electronic Systems*, 47(3):1814–1836, 2011.

[76] Seokho Yoon, Keunhong Chae, and Sun Yong Kim. A new approach to local signal design for enhanced tmboc signal tracking. *Journal of Electrical Engineering & Technology*, 15(4):1837–1845, 2020.

[77] Saifeddine Chebir, Salih Aidel, Khaled Rouabah, S Attia, and Mustapha Flissi. Gnss signals acquisition and tracking in unfavorable environment. *Radioengineering*, 27(2):557–571, 2018.

[78] José Ángel Ávila Rodríguez. *On generalized signal waveforms for satellite navigation*. PhD thesis, München, Univ. der Bundeswehr, Diss., 2008, 2008.

[79] Guenter W Hein, Jose-Angel Avila-Rodriguez, Lionel Ries, Laurent Lestarquit, Jean-Luc Issler, Jeremie Godet, and Tony Pratt. A candidate for the galileo l1 os optimized signal. In *Proceedings of the 18th international technical meeting of the satellite division of the institute of navigation (ION GNSS 2005)*, pages 833–845, 2005.

[80] Thomas A Stansell Jr. Rtcm sc-104 recommended pseudolite signal specification. *Navigation*, 33(1):42–59, 1986.

[81] Joon Wayn Cheong. *Signal processing and collective detection for Locata positioning system*. PhD thesis, UNSW Sydney, 2012.

[82] Tin Lian Abt, Francis Soualle, and Sven Martin. Optimal pulsing schemes for galileo pseudolite signals. In *Proceedings of the 18th International Technical Meeting of the Satellite Division of The Institute of Navigation (ION GNSS 2007)*, pages 926–934, 2007.

[83] Daniele Borio and Cillian Odriscoll. Design of a general pseudolite pulsing scheme. *IEEE transactions on aerospace and electronic systems*, 50(1):2–16, 2014.

[84] Weihua Zhuang and James Tranquilla. Digital baseband processor for the gps receiver (parts i and ii). *IEEE Transactions on Aerospace and Electronic Systems*, 29(4):1343–1349, 1993.

[85] David Akopian. Fast fft based gps satellite acquisition methods. *IEE Proceedings-Radar, Sonar and Navigation*, 152(4):277–286, 2005.

[86] PK Sagiraju, GVS Raju, and D Akopian. Fast acquisition implementation for high sensitivity global positioning systems receivers based on joint and reduced space search. *IET Radar, Sonar & Navigation*, 2(5):376–387, 2008.

[87] Bilal Beldjilali and Belkacem Benadda. A new proposed gps satellite signals acquisition algorithm based on the fast fourier transform. *Journal of electrical and electronics engineering*, 11(2):5–10, 2018.

[88] Kewen Sun and Letizia Lo Presti. Bit sign transition cancellation method for gnss signal acquisition. *The journal of navigation*, 65(1):73–97, 2012.

[89] Can Zhu and Xiangning Fan. Weak global navigation satellite system signal acquisition with bit transition. *IET Radar, Sonar & Navigation*, 9(1):38–47, 2015.

[90] Sanghoon Jeon, Hyoungmin So, Ghangho Kim, Changdon Kee, Kiho Kwon, and SeungWoon Choi. Analysis of gnss signal acquisition methods for the bit-transition problem for a single code period. *Transactions of the Japan Society for Aeronautical and Space Sciences*, 56(1):31–41, 2013.

[91] Daniele Borio, Eduardo Cano, and Gianmarco Baldini. Sychronization of pulsed pseudolite signals: analysis and comparison. In *Proceedings of the 25th International Technical Meeting of the Satellite Division of The Institute of Navigation (ION GNSS 2012)*, pages 482–493, 2012.

[92] Joon Wayn Cheong, Andrew G Dempster, and Chris Rizos. Detection of time-hopped ds-cdma signal for pseuodolite-based positioning system. In *Proceedings of the 22nd International Technical Meeting of the Satellite Division of The Institute of Navigation (ION GNSS 2009)*, pages 881–891, 2009.

[93] Shijie Yun, Zheng Yao, Tengfei Wang, and Mingquan Lu. High accuracy and fast acquisition algorithm for pseudolites-based indoor positioning systems. In *2016*

fourth international conference on ubiquitous positioning, indoor navigation and location based services (UPINLBS), pages 51–60. IEEE, 2016.

[94] Kai Borre, Dennis M Akos, Nicolaj Bertelsen, Peter Rinder, and Søren Holdt Jensen. *A software-defined GPS and Galileo receiver: a single-frequency approach*. Springer Science & Business Media, 2007.

[95] Olivier Julien. *Design of Galileo L1F receiver tracking loops*. University of Calgary, Department of Geomatics Engineering, 2005.

[96] J Wang et al. Pseudolite applications in positioning and navigation: Pro-gress and problems. *Positioning*, 1(03), 2002.

[97] Markus Irsigler and Bernd Eissfeller. Comparison of multipath mitigation techniques with consideration of future signal structures. In *Proceedings of the 16th international technical meeting of the satellite division of the institute of navigation (ION GPS/GNSS 2003)*, pages 2584–2592, 2003.

[98] Huicui Liu, Xiaojing Li, Linlin Ge, Chris Rizos, and Feixue Wang. Variable length lms adaptive filter for carrier phase multipath mitigation. *GPS solutions*, 15(1):29–38, 2011.

[99] P Zhong, XL Ding, DW Zheng, Wu Chen, and DF Huang. Adaptive wavelet transform based on cross-validation method and its application to gps multipath mitigation. *GPS solutions*, 12(2):109–117, 2008.

[100] Valanon Uaratanawong, Chalermchon Satirapod, and Toshiaki Tsujii. Evaluation of multipath mitigation performance using signal-to-noise ratio (snr) based signal selection methods. *Journal of Applied Geodesy*, 15(1):75–85, 2021.

[101] D Dong, M Wang, W Chen, Z Zeng, L Song, Q Zhang, M Cai, Y Cheng, and J Lv. Mitigation of multipath effect in gnss short baseline positioning by the multipath hemispherical map. *Journal of Geodesy*, 90(3):255–262, 2016.

[102] Khaled Rouabah, Chebir Saifeddine, Salim Atia, Mustapha Flissi, and Djamel Chikouche. Mathematical model of non-coherent-dll discriminator output and multipath envelope error for boc (α, β) modulated signals. *Positioning*, 4(1):65–79, 2013.

[103] Mustapha Flissi, Khaled Rouabah, Djamel Chikouche, Abdehalim Mayouf, and Salim Atia. Performance of new boc-aw-modulated signals for gnss system. *EURASIP Journal on Wireless Communications and Networking*, 2013(1):124, 2013.

[104] AJ Van Dierendonck, Pat Fenton, and Tom Ford. Theory and performance of narrow correlator spacing in a gps receiver. *Navigation*, 39(3):265–283, 1992.

[105] Yuqi Liu, Yihang Ran, Ting Ke, and Xiulin Hu. Characterization of code tracking error of coherent dll under cw interference. *Wireless Personal Communications*, 66(2):397–417, 2012.

[106] Hyoungmin So, Ghangho Kim, Taikjin Lee, Sanghoon Jeon, and Changdon Kee. Modified high-resolution correlator technique for short-delayed multipath mitigation. *The Journal of Navigation*, 62(3):523–542, 2009.

[107] Jason Jones, Pat Fenton, Brian Smith, et al. Theory and performance of the pulse aperture correlator. In *Proceedings of ION GPS*, volume 2004, 2004.

[108] Gary A McGraw and Michael S Braasch. Gnss multipath mitigation using gated and high resolution correlator concepts. In *Proceedings of the 1999 national technical meeting of the institute of navigation*, pages 333–342, 1999.

[109] Khaled Rouabah, Salim Atia, Mustapha Flissi, Mohamed Salim Bouhlel, and Salaheddine Mezaache. Efficient technique for dll s-curve side zero-crossings cancellation in global positioning system/galileo receiver. *IET Signal Processing*, 13(3):338–347, 2019.

[110] Yudong Sun, Zheng Yao, and Mingquan Lu. Extended double-delta correlator technique for gnss multipath mitigation. *IEEE Transactions on Aerospace and Electronic Systems*, 59(2):1758–1773, 2022.

[111] P Fenton, B Smith, J Jones, et al. Theory and performance of the pulse aperture correlator. *Tecnical report, Novatel Inc*, 2004.

[112] Youssef Tawk, Cyril Botteron, Aleksandar Jovanovic, and P-A Farine. Performance comparison of different correlation techniques for the altboc modulation in multipath environments. In *2010 IEEE International Conference on Communications*, pages 1–6. IEEE, 2010.

[113] Sihem Zitouni, Khaled Rouabah, Salim Attia, and Djamel Chikouche. Comments on "a general model of multipath error for coherently tracked boc modulated signals". *Wireless personal communications*, 70(4):1397–1407, 2013.